Exploring Nanoparticle Protein Corona Integrity and Drug Distribution from Biodegradable Carriers with Synchrotron-Based Techniques

Dissertation
zur Erlangung des Doktorgrades
and der Fakultät für Mathematik, Informatik und Naturwissenschaften
Fachbereich Physik
Der Universität Hamburg

vorgelegt von

Marvin Bernd Skiba

Hamburg
2024

Gutachter/innen der Dissertation (Supervisor)	Prof. Dr. Wolfgang J. Parak Dr. Saša Bajt Prof. Dr. Barbara Rothen-Rutishauser
Zusammensetzung der Prüfungskommission (Examination Board)	Prof. Dr. Dorota Koziej Prof. Dr. Wolfgang J. Parak Dr. Saša Bajt Dr. Gerald Falkenberg Prof. Dr. Nina Rohringer
Vorsitzende/r der Prüfungskommission (Head of Examination Board)	Prof. Dr. Dorota Koziej
Datum der Disputation (Date of Disputation)	26.11.2024
Vorsitzender des Fach-Promotionsausschusses PHYSIK (Chairman of the Doctoral Committee Physics)	Prof. Dr. Markus Drescher
Leiter des Fachbereichs PHYSIK (Chairman of the Faculty Physics)	Prof. Dr. Wolfgang J. Parak
Dekan der Fakultät MIN (Dean of the MIN-Faculty)	Prof. Dr.-Ing. Norbert Ritter

Abstract

The use of nanomaterials in medicine has increased significantly in recent years, particularly due to their unique physical and chemical properties. Their ability to bind various biological molecules, such as proteins, DNA or drugs opens therefore a wide range of possibilities in therapy and diagnostics. One of the biggest challenges in the application of nanoparticles (NPs) is the formation of the so-called protein corona. As soon as NPs are introduced in biological media different biomolecules adsorb to their surface. This biological cover influences the interactions of the nanoparticles with cells and tissues and thus determines their biodistribution, cell uptake and ultimately their efficiency and safety. The integrity of the protein corona can be influenced by various processes; therefore a deeper understanding of these changes is crucial for the development of safe and effective nanomedical applications.

Furthermore, the question of how different layers of the hybrid construct – nanoparticle, ligands, proteins – can be differentiated and analyzed within these complex environments. By using traditional techniques, it is often challenging to resolve these multi-layered structures that occur *in vivo*.

This dissertation aims to address these knowledge gaps and advance research in these areas. Specifically, the work focuses on three projects:

In the first part, the integrity of a labeled pre-formed protein corona around gold nanoparticles is probed inside cells using X-ray fluorescence imaging. This study provides insight into the time dependent degradation in the intracellular environment.

The second part deals with the characterization of gold nanoparticle, labeled ligands and a labeled protein corona using anomalous small angle X-ray scattering. The proof of concept shows that the method is able to distinguish between the three different parts and thus enable a more detailed analysis of the hybrid system

In the next chapter, biodegradable polyelectrolyte capsules are explored as promising carrier in the field of drug delivery. These carriers can be designed to enhance the bioavailability of hydrophobic drugs and offer controlled or triggered release properties. Understanding the behavior of these carriers within cells is crucial for optimizing their design and effectiveness. The third project explores how X-ray fluorescence imaging can be used to track the intracellular distribution of a drug delivered by biodegradable microcarriers. This focuses on the release and localization of a Selenium based drug within the cellular environment, providing important data for the development of effective and safe drug delivery systems.

Zusammenfassung

Die Verwendung von Nanomaterialien in der Medizin hat in den letzten Jahren erheblich zugenommen, insbesondere aufgrund ihrer einzigartigen physikalischen und chemischen Eigenschaften. Ihre Fähigkeit, verschiedene biologische Moleküle wie Proteine, DNA oder Medikamente zu binden, eröffnet daher ein breites Spektrum an Möglichkeiten in Therapie und Diagnostik. Eine der größten Herausforderungen bei der Anwendung von Nanopartikeln (NPs) ist die Bildung der sogenannten Proteinkorona. Sobald NPs in biologische Medien eingebracht werden, lagern sich verschiedene Biomoleküle an deren Oberfläche an. Diese biologische Hülle beeinflusst die Wechselwirkungen der Nanopartikel mit Zellen und Geweben und bestimmt somit ihre biologische Verteilung, die Zellaufnahme und letztlich ihre Effizienz und Sicherheit. Die Integrität der Proteinkorona kann durch verschiedene Prozesse beeinflusst werden, und ein tieferes Verständnis dieser Veränderungen ist entscheidend für die Entwicklung sicherer und wirksamer nanomedizinischer Anwendungen.

Darüber hinaus stellt sich die Frage, wie die verschiedenen Schichten des Hybridkonstrukts - Nanopartikel, Liganden, Proteine - innerhalb dieser komplexen Umgebungen unterschieden und analysiert werden können. Mit herkömmlichen Techniken ist es oft schwierig, diese vielschichtigen Strukturen, die *in vivo* auftreten, aufzulösen.

Diese Dissertation zielt darauf ab, diese Wissenslücken zu schließen und die Forschung in diesen Bereichen voranzutreiben. Im Einzelnen konzentriert sich die Arbeit auf drei Projekte:

Im ersten Teil wird die Integrität einer markierten, vorgeformten Proteinkorona um Goldnanopartikel innerhalb von Zellen mittels Röntgenfluoreszenzbildgebung untersucht. Diese Studie gibt Aufschluss über den zeitabhängigen Zerfall in der intrazellulären Umgebung.

Der zweite Teil befasst sich mit der Charakterisierung von Goldnanopartikeln, markierten Liganden und markierten Proteinen mittels anomaler Kleinwinkel-Röntgenstreuung. Der *Proof of Concept* zeigt, dass die Methode in der Lage ist, zwischen den drei verschiedenen Komponenten zu unterscheiden und somit eine detailliertere Analyse des Hybridsystems zu ermöglichen.

Neben Nanopartikeln werden auch biologisch abbaubare Polyelektrolytkapseln als vielversprechende Träger für die Verabreichung von Arzneimitteln erforscht. Diese Träger können so gestaltet werden, dass sie die Bioverfügbarkeit von hydrophoben Arzneimitteln verbessern und kontrollierte oder ausgelöste Freisetzungseigenschaften bieten. Das Verständnis des Verhaltens dieser Träger in Zellen ist entscheidend für die Optimierung ihres Designs und ihrer Wirksamkeit. Das dritte Projekt untersucht, wie die Röntgenfluoreszenz-Bildgebung

genutzt werden kann, um die intrazelluläre Verteilung eines durch biologisch abbaubare Mikroträger verabreichten Medikaments zu verfolgen. Der Schwerpunkt liegt dabei auf der Freisetzung und Lokalisierung eines auf Selen basierenden Arzneimittels in der zellulären Umgebung, was wichtige Daten für die Entwicklung wirksamer und sicherer Arzneimittelabgabesysteme liefert.

List of Abbreviations

AMEM	Alpha modified Eagle medium
aSAXS	Anomalous small angle X-ray scattering
AuNP	Gold nanoparticle
CLEM	Correlative light and electron microscopy
COVID	Coronavirus disease
CTPR	Consensus tetratricopeptide repeat
Ctrl	Control
DESY	Deutsches Elektronen-Synchrotron
DEX	Dextrane
DLS	Dynamic light scattering
DMEM	Dulbecco's modified Eagle medium
DMSO	Dimethyl sulfoxide
DNA	Desoxyribonucleic acid
DREAM	Differential Evolution Adaptive Metropolis
DTT	Dithiothreitol
EC_{50}	Half maximal effective concentration
EDTA	Ethylenediaminetetraacetic acid
EMA	European medicines agency
ESI-MS	Electrospray ionization mass spectrometry
ESRF	European Synchrotron Radiation Facility
EXAFS	Extended X-ray absorption fine structure
FBS	Fetal bovine serum
FDA	Food and drug administration
FWHM	Full width at half maximum
ICP-MS	Inductively coupled plasma mass spectrometry
KB	Kirkpatrick-Baetz
LbL	Layer by layer
LSPR	Localized surface plasmon resonance
MTT	3-(4,5-dimethylthiazol-2-yl)-5-(3-carboxymethoxyphenyl)-2-(4-sulfophenyl)-2H-tetrazolium
M_w	Molecular weight

NP	Nanoparticle
p-XSC	1,4 - phenylenebis(methylene)seleno cyanate
PAH	Poly allylamine hydrochloride
PARG	Poly-L-arginine
PBS	Phosphate buffered saline
PCC	Pearsons' correlation coefficient
PCM	Phase contract microscope
PDI	Poly dispersity index
PEC	Polyelectrolyte capsule
PEG	Polyethylene glycol
PSS	Poly sodium 4-styrenesulfonate
ROI	Region of interest
ROS	Reactive oxygen species
SAXS	Small angle X-ray scattering
SEM	Scanning electron microscope
SXT	Soft X-ray tomography
TEM	Transmission electron microscope
TFA	Triflouroacetic acid
TIPS	Triisopropyl silane
UV	Ultraviolet
Vis	Visible
WAXS	Wide angle X-ray scattering
XANES	X-ray absorption near edge spectroscopy
XAS	X-ray absorption spectroscopy
XFI	X-ray fluorescence imaging
XPCS	X-ray photon correlation spectroscopy
XRF	X-ray fluorescence

List of Figures

1 Nanoparticles and the significance of the protein corona

Over the past decades nanoparticles (NPs) have influenced several research areas. Various applications of nanoparticles have made their way out of the laboratory and into our daily lives. Although nanomaterial-based products are already commercially available in various areas [1,2], their distinct chemical and physical properties also made them a promising tool in the field of medical diagnosis and therapy.[3] Many of these nanomaterial-based formulations are already approved by medical regulatory agencies (European Medicines Agency – EMA, Food and Drug Administration – FDA), following their introduction into clinics.[4,5] The recent COVID-19 pandemic has raised significant interest in the use of nanomaterials in biomedical applications underscored by their crucial role in nano-based vaccines.[6–8] Besides this prominent novel application, other nanomaterials are already used for a prolonged period in therapeutic purposes, *e.g.* the 1995 approved Doxil®, as a nano-formulation of the known anti cancerogenic drug doxorubicin[9], or the 1996 approved iron nanoparticle-based contrast agent for magnetic resonant imaging, Feridex®.[10] Despite these established uses, there are still several challenges that need to be addressed in the future directions of nanomedicines. One major area where the benefits of nanoparticles are being explored is the research of cancerous diseases. The first step lies in the successful delivery of the NPs to the intended point of action/the tumor. However, which sounds so simple, is still an ongoing debate and not fully elucidated. In general, this delivery of nanoparticles to tumor sites follows one of two possible mechanisms, either a passive accumulation of NPs caused by an altered microenvironment at the tumor region, or an active targeting strategy involving specific binding moieties on the nanoparticle surface for cells at the tumor site. The passive accumulation was explained by the enhanced permeability and retention effect. A controversial concept stating that administered NPs enter the tumor via gaps between the endothelial cells of the surrounding blood vessels and can't escape the tumor site due to dysfunctional tumor lymphatic vessels.[11,12] Recently, this paradigm has been challenged, resulting in strong indications whether this long-stated mechanism might be incorrect. The novel approach describes the passive delivery mechanism through an active transport and retention, whereby the exit is still accomplished due to intact lymphatic systems.[13,14] Nevertheless the question remains, why most of nanoparticles via passive accumulation strategies fail to reach the tumor in a desirable manner.[15–17] Although, several nanoparticles' parameters (*e.g.*, size[18], shape[19] or surface chemistry[20]) seems to impact the delivery efficiency[15], the dose of administered nanoparticles, which was often not considered, appears

to be the most influential parameter by oversaturating Kupffer cells.[21] This cognition might change the progress in novel nano-based drugs relying on a passive targeting mechanism. Targeted drug delivery of nanomaterials is becoming increasingly prominent, as it theoretically allows for specific cell types to be targeted and nanoparticles to be selectively concentrated.[22–25] In contrast, barely 0.7% of administered targeted nanoparticles were found in solid tumors according to a survey of more than 200 recent publications between 2005-2015.[15] This finding could be attributed to the possible denaturation, and thus loosing of their receptor binding-affinity of the structure of targeting peptides/antibodies when conjugated to the nanoparticle, or moreover the adsorption of biomolecules onto the nanoparticles surface, which covers the designed functionalities (Fig. 1).[26–29] This adsorption of different biomolecules, *e.g.*, lipids, carbohydrates, ions and proteins, is referred as the 'biological identity' of the nanoparticle.[30,31] Once the nanoparticle is introduced into a protein-enriched milieu, the surface is subsequently covered by a variety of proteins, which undergoes a dynamic exchange of adsorbing and desorbing from the NPs surface.[32,33]

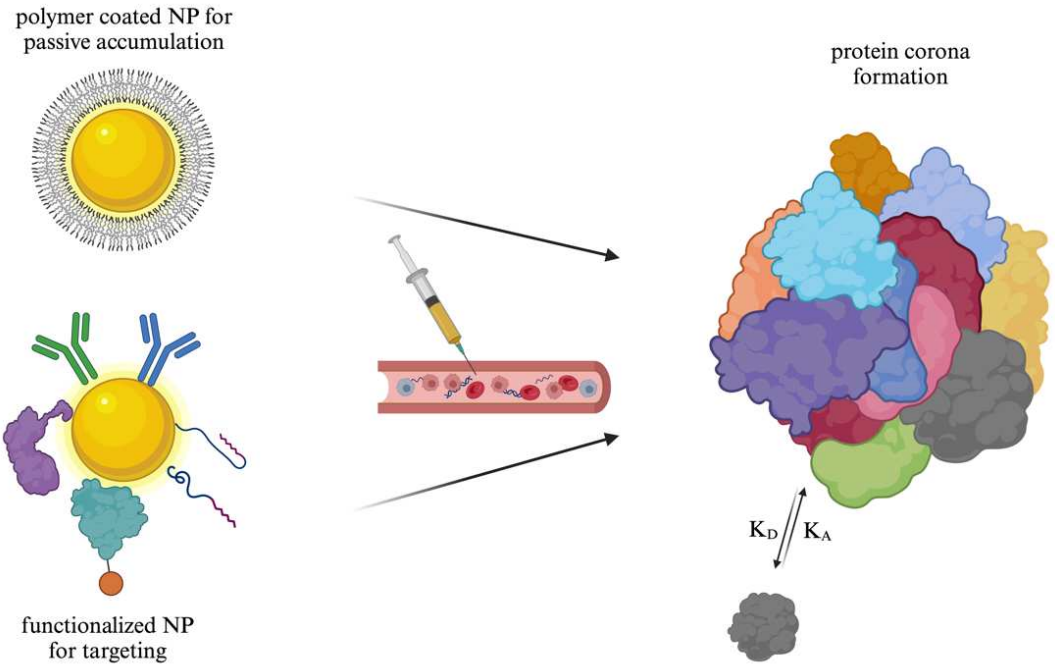

Figure 1: Scheme of protein corona formation onto polymer coated nanoparticles and functionalized nanoparticles after administrating into biological fluid. Created with BioRender.com.

Various distinctive techniques can be employed to experimentally investigate this protein corona on nanoparticles - including gel electrophoresis[34], mass spectrometry[35,36],

spectroscopy[37,38] or light scattering techniques[39]. Considering that each of the above-mentioned techniques is based on a change of a physicochemical property, it becomes evident how drastically the corona formation alters the nanoparticle from its designed self. Extensive research has shown that the protein corona formation and composition severely impact the behavior of nanoparticles, influencing critical parameters, such as overall biocompatibility, cellular uptake and biodistribution in small animal models, regardless of an active or passive targeting strategy.[40–44] It should be noted that the protein corona formation can also be beneficial in terms of an increased colloidal stability of the nanoparticles and thus reduced cytotoxicity.[45,46] Consequential research strives to control the protein corona formation to achieve specific effects, such as influencing cell or tissue specificity by pre-forming a protein corona with selected proteins.[47,48] While still a common immune response to protein corona decorated nanoparticles is the increased phagocytic activity by macrophages which will direct the NP to the liver and spleen, resulting in premature clearance from the bloodstream. This reduced circulation time *in vivo* has significant implications for biodistribution, affecting the ability to reach target sites and potentially reducing the therapeutic efficacy due to lower local concentrations.[49]

This significant influence has prompted numerous studies to investigate the protein corona formation and the following behavior.[50–53] However, many of the studies are performed in well-controlled test solutions, and thereby may not fully replicate the complexity of *in vivo* environments. Although several *in situ* and *in vivo* approaches have been proposed to enhance our understanding of these interactions, they are mostly still in the development stages and require further validation before becoming routinely available.[54–58] Also, most of the proposed methods are pursued for whole animal models, whereas *in vitro* experiments focusing on cellular resolution are lacking. What happens to the protein corona after NPs are taken up by cells remains broadly unclear. Detailed knowledge of the intracellular fate of the protein corona is crucial for understanding and developing nanoparticle-based drug delivery systems. The intracellular degradation of the protein corona and its components can lead to various byproducts with diverse biological impacts, ranging from toxicity to immune regulation.

Lately evidence was provided that the degradation of the protein corona within lysosomes, following a different intracellular decomposition by employing optical fluorescence microscopy techniques.[59,60] More recently the findings were further studied by using correlative light and electron microscopy (CLEM), enabling high resolution imaging allowing for ultrastructural intracellular examination.[61] Therein evidence was demonstrated that the hybrid

construct undergoes a separate endosomal sorting, resulting in the excretion of the nanoparticles whereas the protein corona remains inside the cell to be metabolized. The reason for the intracellular divergence was suspected to be the pH value inside these trafficking vesicles or additionally that the ionic environment affecting the binding affinity, suggesting the degradation might be a passive mechanism.

It has to be noted that these results rely primary on fluorescent labelling of the parts, followed by microscopic evaluation. However, it's important to acknowledge potential challenges using fluorescence-based techniques. The primary issues are the potential detachment of the label, which can lead to inaccuracies in data acquisition or quenching, where non-radiative processes of the fluorophore reduce the fluorescence signal.[62] Additionally, when using visible light the spatial resolution is restricted to half the wavelength (thus hundreds of nanometers), due to the Abbe-limit of separating two distingue objects. Moreover, the penetration depth of visible light is restricted to millimeters, caused of the high absorption and scattering probability by soft tissue.[63]

In this context, X-ray-based techniques offer a complementary approach due to their unique capabilities. X-rays can provide an excellent balance between penetration depth and spatial resolution, enabling to explore structures at tissue, cellular and subcellular levels with high accuracy.[64] Soft X-ray (~0.1 – 1 keV) imaging is particularly suited for visualizing organelles within cells due to its ability to provide high-resolution images without the need of exogenous labels. The contrast is generated as a result of different linear absorption coefficients of the cellular compartments and the nanoparticles, respectively. Techniques such as soft X-ray tomography (SXT) facilitate the three-dimensional reconstruction of cellular structures at nanometer-scale resolution, offering a detailed view of the intracellular milieu and distribution of nanomaterials.[65,66] However, soft X-rays suffer from limited penetration depth of some micrometers in soft tissue, making them more suitable for studying thin samples or isolated cells. To overcome limitations in penetration depth, hard X-rays (~1 – 100 keV) can be employed. Hard X-ray imaging techniques, such as hard X-ray tomography or Compton imaging, are capable of penetrating thicker tissues and even whole organisms, allowing for comprehensive examination of internal structures.[67–70] X-ray fluorescence (XRF) imaging further complements this capability by providing quantitative elemental mapping in two or three dimensions, crucial for understanding the distribution of nanoparticle components within tissues or intracellular.[71–73] For structural analysis, techniques like Small-Angle X-ray Scattering (SAXS) and Wide-Angle X-ray Scattering (WAXS) can be employed to explore the

size, shape, crystallinity and organization of nanoparticles and their assemblies. These methods provide insights into nanoparticle aggregation and dispersion in complex biological media.[74] X-ray photon correlation spectroscopy (XPCS) is additionally useful for examining dynamic processes, offering information on particle interactions and stability over time in biological environment.[75] In terms of chemical characterization, X-ray absorption spectroscopy (XAS) offers detailed insights into the chemical environment and electronic states of specific elements within a sample. This is further enriched by techniques like X-ray near edge structure spectroscopy (XANES) and extended X-ray absorption fine structure spectroscopy (EXAFS), which provide detailed information about the local geometric and electronic configuration of atoms. For example, these techniques have been shown to be crucial in understanding silver nanoparticle associated cell toxicity, by identifying different chemical silver species (Ag^0, Ag-S, Ag-O, …) over time in cells.[76]

These advanced X-ray based methodologies can therefore provide a comprehensive view of the structural, chemical, and spatial dynamics of nanoparticles in biological environment, significantly advancing the development of nanoparticle-based drug delivery systems to enhance their efficacy in biomedical applications. The following thesis will consequently explore the basics of synchrotron-based X-ray generation, fundamentals of X-ray fluorescence and anomalous small angle X-ray scattering and how this improves the study of nanoparticles and microcarriers for *in vitro* scenarios.

1.1 X-Ray Generation: The Impact of Synchrotron Technology

Historically, X-rays have been used in the field of biomedicine from the very beginning, as emphasized in the famous first X-ray image of C. Röntgen's wife's hand in 1895.[77] Nowadays, artificial X-rays are indispensable in the medical field, for example as a routine imaging method of hard and soft tissue or as a therapy in cancer treatment. In these medical applications, the high energetic electromagnetic waves are predominantly generated as bremsstrahlung. Hereby a heated metal cathode emits electrons as a result of the thermoelectric effect. The produced electrons are accelerated by a high voltage in the direction of the anode. The anode usually consists of an element with high atomic number, typically tungsten, due to its high melting temperature and efficiency in generating X-rays. As soon as the electrons hit this anode material, they are suddenly decelerated, resulting in the emission of X-rays. The underlying physical principle hereby is the conservation of energy. Since the charged particles, in this case electrons, are suddenly decelerated, they lose kinetic energy, which is then transformed into radiation. In addition, these electrons can eject an electron from the inner shell anode material atoms. This gap in the electronic structure is suddenly filled by an outer shell electron, which emits an element characteristic photon, again conserving the energy of the system. This process, called X-ray fluorescence, is discussed in more detail in section 2.3 below. The X-rays generated at the anode consist of a continuous spectrum caused by bremsstrahlung with characteristic fluorescence lines. Followed by filtering to remove low energetic X-rays to reduce noise and patient dose, the X-rays are used for medical imaging. The primary principle is that different tissues have different attenuation properties. Hard tissues, such as bone, consisting of higher Z material (mostly Ca) and thus attenuating X-rays more than soft tissue, which predominantly contain low Z elements (*e.g.* C, O, N).[78,79]

Another method of generating more intense X-rays, compared to the technique above, is to utilize synchrotron radiation. The underlying principle is rather similar as synchrotron radiation is also a specific type of bremsstrahlung. Hereby, from the first generation of synchrotron facilities on, high magnetic fields of bending magnets, force charged particles on a circular trajectory via the Lorentz force in a storage ring. The change of direction of the charged particles leads then to the emission of X-rays. The energy of the emitted beam is dependent on the speed, particles' mass and the radius of the orbit. This basic concept was subsequently expanded into the next generation of synchrotron facilities, with the adaption of wigglers and/or undulators in the straight sections of the storage ring. These insertion devices are arrays of magnets with

alternating orientation, constraining the charged particles on a sinusoidal path. Each oscillation results in the generation of synchrotron radiation. In case of wigglers, the magnetic force and thus the amplitude of oscillation of the charged particles is relatively high, which consequences in a high energetic, but broad emitted radiation spectrum. An undulator on the other hand uses lower magnetic field strengths. This reduced deflection results in coherently overlapping radiation packets, which leads to a narrow and intense X-ray spectrum. Overall, both, wigglers and undulators enhance the ability of synchrotron facilities to produce intense X-rays. As the generation mechanism is slightly different, generally undulators provide a more monochromatic, coherent and intense beam, while wigglers produce a broader spectrum with higher total power.[80,81]

Once the synchrotron beam has been generated in the source, further modifications are required for most of the experiments performed at a synchrotron facility. The following paragraph describes selected components that have been used in the context of the work presented here. It should be noted that a variety of different devices are used at synchrotron facilities for specific purposes. At a first glance experiments generally require a well-defined photon energy of the incident beam on the sample. A common system for this purpose is a double-crystal monochromator. This type of monochromator utilizes Bragg's law of diffraction, *i.e.* polychromatic light from the source hits the crystal, whereas only light with the wavelength that satisfies Bragg's law is reflected at a certain angle. The second subsequent crystal reflects the monochromatic beam parallel to the initial source beam. Due to the choice of crystal material and the ease of angle adjustment, such a monochromator system covers a wide energy range. Especially for X-ray microscopy studies, the now monochromatic beam needs to be focused to a suitable spatial beam size. Kirkpatrick-Baetz (KB) mirror systems are frequently employed as X-ray focusing devices at synchrotron facilities. Each mirror in a KB mirror system has an elliptical shape which allows it to focus the incident beam in one focal plane each - by total reflection. Through positioning two mirrors orthogonally to each other, the X-ray beam can be focused in both, vertical and horizontal plane, to a focal point, nowadays at a sub-50-nm level, suitable for high resolution imaging experiments.[82–84] Subsequently the monochromatic and focused X-ray beam is then directed onto a sample of interest, whereas different processes of light-matter interaction can occur. In the following sections two of these interactions are described in more detail, as they were used for the experiments presented in this thesis.

1.2 X-Ray Fluorescence Imaging

X-ray fluorescence imaging (XFI) is a versatile method for obtaining two- or three-dimensional maps of many different types of materials. In general, X-ray fluorescence can be described as a two-step process, as a specific case of light-matter interaction. Light, as an electromagnetic wave, is capable of ionizing atoms by exciting their electrons, when the energy of the photon is higher than the binding energy of the electron. Therefore, the energy of X-rays is high enough to excite even strongly bound electrons in the inner shell of atoms. The probability of this first crucial step, the photoelectric effect, scales therefore with the exciting energy.[85,86] An element specific constant, the mass attenuation coefficient, represents the fraction of photons removed from the incident X-ray beam per unit mass of the material, as depicted for gold in Fig. 2.

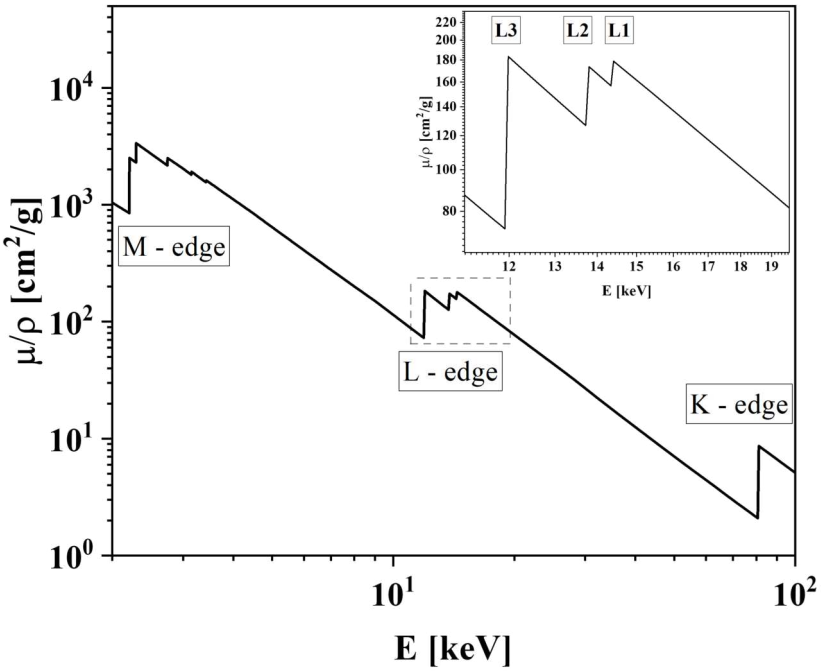

Figure 2: Mass attenuation coefficient of Au as a function of incident X-ray energy. The inlay in upper right corner shows a magnified view of the L absorption edge. Values extracted from National Institute of Standards and Technology.[87]

Within the energy range used for all the experiments presented in this work (7 – 17 keV), photoelectric absorption is the main process responsible for the loss of X-ray photons by interaction with the sample. The contributions of coherent and incoherent scattering processes are rather low (< 1%) for this element at these energies used, while the energy for other

processes, *e.g*. pair production is too low. The mass attenuation coefficient decreases with increasing photon energy. However, whenever the energy of the incident photon equals or exceeds the binding energy of an electron of the material, the photon is most probable to be absorbed, resulting in the creation of a photoelectron and a hole, leading to a sharp increase in the absorption coefficient, called the absorption edge. These absorption edges are named according to the principal quantum number of the excited electron (n = 1 – K, n = 2 – L, n = 3 – M). A closer look at the absorption edges reveals that these are not just one sharp irregularity in the decreasing mass attenuation coefficient with energy. In detail, the inset in Fig. 2 shows that the absorption edges are differentiated even more, as a result of different subshells and spins, *e.g.*: L1 – 2s electron, L2 – 2p1/2 and L3 – 2p3/2 electrons, which differ in binding energy due to spin-orbit coupling.[88]

This absorption of the X-ray photon and ejection of an inner shell electron results in an unstable state for the atom. This vacancy in electronic structure is therefore subsequently filled by an electron from a higher energy level. Following conservation of energy, some kind of energy must be transferred as a result of the relaxation of the electron, which can occur either by non-radiative processes, or by the emission of an X-ray fluorescence photon. Non-radiative processes, *e.g.*, Auger electron cascade or Coster-Kronig transitions will not be discussed in the following chapter, however it needs to be noted that these are the main reason for lowering X-ray fluorescence yields, especially in case of low-Z materials.[89–91]

In the event of an X-ray fluorescence photon being emitted, the energy is specific to the distinguishable transition and therefore equivalent to the difference in energy between the initial and final states of the electron. The emission of the photon is independent from the direction of the exciting photon and isotropic over the full solid angle $4 \times \pi$. The full process is schematically shown in Fig. 3 below. The resulting X-ray photon with λ_2 shown here is according to IUPAC named as an L3M5 photon, as in the initial state the vacancy is created in the L3 shell, and subsequently filled from an electron of the M5 shell.[92,93]

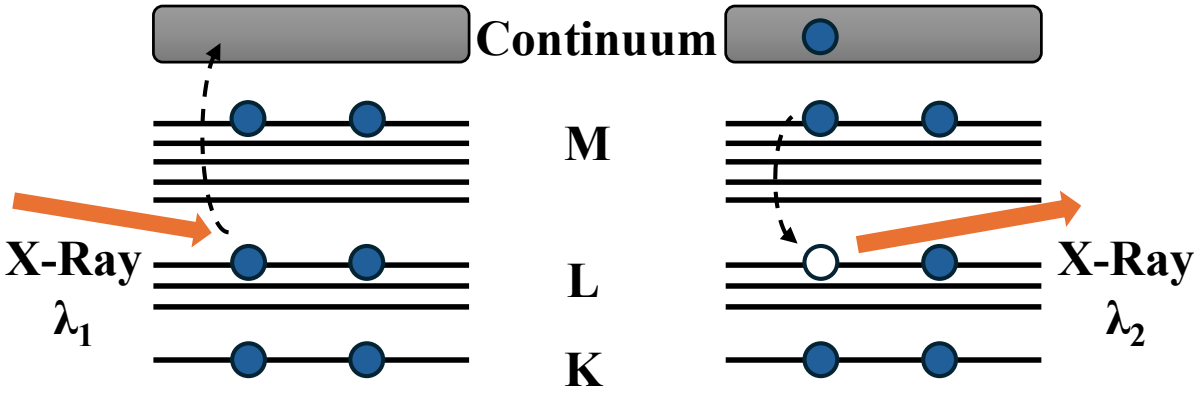

Figure 3: Schematic illustration of the X-ray fluorescence process. On the left scheme the incident photon beam with wavelength λ_1 (orange) excites an electron (blue) from the L3 subshell. Subsequently an electron from the M5 subshell fills this vacancy (white), resulting in a characteristic X-ray emission with the wavelength λ_2. The energy of the emitted photons is thereby decreased ($\lambda_1 < \lambda_2$). It has to be noted that not all electrons of each shell are depicted in this scheme.

By illuminating a real sample, which consists of a multitude of atoms from various elements, different transitions occur quasi simultaneously. However, as the electrons in different elements experience a distinctive binding energy, the same transition in different elements, *e.g.* L3M5, creates a photon with an element characteristic energy. By detecting the resulting photons depending on their energy, this leads to a full spectrum with diverse peaks, originating from different elements. This feature of the X-ray fluorescence process enables the simultaneous determination of various elements with one excitation. Commonly two type of detector systems are used in X-ray fluorescence. On the one hand, wavelength-dispersive detectors, working as a combination of a monochromator and a nonspecific photon counter. These detectors are commonly used when high energetic resolution is necessary. Hereby the creation of a spectrum takes rather long time as different wavelengths have to be scanned one after another by changing the angle of the monochromator to satisfy Braggs' law of diffraction. More common, especially for imaging purposes, are the faster energy dispersive detectors. The basic principle of a solid-state detector, such as the widely used silicon drift detector, is the creation of an electron-hole-pair when the fluorescent X-ray photon strikes the detector material. The resulting electrons are accelerated by an electric field in the drift zone to an electrical contact. The so created electrical signal, proportional to the number of electrons, is thereby proportional to the energy of the incident X-ray photon, since higher energy photons, create more electron-hole pairs. When analyzing spectra recorded with a silicon drift detector, two intrinsic features have to be taken

into account. First, a so-called pile-up artifact is possible when two or more X-ray photons get detected in a shorter time frame than the detector readout time. This creates an artificial event with an energy equal to the sum of the incident photon energies. Another artifact that needs to be considered are escape-peaks. If the energy of the incident fluorescent photons is higher than to the absorption edge of the detector material, part of the energy can be absorbed, before electron-hole pairs are created. Subsequently, secondary X-ray fluorescence photons can be emitted from the detector material, which "escape" the detector. The result is the detection of a second peak with an energy lower than the energy of the primary fluorescence photons by the difference corresponding to the absorption edge energy of the detector material.[94,95]
In a typical X-ray fluorescence imaging experiment, the position of the X-ray beam is fixed and the sample is moved step by step in different directions to project a map. The step size is chosen, either when high spatial resolution images are required, based on the focusing dimensions of the X-ray beam, or for fast evaluation of larger areas based on the photon flux. In practice, the optimal solution is often a compromise between the two, enabling high spatial resolution while maintaining an appropriate acquisition time. The incident photon energy is chosen to be high enough to excite all elements of interest, considering that for higher energies the fluorescence yield of low energetic transitions is decreased, as discussed in the previous section.
In each movement step of the sample, a spectrum is recorded, reflecting all the above-mentioned steps. Figure 4A shows exemplary one summed spectrum of a cell treated with AuNPs bearing Gd tagged proteins, excited with 17 keV at the European Synchrotron Radiation Facility (ESRF), beamline ID16A.[96] This spectrum is used in the following to further explain crucial processing steps to finally obtain a 2-dimensional elemental map.

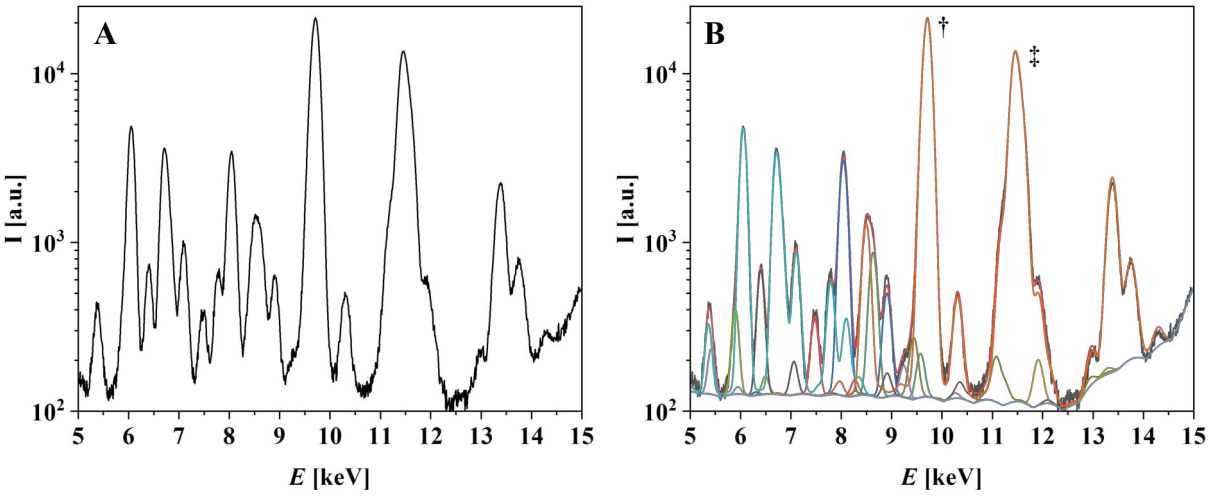

Figure 4: A) Summed X-ray fluorescence spectrum of a mammalian cell, treated with Au and Gd nanoparticles, after excitation with 17 keV synchrotron radiation. B) Fitted spectrum showing the various underlying individual emissions. Each color represents the X-ray emission of a certain element in the sample. Notations † and ‡ are used to specify two different Au emissions: L3M5 and L2M4, respectively.

The spectrum shown in Fig.4A represents a sum of each individual spectrum detected from illuminating one pixel for 50 ms. In this specific case the area of one cell (35 µm horizontally, 20 µm vertically) was mapped with a step size of 70 × 70 nm^2, resulting in ~204'000 individual spectra. The most prominent peak in this spectrum at 9.7 keV (labeled with †) corresponds to the X-ray photon generated by the previously described L3M5 transition of Au. However, it becomes clear that the spectrum is quite complex as it consists of various peaks which may overlap in their detected energies. All the results presented in this thesis originate from fitting the individual spectra using PyMCA.[97] The software toolkit PyMCA, developed at the ESRF, includes diverse algorithms needed for a whole spectrum evaluation, *e.g.* background models, peak shapes, energetic position of peaks, fluorescence yields and additionally calculations for the discussed detector artifacts of pile-up and escape peaks. Following an experiment/ detector specific energy calibration, the summed spectrum is consequently fitted using a linear-combination of gaussian shaped peaks. The characteristic X-ray emission energies of most known elements are tabulated, based on theoretical calculations and experimental confirmations.[98,99] Figure 4B illustrates the complex composition of the overall spectrum. Each color herein represents the predicted emission of one element, while every peak is originating theoretically from a specific electronic transition. The energy resolution of silicon drift detectors

however, is usually not sufficient to resolve two transitions with a small energy difference. For the orange-colored Au peak labeled by ‡ at around 11.5 keV, it is evident from the shape that it consists of several underlying smaller peaks. Indeed, the fitting reveals that it is originating from 6 distinct electronic transitions of gold and 2 smaller peaks originating from different elements (Pt and Br). The peaks maximum at 11.44 keV can be assigned to the L2M4 Au transition, which holds the highest fluorescence yield from the 6 transitions in this energy range. Besides qualitative evaluation of different elements in a spatial manner, quantitative values can be obtained by X-ray fluorescence imaging. Quantitative examination can be either obtained applying a fundamental parameter approach, or by comparing the measured dataset to a standard sample measured under the same conditions. The fundamental parameter method is fully based on a theoretical calculation. Thereby the final composition of the sample is extrapolated by the detected fluorescent intensities, considering the full physical parameters of the underlying processes.[100,101] Using an external standard sample, a relationship between the detected intensity for different elements and their known concentrations need to be determined. The standard sample should hereby contain either all elements of interest, or otherwise offer emissions over the energy range covering the elements of interest. In the second case it is subsequently necessary to extrapolate the obtained calibration factors to the elements of interest using their element-specific parameters (*e.g.* absorption efficiency, fluorescence yield).[102,103] Finally, by fitting each individual spectra at each motor position while considering the calibration factors, a 2-dimensional, quantitative, elemental map can be extracted. To keep consistent with the examples used throughout this chapter, a pseudo-colored image of a cell treated with AuNPs surrounded by a gadolinium (Gd) labeled protein is shown below. The cell is clearly depicted by the fluorescence originating from potassium (Fig. 5A), whereas the nanoparticles can be displayed by the fluorescence originating from Au (Fig. 5B), and the labeled protein by the Gd emission (Fig. 5C). In order to enhance the signal to noise ratio, the gold and Gd fluorescence is shown as sum of all emissions originating from transitions to L-shells (L3M5, L2M4, …). The following paragraph will elucidate how X-ray fluorescence imaging can help in understanding the dynamical intracellular fate of the protein corona onto nanoparticles.

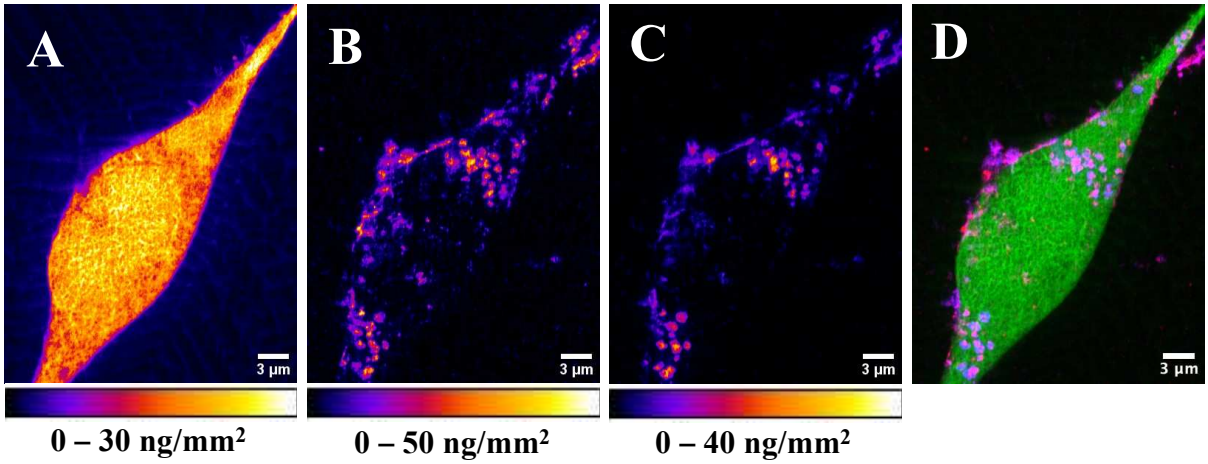

Figure 5: Pseudo colored images of different elements in a mammalian cell, treated with AuNPs bearing a Gd labeled protein, obtained by 2-dimensional X-ray fluorescence imaging. Quantitative pixel vales are shown for potassium (A), gold (B), gadolinium (C). The individual channels are merged in a false-color image (D) to showcase the multiplexing ability of X-ray fluorescence imaging, with potassium (green), gold (red), gadolinium (blue). Scale bar = 3 µm. Image modified with permission from Ref.[104]

1.3 Nanofocused X-Ray Fluorescence Imaging to probe the intracellular Fate of a Protein Corona around colloidal Nanoparticles

The project is motivated by the question of to what extent X-ray fluorescence imaging can be utilized to track the intracellular fate of a pre-formed protein corona around AuNPs with engineered consensus tetratricopeptide repeat proteins (CTPR). The protein corona, a layer of biological molecules that forms on NP surfaces, significantly affects NPs' biological interactions, including biodistribution and cellular uptake. Complementary techniques for studying the intracellular fate are limited to thin samples, in case of correlative electron and fluorescence microscopy, where the inherent resolution limit of visible light represents a significant limitation. Similarly, *ex vivo* techniques are often employed, *e.g*. mass spectrometry. Therefore, XFI offers a promising approach because it allows for the acquisition of elemental maps with high spatial resolution, potentially overcoming the restrictions described above. Despite these promising advantages, XFI is restricted to small sample populations, as the individual maps are acquired in a time-consuming manner as part of synchrotron beamtime. This can subsequently lead to difficulties regarding statistical significance of the obtained results due to cell-to-cell variability. The aim is to provide insights into the protein corona's intracellular fate at the cellular level, discussing advantages and drawbacks, which could eventually be applied to larger *in vivo* samples, improving the design and safety assessment of NP-based biomedical applications.

Most of the presented results of the following section were published in advance:

Skiba, M.; Guedes, G.; Karpov, D.; Feliu, N.; L. Cortajarena, A.; Parak, W.J.; Sanchez-Cano, C. Probing the Cellular Fate of the Protein Corona around Nanoparticles with Nanofocused X-ray Fluorescence Imaging. Int. J. Mol. Sci. 2024, 25, 528.
https://doi.org/10.3390/ijms25010528

Contribution:
The author contributed by synthesis and characterization of the nanoparticles, performing synchrotron experiments, formal analysis of the acquired data and by writing the manuscript.

Protein design, expression, Gd labeling and characterization was solely conducted by G. Guedes and A. L. Cortajarena. Information can be found in supporting information of the above-mentioned publication.

1.3.1 Materials

Ammonia solution (Sigma) , Acetic acid (Sigma), Dulbecco's modified eagle medium (DMEM, Gibco), Fetal bovine serum (Sigma), Penicillin/streptomycin (Invitrogen), Phosphate buffered saline (Thermo Fisher), trypsin/EDTA (Invitrogen), Bovine serum albumin (Sigma), Alpha modified eagle medium (AMEM, Gibco), Trypan blue (Invitrogen), 3-(4,5-dimethylthiazol-2-yl)-5-(3-carboxymethoxyphenyl)-2-(4-sulfophenyl)-2H-tetrazolium (Thermo Fischer), Dimethyl sulfoxide (Sigma), Dichloromethane (Sigma), Diethyl ether (Sigma), Trifluoroacetic acid (Thermo), Triisopropyl silane (Sigma), Diethylether (Sigma), Ethanol > 99% (Sigma), Nitric acid (Sigma), Hydrochloric acid (Sigma), Dithiothreitol, Sodium hydroxide, Amino-PEG-thiol (Rapp Polymere), Carboxy-PEG-thiol (Rapp Polymere), Methoxy-PEG-thiol (Rapp Polymere), Sodium citrate (Sigma), Gold (III) chloride trihydrate (Sigma), Ethylenediaminetetraacetic acid disodium salt (Sigma), Citric Acid (Sigma).

1.3.2 Methods

1.3.2.1 Synthesis of AuNPs

The synthesis of 12 nm sized AuNPs was carried out according to a previously published and established protocol.[105] For a common batch, 215 mL aqueous sodium citrate solution (2.75 mM) was mixed with 71 mL citric acid solution (2.75 mM) and boiled for 15 minutes, followed by the addition of ~2.5 mg ethylenediaminetetraacetic acid. After two minutes 71 mL of 812.5 µM, hot, aqueous gold chloride solution was added under vigorous stirring and boiled for additional 20 minutes before cooling down to room temperature under stirring. So obtained particles were either directly used for subsequent surface modification with polyethylene glycols or concentrated using spin filter units for coupling covalent coupling to proteins.

1.3.2.2 De-protection amino PEG

3.7 mL of dichloromethane was used to dissolve 0.0349 mmol of commercially available tritylthiol-PEG-amine (3 kDa). 307 µL triisopropyl silane (TIPS) and 223 µL triflouroacetic acid (TFA) were added ander vigorous stirring, before adding same amounts of TIPS and TFA once more. For fifteen minutes, the mixture was vigorously stirred while covered with parafilm. The solvent was evaporated using a rotary evaporator at 30 mbar and 60°C water bath. The so-obtained white powder was triturate and filter-washed using diethyl ether. Finally, a yield of 84.8%, or 0.0296 mmol, was obtained.[55]

1.3.2.3 Pegylation of citrate capped AuNPs

Thiolated PEGs were dissolved in miliQ water (10 mg/mL) and promptly added to the gold nanoparticle solution (250 PEG/nm^2 gold surface). The total gold surface in solution was calculated by assuming that each gold nanoparticle is a perfect sphere with a diameter of 12 nm. The solution was covered with parafilm and stirred overnight at room temperature before being collected. The first centrifugation was carried out at 4°C, 30,000 rcf for 60 minutes. The pellets were resuspended in miliQ and five additional rounds of washing by centrifugation (25,000 rcf, 30 min), with the supernatant replaced with fresh miliQ water to remove unreacted PEG molecules and precursors.

1.3.2.4 Particle characterization

The zeta-potential of the particles was determined by laser Doppler anemometry (Zetasizer, Malvern Panalytical, UK). Therefore, the nanoparticles were diluted in PBS and subsequently measured unless noted otherwise. All results shown in this work are presented as an average including standard deviation from three individual measurements. UV-visible absorbance spectroscopy (Agilent Varian Cary 5000, Santa Clara, USA) was carried out in a plastic cuvette with 1 cm pathlength. Nanoparticles were diluted in water or phosphate buffered saline (PBS) until an absorbance between 0.2 – 1.0 was reached at 520 nm. For size determination by transmission electron microscopy (TEM, JOEL JEM-2100F UHR, Akishima, Japan), one drop (8 µL) of nanoparticle solution was placed on a copper meshed carbon grid and let air dry. For negative staining experiments, 0.5 µL of 1 w.% Uranyl acetate in water was added on the grid after drying.

1.3.2.5 Cell culture

Mouse embryonic fibroblasts (3T3) cells were cultured in Alpha modified eagles' medium (AMEM), supplemented with 100 U/mL penicillin-streptomycin and 10% fetal bovine serum. Cells were grown until a confluency of 70 – 80% was reached at 37°C and 5% CO_2. Subculturing was conducted every 2 – 3 days with 0.05 w.% Trypsin, 0.02 w.% EDTA for chemical detachment of adherent cells.

1.3.2.6 Biocompatibility evaluation

Cell viability following exposure to AuNPs, CTPR-Gd protein, or the hybrid AuNP@CTPR-Gd was assessed using separate MTT assays.[106] For this process, 2×10^3 cells in 100 µL of AMEM cell medium were seeded into each well of a 96-well plate and incubated overnight. The next day, the growth medium was removed and replaced with 100 µL of fresh growth medium containing the compound of interest at various concentrations—ranging from 0.1 to 50 µg/mL for Au and 3 nM to 1.5 µM for the free protein. After 24 hours at 37°C with 5% CO_2, the cells were rinsed with 100 µL of PBS; then, 100 µL of growth medium containing 0.5 mg/mL of MTT was added. After a 2-hour incubation period, the growth medium was removed, and 100 µL of dimethyl sulfoxide (DMSO) was added to dissolve the formazan crystals formed in situ. The absorbance of each well was then measured at a wavelength of 550 nm, with background correction done using the absorbance at 630 nm.

1.3.2.7 Uptake evaluation

To confirm and quantify the cellular internalization inductively coupled plasma mass-spectrometry (ICP-MS) was used. Initially, 3×10^5 cells were placed in 6-well plates with 2 mL of AMEM and allowed to grow for 24 hours. After this period, the medium was removed, and the cells were exposed to compounds of interest at varying concentrations, dissolved in 2 mL of serum-free growth medium. After another 24 or 48 hours, the medium was discarded, and the cells were rinsed with 1 mL of PBS before being detached with 0.5 mL of Trypsin/EDTA solution. Cells were then collected by adding 1.5 mL of medium and transferred into a 15 mL Falcon tube. Trypan blue staining was employed for manual counting of live cells using a Neubauer hemocytometer.[107] Subsequently, the cells were centrifuged at 200 rcf for 5 minutes, and an additional 1 mL of aqua regia was added. The cells were then digested with a Berghof Speedwave XPERT microwave digester. Finally, the amounts of Au, Fe, and/or Gd were measured using ICP-MS.

1.3.2.8 Sample preparation for XFI

Mouse embryonic fibroblasts (3T3 cells) were grown on silicon nitride membranes for nanofocused synchrotron XRF-imaging experiments, following methods modified from previously published protocols.[108] The cells were removed from culture flasks and diluted in AMEM culture medium to a concentration of 50,000 cells/mL. Subsequently, a single drop (10 µL) was placed onto each pre-treated silicon nitride membrane, which was secured to the bottom of 6-well plates using UV-sterilized double-sided adhesive tape. The use of double-sided adhesive tape prevents the membrane from moving around in the well, which minimizes the risk of breakage during the experimental procedure. After two hours of incubation at 37°C with 5% CO_2, 2 mL of AMEM medium was gently added, and the plate was placed in an incubator overnight. The next day, the medium was removed and replaced with fresh AMEM medium, without FBS, for the control group or AMEM without FBS containing AuNP@CTPR-Gd (with an elemental concentration of Au determined by ICP-MS of C_{Au}~10 µg/mL), respectively. After 24 hours of treatment with AuNP@CTPR-Gd, cells were rinsed with 2 mL of PBS and maintained in 2 mL of fresh growth medium (without AuNP) for different incubation periods (in this study, t_{inc} = 0, 30, 60, and 120 minutes). Then, the membranes were removed, immersed in 150 mM ammonium acetate buffer (pH 7.1), blotted with filter paper, and immediately plunge-frozen in liquid ethane. Samples were then placed into custom-designed and 3D-printed sample holders and kept under cryogenic conditions until measurements were taken.

1.3.2.9 X-ray fluorescence imaging

All synchrotron experiments were conducted at beamline ID16A of the European Synchrotron Radiation Facility (ESRF, Grenoble, France). XRF-imaging of individual cells was performed under cryogenic conditions using two six-element silicon drift diode detectors with an active area of 3 cm^2, positioned 3 cm away from the sample. The incident beam energy was set to 17 keV (with a photon flux of 1.55×10^{11} ph/s) and focused to dimensions of 48.6 nm × 41.6 nm (FWHM, h × w). Detailed cellular mapping was carried out with a 70 nm × 70 nm step size and a dwell time of 50 ms. The combined emission spectra were fitted and analyzed using PyMCA software version 5.6.5. Elemental concentrations were calculated assuming a matrix thickness of 6 µm with a density set at 1 g/cm^3.

1.3.2.10 Colocalization Analysis

The colocalization of Au and Gd was analyzed on the elemental maps originating from the XFI experiment. Specifically, Pearson's correlation coefficients (*r*, PCC) and Manders' coefficients (M_1, M_2) were computed with the ImageJ-Coloc2 plugin.[109] In brief, The Pearson's correlation coefficient (PCC) measures the covariance between two images on a pixel-by-pixel base, normalized by their standard deviations. It ranges from -1 to 1, where -1 indicates perfect anti-correlation, 0 indicates no correlation, and 1 indicates perfect correlation. PCC is unaffected by differences in mean signal intensity but a poor signal-to-noise ratio can reduce its value towards 0.[110,111] Considering pixel intensities, two additional coefficients were determined: M_1, which is the proportion of channel A's signal overlapping with channel B above a threshold, and M_2, which measures the reverse. Manders coefficients are relatively insensitive to low signal-to-noise ratios as they sum many pixels above the threshold, minimizing random noise effects. The values range from 0 to 1, allowing for the investigation of individual dependencies.[112]
Each colocalization analysis was validated using Costes' significance test, which evaluates the statistical significance of colocalization between two signals by randomizing one of the signals and recalculating the correlation. If the randomized correlation remains below the original, it confirms significant colocalization, with a threshold of $p \geq 0.95$.[113]

1.3.3 Results and discussion

1.3.3.1 Particle characterization and *in vitro* evaluation

Gold nanoparticles were synthesized following a previously described method. Their surface was then modified with thiolated polyethylene glycols bearing terminal amine groups, to enhance their possibilities of forming a protein corona with negatively charged Gd labelled CTPR (zeta-potential of -24.9 ± 9.7 mV). The resulting AuNP were characterized by UV-Vis absorbance spectroscopy, zeta potential analysis, and transmission electron microscopy (TEM). Success of the surface modification was detected by a slight shift in the wavelength of the surface plasmon resonance of the gold nanoparticles (caused by changing of the surrounding refractive index) observed in their UV-Vis absorption spectra (Fig. 6), and supported by zeta potential changes (from -36.9 ± 1.3 mV for citrate AuNP to +27.3 ± 2.7 mV for PEG AuNP).

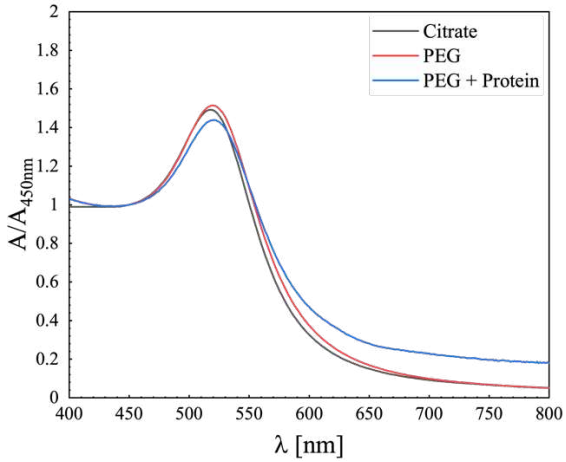

Figure 6: UV-Vis absorbance spectra of AuNP with different surface coatings.

Additionally, negative staining (with Uranyl acetate) TEM showed a narrow size distribution for the AuNP (Fig. 7A), with an average core diameter of $d_c = 11.9 \pm 0.7$ nm (Fig 7B, N = 121). The diameter of the whole NPs, including the organic PEG shell, was extended $d_{cs} = 32.5 \pm 4.9$ nm (Fig 7C, N = 189).

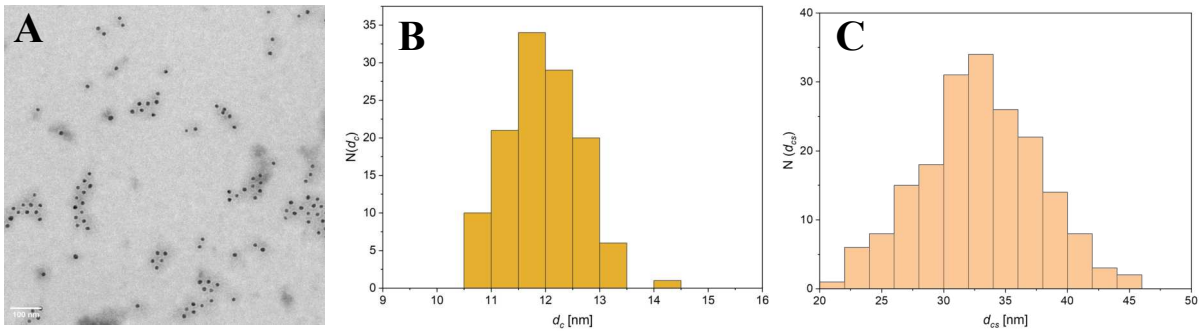

Figure 7: A) Representative transmission electron microscopy (TEM) image of AuNP with negative staining (with Uranyl acetate). The scale bar indicates 100 nm. B) Histogram of 121 measured NP core sizes (d_c) and C) histogram of 189 measured NP diameter including organic shell (d_{cs}), based on TEM images.

The formation of the protein corona of CTPR-Gd on the final particles was confirmed by three different approaches. First, a wavelength shift of the absorbance maximum of 1 nm was observed in the UV-Vis absorbance spectroscopy, similar to the shift from citrate capped AuNPs to pegylated AuNPs. Additionally, an indirect method using ICP-MS was conducted. For this, the initial ratio between CTPR-Gd protein and AuNP was determined to be 228. After three rounds of centrifugation (20 krcf, 30 min), changing the supernatant with PBS, still a ratio of

128 (proteins/AuNP) was detected. Since commonly this centrifugation parameters are not sufficient to pellet proteins, we conclude a "hard" protein corona was formed.[114] Moreover, gel electrophoresis was conducted with pegylated AuNP (Fig. 8, left lane) and the mixture of AuNP@CTPR-Gd (right lane). It is shown that the pure AuNP moved towards the anode, driven by the amino group moieties on the PEG. In contrast the AuNP with CTPR-Gd protein (AuNP@CTPR-Gd) stuck in the pocket and even concentrated slightly in direction in the direction of the cathode, which can be explained by the negative surface potential of the protein on top of positively charged pegylated AuNP.

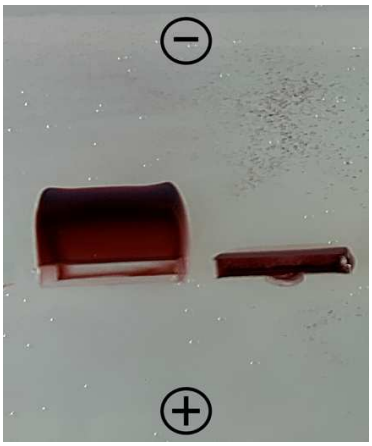

Figure 8: Agarose Gel electrophoresis (2 w.% agarose) of AuNP (left lane) and AuNP@CTPR-Gd (right lane).

Biocompatibility assays on mouse embryonic fibroblasts (3T3) cells revealed that pegylated AuNP, AuNP@CTPR-Gd, and free Gd labelled CTPR caused no acute toxicity up to 10 µg/mL Au or 2 µM protein (Fig. 9A,B). Notably, the choice of 10 µg/mL Au treatment for following XRF-imaging experiments and ICP-MS uptake experiments was intentionally made to ensure suitability for detection by XRF-imaging without overloading the cells with particles and thus create random overlap of the different components. Remarkably, a slight increase on cell viability as observed at higher CTPR-Gd concentrations might be due to possible interferences on the used 3-(4,5-dimethylthiazol-2-yl)-5-(3-carboxymethoxyphenyl)-2-(4-sulfophenyl)-2H-tetrazolium (MTT) assay caused by the protein, as reported for different polypeptides before.[115] Further cellular uptake experiments (Fig. 9C) determined that each individual cell internalized an average of 0.17 ± 0.04 pg Au and 0.22 ± 0.06 pg Gd after 24 h of treatment with AuNP@CTPR-Gd (c_{Au} = 10 µg/mL)

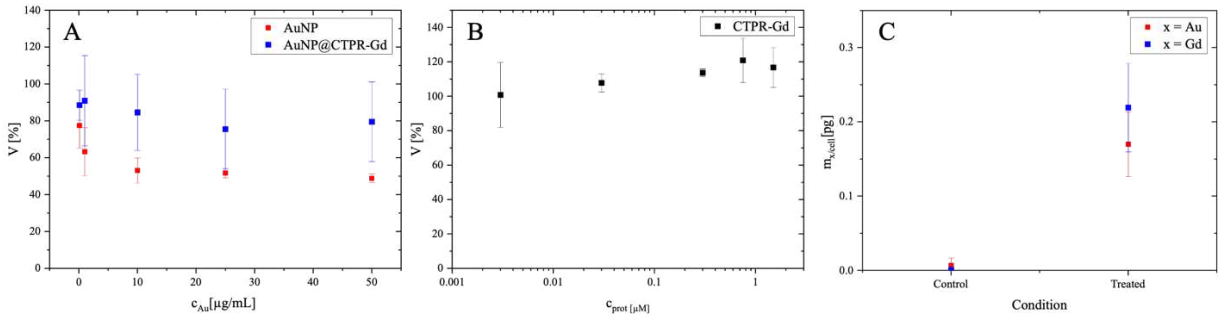

Figure 9: A) Cell viability V of AuNP and AuNP@CTPR-Gd, and B) free CTPR-Gd, in dependence of the Au concentration c_{Au} and the protein concentration c_{prot}, respectively. C) Mass of endocytosed Au and Gd *per* cell ($m_{Au/cell}$, $m_{Gd/cell}$ [pg]) on 3T3 cells exposed to c_{Au} = 0 (control) or c_{Au} = 10 µg/mL AuNP@CTPR-Gd (treated) for 24 h, without following incubation in NP-free medium (t_{inc} = 0) as measured with ICP-MS.

1.3.3.2 X-ray fluorescence imaging

To study the dynamic behavior of the protein corona after cellular internalization, we exposed 3T3 cells to AuNP@CTPR-Gd for 24 h (c_{Au} ~10 µg/mL), followed by different incubation times t_{inc} in particle free medium (0, 30, 60 or 120 min). Cells were cryopreserved and analyzed with XRF-imaging under close-to-native conditions at the ID16A cryo-nanoprobe beamline at the ESRF. As a control, untreated cells were prepared and analyzed in the same way. Initially, coarse scans were conducted (400 nm x 400 nm step size and 100 ms dwell time) to select 3T3 cells adequate for imaging. Information about the cell state was obtained based on K K_α emission maps, which indicated which cells were alive before fixation by plunge freezing and maintained their integrity during the process. Moreover, both K and Zn K_α emissions were used throughout the experiments to identify the cellular and nuclear outlines (respectively). Subsequently, at least three cells were imaged by XRF-imaging for each group (controls, or AuNP@CTPR-Gd exposure for 24 h followed by 0, 30, 60, 120 min NP-free incubation), with a lateral resolution of 70 nm x 70 nm. In total, 16 cells were imaged for this study. As expected, no Au- or Gd-L X-ray emission peaks were observed in the X-ray fluorescence spectra obtained from untreated 3T3 controls (Fig.10A), but were clearly visible in those from cells exposed to AuNP@CTPR-Gd (Fig. 10B).

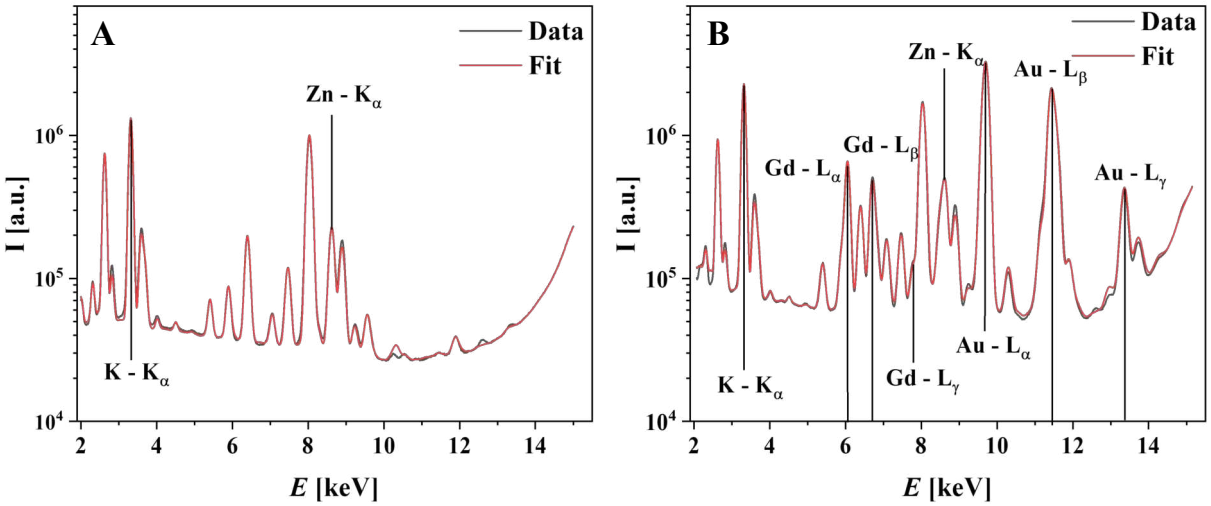

Figure 10: Summed X-ray fluorescence spectra of 3T3 cell mapping, showing the detected intensity I versus energy *E*. Left spectra (control in which cells were not exposed to AuNP@CTPR-Gd) shows no sign of Au or Gd L_α emissions as expected, whereas in the AuNP@CTPR-Gd treated sample (right) L_α emissions from Gd (*e.g.* 6.7 keV) and Au (*e.g.* 9.7 keV) are clearly visible.

The acquired spectra were subsequently fitted using PyMCA the identification and separation of the emission from distinct elements. This allowed for obtaining maps of Au and Gd as unique tracers for the NP cores and the protein corona (respectively) for each sample, see *e.g.*, Fig. 11. Pseudo-colored images of K, Zn, Au, and Gd for all measured high-resolution cells are listed in the Appendix section (see Figures A1-A5).

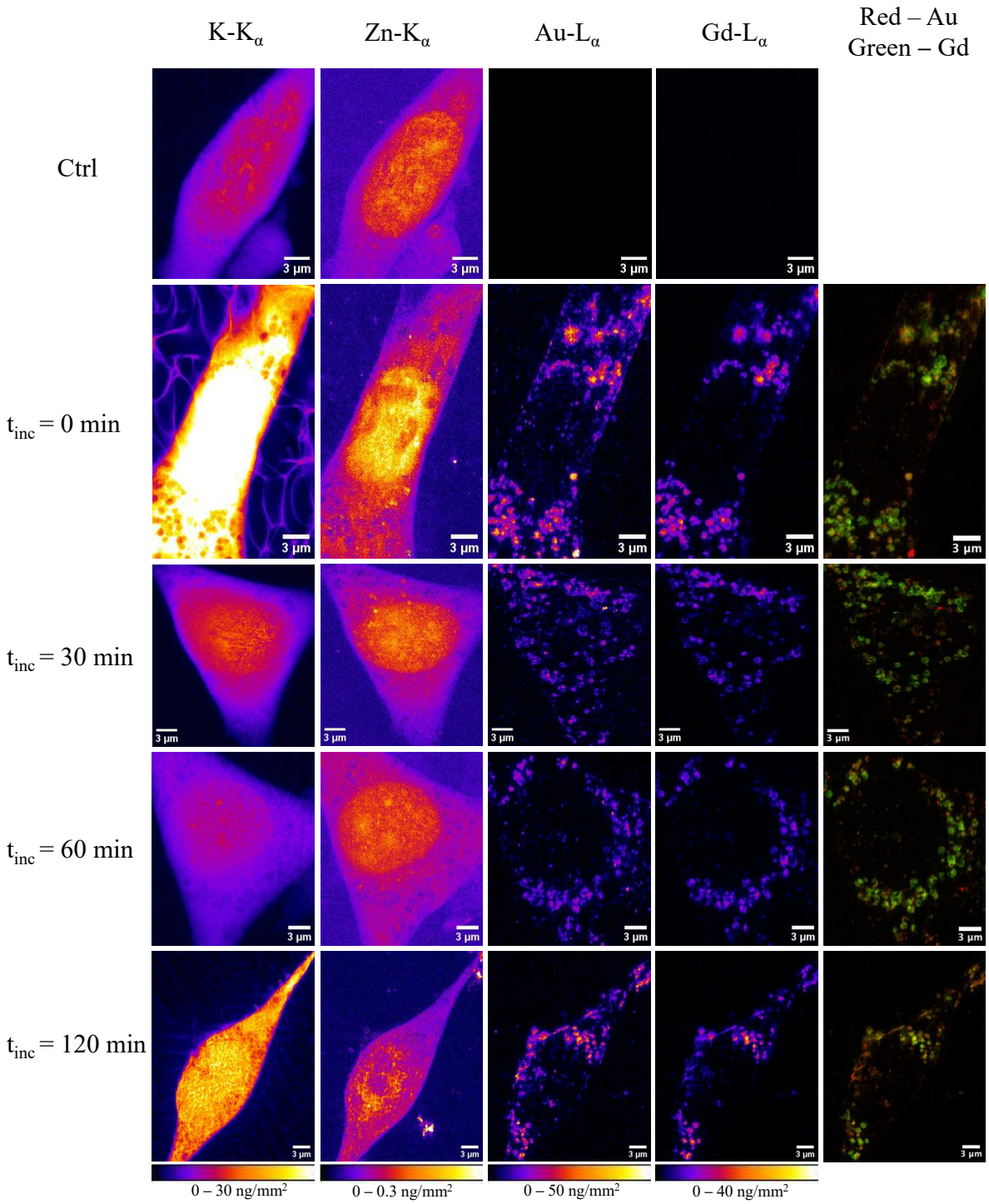

Figure 11: Pseudo colored images of 3T3 cells acquired by XRF-imaging. The signals originated from fitted: K K_α emission (first column), Zn K_α emission (second column), Au L_α emission (third column), and Gd L_α emission (fourth column). Fifth column shows a merged image indicates a high colocalization, whereas red originates from Au emission and green from Gd emission. The cells depicted in the first row are control cells without NP treatment. The following lines show one representative cell after 24 h of exposure with AuNP@CTPR-Gd (c_{Au} ~10 µg/mL) and different incubation times t_{inc} in NP free medium as indicated on the left. The scale bars indicate 3 µm.

An initial evaluation shows overlap between the L_α emissions from Au and Gd occurring inside cells. This finding is in accordance with the expected simultaneous uptake mechanism for the hybrid construct AuNP@CTPR-Gd, *i.e.* the preformed protein corona is endocytosed together with the NP cores. The granular structure of the NP distribution is in agreement with endocytotic uptake.[116–119] Both, Au and Gd elements appear to be mostly accumulated in multiple small areas (which is clearer in the Gd maps), which are attributed to lysosomes/endosomes.[120]

1.3.3.2.1 Analysis in whole cell

The absolute amount of Au and Gd and their ratio was determined for the whole cellular area, but a clear tendency showing the decrease or increase as a function of the incubation time could not be observed (Fig. 12). Nevertheless, a great degree of cellular variability in the Au/Gd ratio could be observed in the small population of cells studied, making it difficult to assess the results obtained. Yet, although the initial molar ratio of Au per Gd in AuNP@CTPR-Gd hybrids before they were added to cells was $c_{Au}/c_{Gd} = 26.8$, the values obtained from our XRF-imaging measurements after NP internalization by cells were around $c_{Au}/c_{Gd} = 2$. Such a low ratio was supported by ICP-MS based uptake experiments, which displayed similar quantities of Au and Gd per cell and a ratio of $c_{Au}/c_{Gd} = 0.9$. In general, this might indicate that the AuNP taken up during the 24 h treatment with AuNP@CTPR-Gd are excreted faster than the Gd labelled proteins, which is in line with fluorescence-based degradation studies and also experiments using polystyrene NPs.[60,61]

For further colocalization analysis, the elemental concentrations (ng/mm^2) of the XRF-imaging maps acquired were first converted into nmol/mm^2 by dividing the value of each pixel by the molecular weight of the element of interest. This allows for a more meaningful data interpretation by comparing the relative amounts of Au and Gd atoms. Masks marking the outline of each individual cell were generated from the Potassium XRF-imaging maps, and the colocalization between Au and Gd was calculated inside those areas to avoid any possible interference from the background signal. The Pearson's correlation coefficient r and the Manders' coefficients M_1 and M_2 were determined for whole cells (Fig. 12). For all colocalization analysis channel 1 and thereby M_1 is based on Au, whereas channel 2 (M_2) defines contribution from Gd.

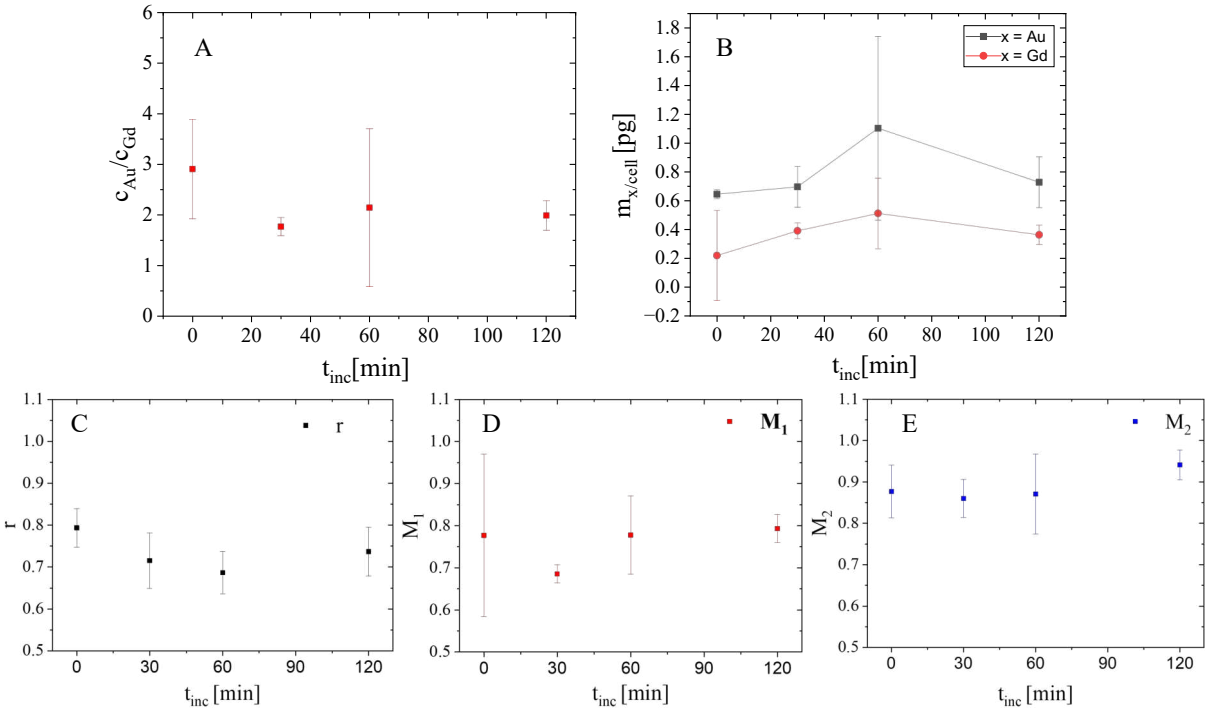

Figure 12: Molar ratio c_{Au}/c_{Gd} (A) and total elemental amount (B) of Au and Gd ($m_{Au/cell}$, $m_{Gd/cell}$) in whole 3T3 cells exposed to AuNP@CTPR-Gd (c_{Au} ~10 µg/mL) for 24 h, followed by different incubation times (t_{inc} = 0, 30, 60, and 120 min) in NP-free medium. Lower row illustrates consecutive colocalization between Au and Gd in these cells. The graphs show the Pearson's correlation coefficient *r* (C), the Manders' coefficient M_1 (D – relative proportion of Au overlapping with Gd), and the Manders' coefficient M_2 (E – relative proportion of Gd overlapping with Au).

Overall, all correlation coefficients show values > 0.6, indicating that Au and Gd are highly colocalized inside cells. Still, the Pearson's correlation coefficient r shows a slight decrease in its mean value within the first 60 minutes. This might imply a possible decomposition of the protein corona whereby proteins (as indicated by Gd) are removed from the surface of the NPs, as in that case the colocalization between both elements should decrease. Still, these variations are not statistically significant, proven by Students t-test ($p > 0.05$). This might be caused by the overall small populations in these studies (*i.e.*, three cells per condition) and the huge intrinsic cellular variability observed, which does not allow to establish proper statistics.
Besides, the mean values of M_1 as well as M_2 are nearly constant, characterized by a large error, and thus tolerate no accurate discussion of the results.

1.3.3.2.2 Analysis inside cellular vesicles

The same colocalization analysis was performed at the small circular areas inside cells, where most Au and Gd was found. These intracellular vesicles are most likely endosomes and lysosomes linked to the internalization process of the NPs. Previous experiments suggested that protein corona around NPs might get degraded in endosomes, during their maturation into lysosomes.[60,61,121] For the analysis at least 20 of those areas were automatically selected based on the Gd signal for each image using the FiJi software. This was done in order to avoid human-related bias in the selection of the regions of interest (ROI). All of the regions selected had a circularity ≥ 0.7, and showed a diameter smaller than 1 μm (area < 0.79 μm^2), as expected from cellular endosomes or lysosomes. Representative images showing the ROIs selected from cells exposed to AuNP@CTPR-Gd for 24 h and different subsequent incubation times t_{inc} in NP-free medium are shown in Fig. 13. Images showing the ROIs selected from all cells analyzed can be found Fig. A6.

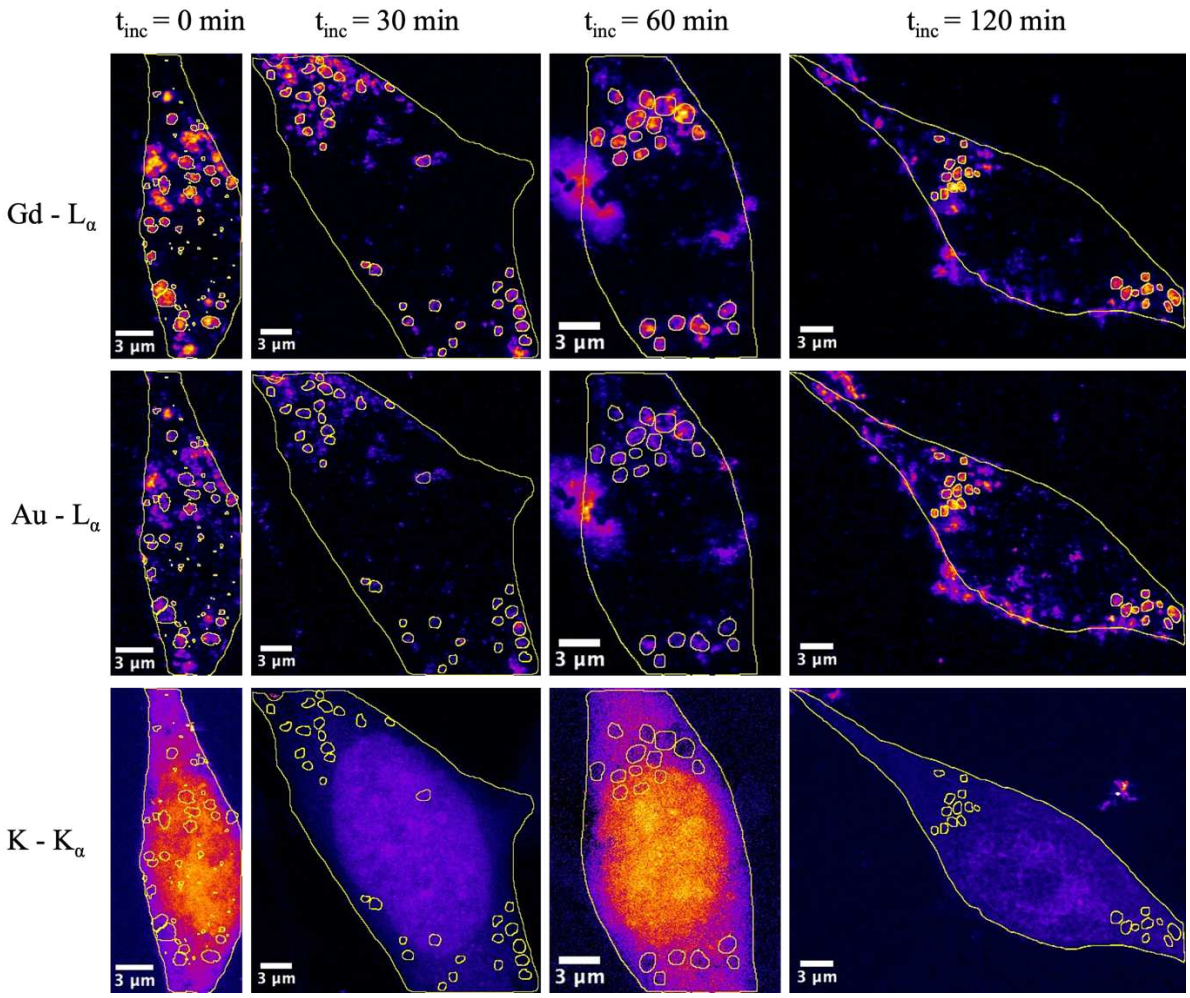

Figure 13: Pseudo colored images acquired by XRF-imaging from 3T3 cells exposed to AuNP@CTPR-Gd for 24 h (C_{Au} ~10 µg/mL) after subsequent incubation times t_{inc} in NP-free medium: t_{inc} = 0, t_{inc} = 30 min, t_{inc} = 60 min, and t_{inc} = 120 min. The signals originated from the Gd - L_α emission (first row), Au - L_α emission (second row) or K - K_α emission (third row). Regions of interest (ROI) in yellow stated as intracellular vesicles are defined for nearly spherical areas, showing a circularity ≥ 0.7 and an area smaller than 0.79 µm^2. The scale bars indicate 3 µm.

The Au to Gd ratios c_{Au}/c_{Gd} found in vesicles were always smaller than those obtained when whole cells were considered (Fig. 14 and Fig. 12). Therefore, a substantial fraction of intracellular Gd must remain located inside endosomes/lysosomes. Moreover, our analysis also showed that the molar ratio c_{Au}/c_{Gd} inside vesicles decreased over time; from an initial value of 1.51 ± 0.02 in cells (t_{inc} = 0), to 1.32 ± 0.01 after t_{inc} =120 min ($p = 0.014$). By calculating the elemental amount of Au and Gd in all the areas stated as vesicles, also a slight decrease of Au can be seen over time, whereas the amount of Gd stays at almost the same level (Fig. 14). These results are significant and seem to support degradation of the protein corona inside the vesicles,

followed by a faster removal of AuNP from them. Remarkable, small vesicle-like areas containing only Au are found close to the nuclei in all cells studied (see Fig. 11). Thus, vesicles seem to maintain the same quantity of Gd labelled proteins, but reduce their amounts of AuNP over time leading to decreased Au/Gd ratios. This corresponds to previous studies, where it was shown that a core size $d_c \approx 12$ nm still can be endocytosed sufficiently.[122–125]

Unfortunately, we cannot assess the degree of degradation of the protein corona in vesicles between the cell uptake of intact AuNPs@CTPR-Gd hybrids and the separation of AuNPs and CTPR-Gd at nuclear areas. Still, differential cellular processing for AuNPs and CTPR-Gd is only observed in areas close to the nuclei, which might indicate that cells cannot treat particles and proteins as individual entities. Thus, some of the initial protein corona might be still existing during intermediate stages of the cellular trafficking.

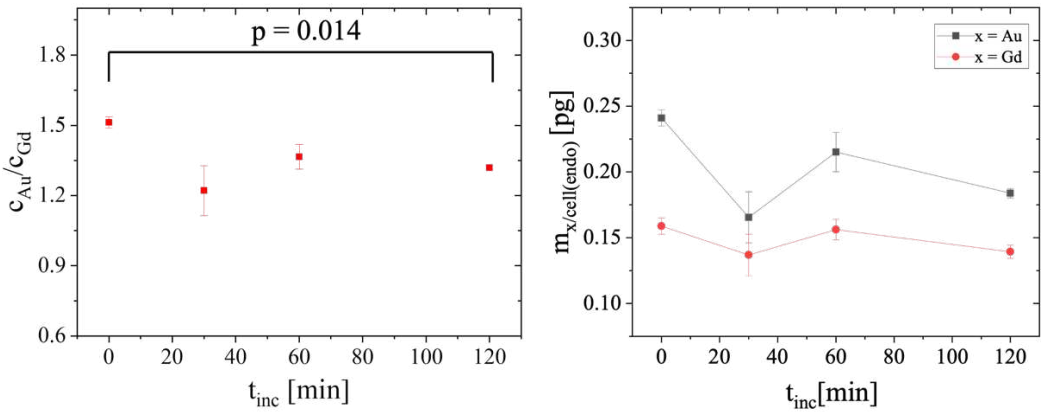

Figure 14: Molar ratio c_{Au}/c_{Gd} of Au/Gd (left) and the total amount (pg/cell) of Au and Gd (right) inside structures stated as vesicles (at least 20 *per* cell) $m_{X/cell(endo)}$ (X = Au, Gd) in 3T3 cells exposed to AuNP@CTPR-Gd (C_{Au} ~10 µg/mL) followed by different incubation times in NP-free medium (t_{inc} = 0, 30, 60, and 120 min).

An analysis of the Au-Gd colocalization in vesicle areas is shown in Fig. 15. A small decrease in the values of PCC (r) and Manders' coefficient 1 (M_1; the relative proportion of Au overlapping with Gd) could also be detected over time, supporting again the possible decomposition of the protein corona inside vesicles, *e.g.*, endosomes or lysosomes, suggested by the changes in the Au/Gd ratios. However, no change was observed for Manders' coefficient 2 (M_2; relative proportion of Gd overlapping with Au) at different incubation times. Previous reports proposed that after degradation, NPs get separated from the detached proteins that had originally formed the corona and are trafficked into vesicles that excrete them from the cell, or

other organelles where they might accumulate for some time.[126] This could explain the decrease of r and M_1 during the incubation period, as AuNP would leave the initial endosomes/lysosomes, and no new AuNP@CTPR-Gd would be internalized by cells to maintain the correlation between Au and Gd in vesicles. Instead, CTPR-Gd proteins would stay inside the initial vesicles, as proteins desorbed from the NPs' surface during this time scale might not be able to escape, so (keeping the spatial resolution of 70 nm x 70 nm in mind) no observable change might be detected in M_2.

Nevertheless, again these results were obtained from small cell populations (*i.e.*, three cells per condition), and thus differences in colocalization coefficients could not be considered significant (Students *t*-test: $p > 0.05$) due to cellular variability, making it impossible to obtain relevant conclusions.

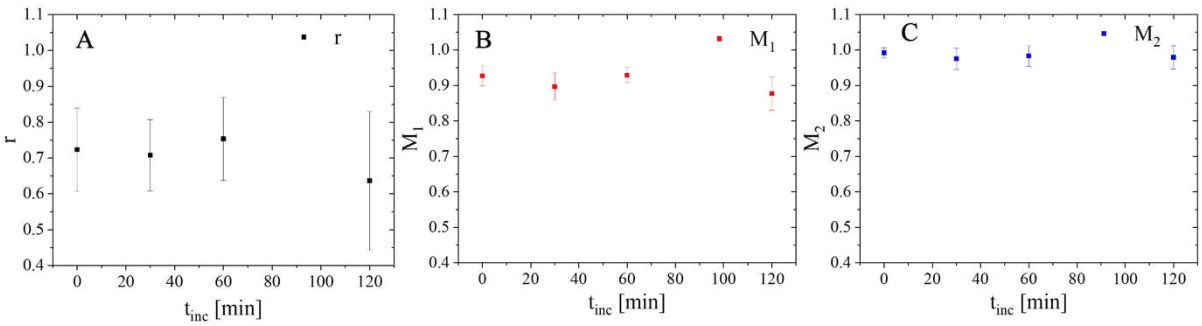

Figure 15: Colocalization between Au and Gd inside structures stated as vesicles (at least 20 *per* cell) in 3T3 cells exposed for 24 h to AuNP@CTPR-Gd (C_{Au} ~10 µg/mL) followed by different incubation times in NP-free medium (t_{inc} = 0, 30, 60, and 120 min). Graphs show Pearson's correlation coefficient r (A), Manders' coefficient M_1 (B – relative proportion of Au overlapping with Gd), and Manders' coefficient M_2 (C – relative proportion of Gd overlapping with Au).

1.3.3.2.3 Analysis dependent on distance to nucleus

During cellular internalization, AuNP@CTPR-Gd would be trafficked by maturing endosomes from distal regions of the cell into areas closer to the nucleus. As such, degradation of the protein corona during cellular transport might be observed as possible changes in the relative accumulation of the AuNP and CTPR-Gd proteins in regions distal and closer to the nucleus. Therefore, each cell image was divided into a number of ROIs, defined as 1 µm width bands with increasing separation to the cellular nucleus. Since cells show a variety of sizes, no ROIs were defined farther than 6 µm from the nucleus, as this allowed the study of at least three cells

for every sample group. Representative images showing the regions of interest selected from cells exposed to AuNP@CTPR-Gd for 24 h and different following incubation times in NP free medium are shown in Fig. 16. Images showing the ROIs selected from all analyzed cells can be found in Fig. A7 and Fig. A8. As images are two dimensional, it should be noted that there is no way to determine whether an element is found inside or outside the nucleus.

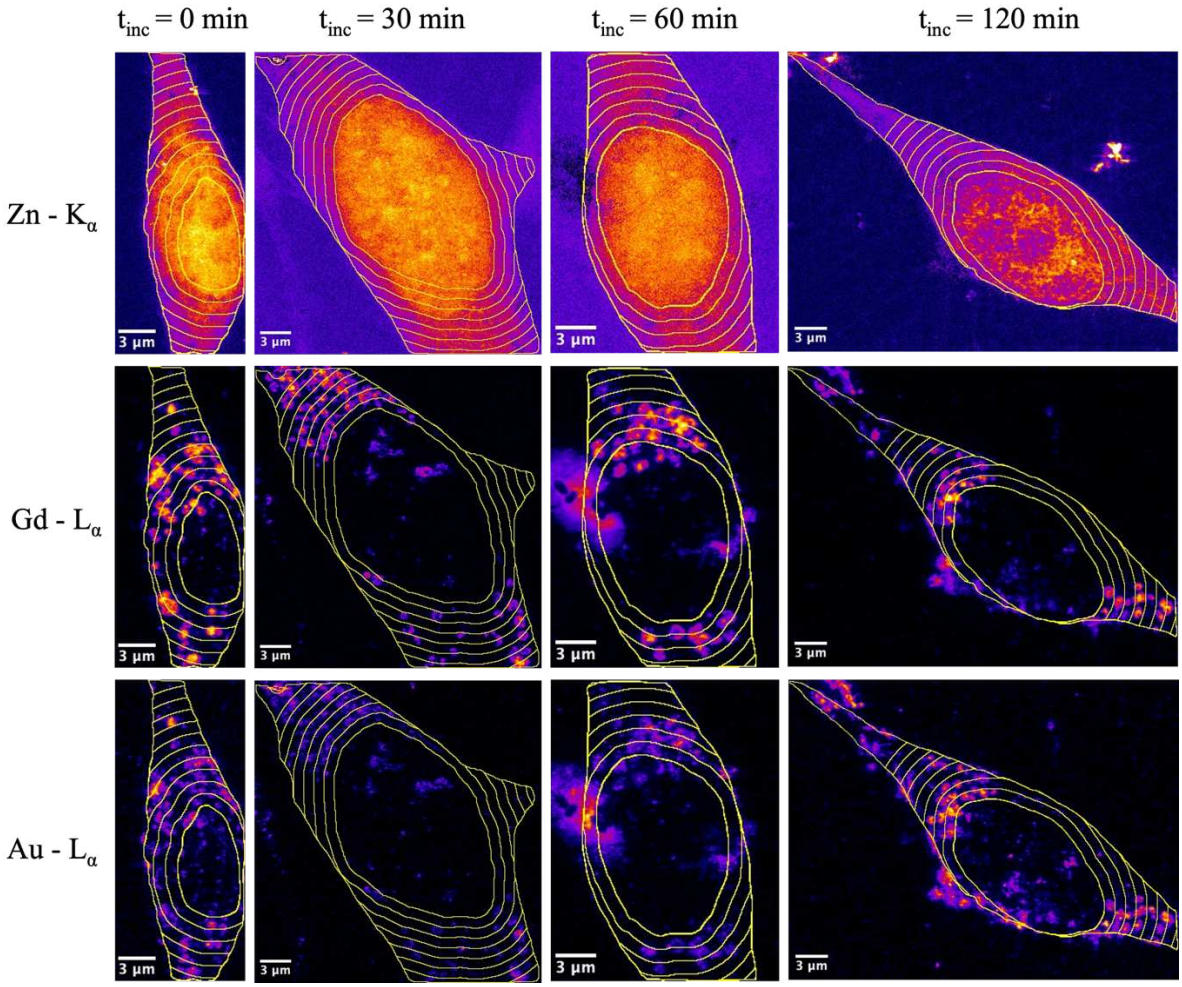

Figure 16: Pseudo colored images acquired by XRF-imaging from 3T3 cells exposed to AuNP@CTPR-Gd for 24 h (C_{Au} ~10 µg/mL), followed by incubation in NP free medium for the time t_{inc}: t_{inc} = 0, t_{inc} = 30 min, t_{inc} = 60 min, and t_{inc} = 120 min. The signals originated from the Zn K_α emission (first row), Au L_α emission (second row), or Gd L_α emission (third row). ROIs are generated by defining the cellular nucleus as center (identified from the Zn K_α emissions maps), the outer cellular membrane as border (identified from the K K_α emissions maps), and sectioned into rings with a width of 1 µm. The scale bars indicate 3 µm.

The absolute amount (Fig. A9) and molar ratios of Au to Gd (Fig. 17) were determined for each of these areas with increasing distance d_{nuc} to the cellular nucleus. Remarkably, the Au/Gd ratios increased from areas in the outside of the cell towards those in the proximity of the nucleus. Such spatial dependence seems to support the hypothesis that the initial protein corona is removed from the NP surface during cellular trafficking, leading to different cellular processing of AuNP and CTPR-Gd proteins. Moreover, as the Au to Gd ratio is normally smaller in areas defined as vesicles than in the proximity of the nucleus, our analysis also suggest that some AuNP must be capable of escaping endocytic vesicles and/or be transported or accumulated into different organelles. This can explain the presence of vesicle-like areas containing only Au close to the nuclei in all cells studied (see Fig. 11).

It has been reported that vesicles containing NPs are able to fuse with organelles related to the cellular secretion pathways, *e.g.* Golgi apparatus or rough endoplasmic reticulum, whereas the following fate is not fully revealed.[126] These organelles are close to the nucleus. Interestingly it was also shown that 12 nm AuNP modulate the function of the endoplasmic reticulum.[127] Moreover, supporting our findings, electron microscopy studies examinating the localization of 12 nm AuNP show an accumulation of most NPs inside vesicles in close proximity to the cellular nucleus.[128]

However, although the highest Au/Gd ratios within cells are always found near the nuclei for all time points studied (Fig. 17), there is a significant (Student's *t*-test: $p < 0.05$) reduction over time on the relative amount of Au to Gd in those areas. The Au/Gd ratios near the nuclei go down from $c_{Au}/c_{Gd} = 3.3 \pm 0.5$ at 24 h exposure without additional incubation time in NP-free medium, to 1.9 ± 0.3, 2.0 ± 0.3 or 2.8 ± 0.4, for 30, 60, or 120 min incubation time, respectively. As such, it might be possible that over the 24 h of cellular uptake of AuNP@CTPR-Gd cells reached a steady state with slightly higher Au amount near the nucleus and a fully homogenous Gd distribution in the cell (Fig. 18). Yet, 30 minutes after stopping the uptake of new NPs the quantities of both Au and Gd increased in the nuclear area (Fig. 18), while Au/Gd colocalization decreased as shown by their r, M_1 and M_2 coefficients (Figure A10). This indicates separate intracellular processing for AuNP and CTPR-Gd proteins. Furthermore, during the following $t_{inc} = 90$ min of incubation the amount of Au and Gd is redistributed all over the cell, possibly preparing AuNP for efflux and CTPR-Gd proteins for further digestion.[61]

Unfortunately, clear evidence of this process could not be drawn due to the limited sample population causing high standard deviations, and thus our arguments remain speculative.

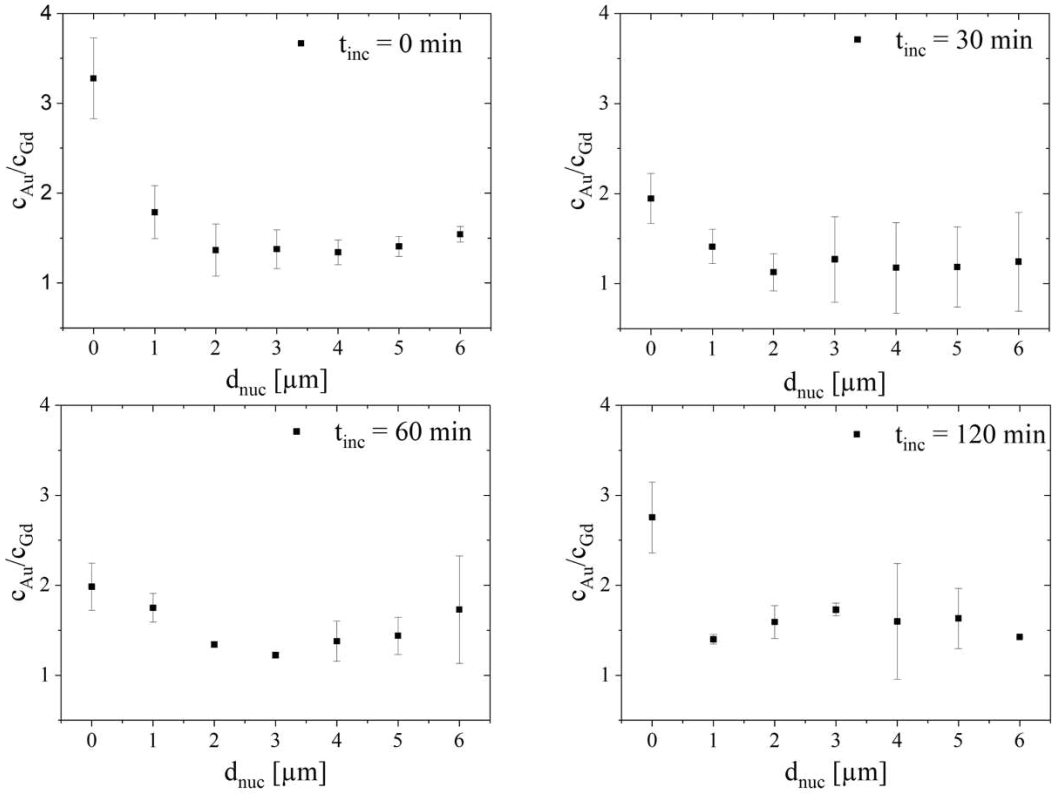

Figure 17: Molar ratio c_{Au}/c_{Gd} of Au/Gd according to the distance d_{nuc} to the cellular nucleus in 3T3 cells exposed to AuNP@CTPR-Gd (c_{Au} ~10 µg/mL) followed by different incubation times in NP-free medium (t_{inc} = 0, 30, 60, and 120 min).

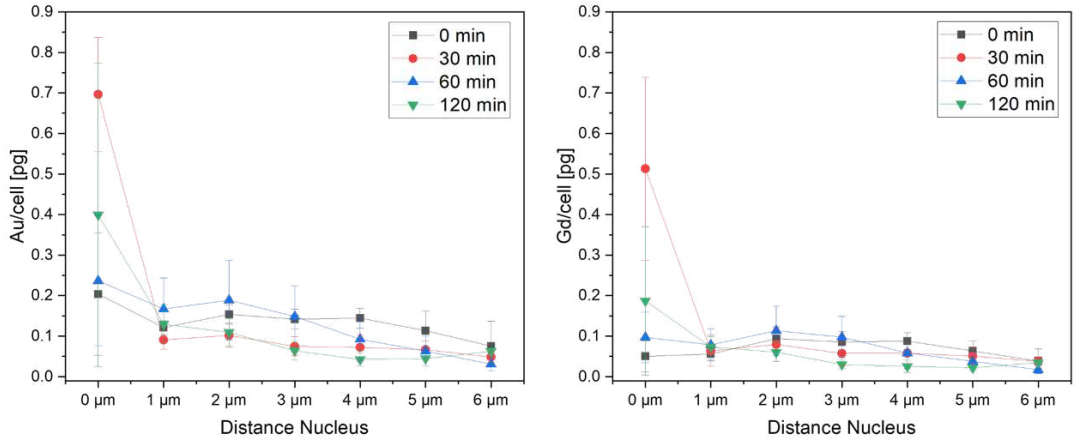

Figure 18: Elemental amount of Au (left) and Gd (right) according to the distance d_{nuc} to the cellular nucleus in 3T3 cells exposed to AuNP@CTPR-Gd (c_{Au} ~10 µg/mL) followed by different incubation times in NP-free medium: t_{inc} = 0 min - black, 30 min - red, 60 min - blue, and 120 min - green). Individual plot for each incubation time and element can be found in Tab. S3.

1.3.3.2.4 Post-hoc sample size estimation

The large cell variability and small sample populations have been an issue throughout this study, hindering the capacity to obtain meaningful conclusions from some of the analysis performed on the data. Unfortunately, this problem is not unique to this experiment. Currently, most XRF-imaging-based experiments intending to obtain subcellular information need to settle for long acquisition times *per* sample to achieve the spatial resolution required. Thus, reducing the maximum size of the sample population possible to achieve, and the scope of the study itself.
As a theoretical exercise, we estimated the sample size required to achieve meaningful results on the intracellular degradation of the protein corona in a hypothetical future experiment. To do this, we used a statistical approach, commonly used to compute group sizes for clinical trials, that was performed using the G*Power software.[129] As an example, the PCC's (r) obtained from our current experiment were projected as a normal distribution with a FWHM of their standard deviations. From this a post-hoc analysis calculated the individual power (Cohens *d*), as a measure for the difference in two populations.[130] After extracting all *d* values, an a priori simulation can calculate the minimum sample size for each incubation time to have a significant difference. In the case of the whole cell area analysis, these calculations lead to the finding that at least 6 cells needed to be measured in the most different case, 0 *versus* 60 min incubation time, 13 cells by comparing 0 *versus* 30 min incubation time and in the most similar scenario, 0 *versus* 120 min incubation time, 20 cells are required for each study group.
Unfortunately, currently it might be challenging to obtain images of such a large number of cells within the timeframe of a normal experiment using the setups and capabilities of nanoprobe beamlines open at this time.[131–134]

1.3.4 Conclusion

In this study, pegylated AuNP with a core diameter of 12 nm and a preformed corona of engineered proteins labeled with Gd surrounding them were probed inside mammalian cells using synchrotron nanofocused XRF-imaging. Our analysis shows that the colocalization between Au and Gd on whole cells decreased over time, although to a very limited degree, while a meaningful reduction on the Au/Gd ratio inside vesicles was also observed over time. Additionally, higher Au/Gd molar ratios were found in areas close to the nuclei than in those far from it, but those differences across cells were reduced after they stopped internalizing

AuNP@CTPR-Gd. Data interpretation was complicated due to large cell to cell variance. Still, our results seem to indicate degradation of the protein corona during the trafficking (and endosomal maturation) of AuNP@CTPR-Gd hybrids after vesicle-related cellular uptake at the outer membranes. Moreover, our data also suggests different cellular processing for AuNP and CTPR-Gd proteins, as supported by the absolute decrease in the amount of Au inside the vesicles over time.

Overall, this work demonstrates that XRF-imaging can be used to study the intracellular fate of the protein corona, and might be a valid tool to investigate other dynamic processes inside cells. Nevertheless, it is worth mentioning that the current technical capabilities of most hard X-ray nanoprobes impose long acquisition times to obtain single images with subcellular resolution, limiting the maximum sample size of the cell populations studied. It is possible to obtain some meaningful results with such sample size (as we did), but in general it makes it difficult to overcome the inherent cell to cell variance and can hamper the application of XRF-imaging to other cellular processes. Therefore, new technical advances allowing faster acquisition times of images with subcellular resolution would be beneficial to extend the use of XRF-imaging for the study of dynamic biological processes at cellular level.

1.4 Anomalous X-Ray Scattering Investigation of triple labeled Nanoparticles

Furthermore, understanding the fate of the ligands that stabilize the NPs is essential as they play a key role in determining the overall stability, biodistribution, and interaction of the nanoparticles with biological entities. Ligands can influence the targeting capabilities and cytotoxicity of NPs, thereby effecting their therapeutic efficacy and safety profile. The structure, charge, and hydrophilicity of the ligands are fundamental parameters that dictate how the NP interacts with cellular membranes, potentially enhancing or inhibiting cellular uptake depending on the design.[135–137] In addition, ligands can be engineered to achieve specific biological responses, acting as functional moieties for active targeting or as stealth components to evade immune recognition, making understanding their fate critical to the safe design of NPs for medical purposes.[138–140]

Recent studies have used fluorescent markers to label each component (NP, ligand, protein) within single cells, revealing distinct degradation pathways for each component.[60] However, due to limitations in penetration depth with fluorescence-based techniques, subsequent studies have turned to radioactive labeling. Radioactive labeling offers the advantage of deeper tissue penetration, allowing for the tracking of NP components in more complex biological systems and over longer periods of time. This provides insights not only into the initial distribution but also into their metabolic fate and clearance pathways of the NPs. An example is provided by projects using radioactive labeling to track these components individually after administration in mice. The results showed that the polymeric shell can be partially degraded by proteolytic enzymes, with the resulting fragments being gradually excreted through the kidney. In addition, radiolabeling of the protein corona here shows that the adsorbed proteins are released from the surface, following a distinct biodistribution before almost complete clearance within a few days.[141–143] To complement these insights, the use of advanced synchrotron-based techniques such as anomalous small angle X-ray scattering (aSAXS), can support a detailed understanding of the structural hierarchy of NPs. aSAXS enables the precise measurement of each constituent layer, including the AuNP core, ligand, and the protein forming the corona. By identifying the size of each layer provides indispensable data on the assembly and stability of NPs in a biological environment and could help to understand their *in vivo* fate. This understanding is crucial for tailoring NPs to either disassemble in a controlled manner for drug release or maintain their integrity for imaging applications. The use of X-ray scattering techniques is

advantageous as it can be used for both, *in vivo* and *in vitro* scenarios. Furthermore, it has been demonstrated that SAXS experiments can be used to obtain images of large areas (*e.g*. bone, teeth, soft tissue) down to the cellular level.[144–146] Such a comprehensive approach could bridge the gap between laboratory models and real-world biological systems.

The subsequent section will present the fundamental principles of the technique, followed by showcasing the results of a proof-of-concept study. Therein various mixtures of amino-PEG and brominated PEG are characterized regarding their formation of a protein corona with an Gd-bearing engineered protein. The amino group promotes electrostatically the formation of a protein corona, while the bromine atom acts as a label for the aSAXS analysis. In addition, proteins were directly covalently bound to the AuNPs, without any ligand, to serve as a positive control.

1.4.1 Small angle X-ray scattering

In principle, the interaction of X-rays with matter can be divided into two distinct principles – scattering and absorption, although in reality a combination of both occurs.[147] While absorption has been discussed in more detail in a previous chapter, the focus of this section is on the scattering of X-rays by matter. Specifically, when X-rays interact with the electrons of the material, the incident photons can be deflected and cause a change in their trajectory without a loss of energy. This process is known as elastic scattering – called Thompson scattering in case of X-rays, Rayleigh scattering in case of visible light. In contrast, other phenomena such as inelastic scattering involve a change in energy, or absorption involves a complete depletion of the energy of the initial photons by the material. For elastic scattering, the associated wave vectors (k) of the incident and scattered photons are of particular interest. Although their magnitude remains unchanged, their directions differ as a result of the momentum transfer.[148,149] This relationship can be expressed mathematically by introducing the wave vectors $\vec{k}_i$ and $\vec{k}_s$ for the incident and scattered photons with the wavelength λ, respectively.

$$\left|\vec{k}_i\right| = \left|\vec{k}_s\right| = \frac{2\pi}{\lambda} \tag{1}$$

The corresponding momentum transfer of the elastically scattered photon, hereafter referred to as the scattering vector $\vec{q}$, can consequently be expressed as:

$$\vec{q} = \vec{k}_s - \vec{k}_i \tag{2}$$

However, since this value is not directly accessible experimentally the importance of the angular dependence is derived. This angular dependence allows to correlate the spatially arranged scattering patterns at a detector with specific structural features of the sample. Considering that the incident wave vector $\vec{k}_i$ is directed along the incoming photon direction, the scattered wave vector $\vec{k}_s$ forms an angle of 2 θ with respect to the incident direction. Thus, obeying, Equation 2 we can therefore express the resulting scattering vector $\vec{q}$ as:

$$|\vec{q}| = \sqrt{|\vec{k}_i|^2 + |\vec{k}_s|^2 - 2\,|\vec{k}_i|\,|\vec{k}_s|\,\cos(2\theta)} \tag{3}$$

Now, considering that the energy of the scattered photon does not change (Equation 1) and applying general trigonometry, the magnitude of the scattering vector can be projected in terms of the incident wavelength and the scattering angle as follows:

$$|\vec{q}| = \frac{4\,\pi \sin(\theta)}{\lambda} \tag{4}$$

Since the scattering information is obtained in reciprocal space, it is mostly necessary to convert the scattering vector into real space. This conversion can be further derived by applying Braggs' law (Equation 5) to the derived expression. Thus, leading to the relationship between the scattering vector *q* and the characteristic distance in real space *d* (Equation 6).

$$\lambda = 2\,d \sin(\theta) \tag{5}$$

$$q = \frac{2\,\pi}{d} \tag{6}$$

As seen in Equation 6, the scattering pattern shifts to smaller *q*-values for larger particles (large *d*) whereas smaller particles scatter at larger *q*-values. Consequently, it becomes clear that the characteristic distance of scatterers directly influences the scattering angle (Equation 4). This principle highlights the difference between wide angle X-ray scattering (WAXS) and small angle X-ray scattering (SAXS). While WAXS is sensitive to interatomic distances – often described by Bragg's law of diffraction, which explains constructive interference on a

crystalline lattice – SAXS is particularly sensitive to the overall size and shape of particles. With SAXS, larger structures, aggregates or particles in the nanometer range can be examined by detecting small scattering angles, corresponding to small q values.

As described before, q is however not directly experimentally accessible. But as the wavelength is well-known in a typical experiment, the magnitude of the scattering vector can be directly assessed by measuring the intensity of the scattered X-rays as a function of the angle θ (Equation 4). Following an azimuthal integration of the 2-D scattering pattern to enhance the signal to noise ratio, the intensity of the detected, scattered photons, can be transferred into a 1-D intensity curve as a function of q as schematically illustrated in Fig. 19 below.

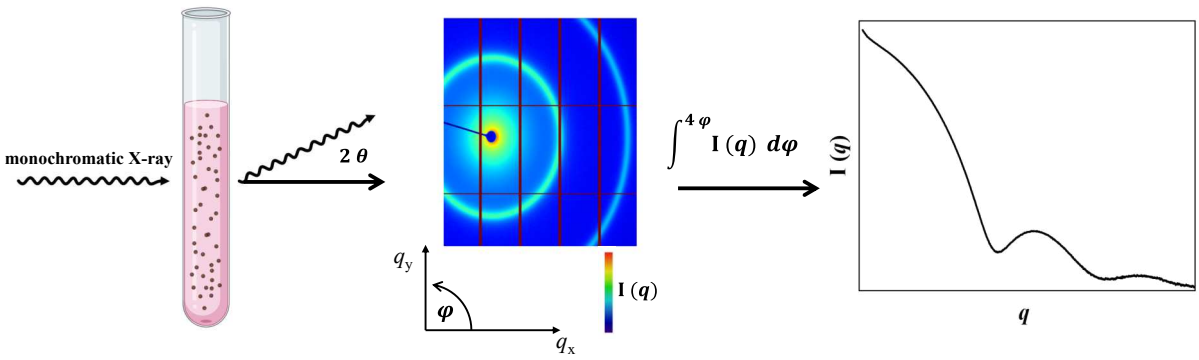

Figure 19: Schematic illustration of the process of elastic X-ray scattering from a sample, producing a characteristic scattering pattern on a 2-D detector. The azimuthal integration over φ of this 2-D scattering pattern yields a typical SAXS curve, plotting the intensity (I) as a function of the scattering vector (q). The image of the area detector shows the shadow of a beam stop, implemented in the setup to avoid direct exposure of the detector elements by the transmitted beam.

The intensity of the scattered signal is in first instance proportional to the number of electrons in the illuminated volume, as the probability of scattering events increases with a higher number of electrons. However, considering the intensity as a function of the number of electrons alone, the SAXS curve would provide only limited information. Since the wavelength of the incident and scattered photon are similar in an elastic process, also interference phenomena can occur. Constructive interference effects appear when the scattered waves from different parts of the sample are in phase with each other. In such cases, their amplitudes add up constructively, which leads to a clear signal increase - a peak - in the scattering pattern. Destructive interference, on the other hand, where the waves are out of phase, leads to a weaker signal or a minimum in the scattering intensity.[150]

In a typical SAXS curve of inorganic particles, the scattering pattern is predominantly influenced by two main components: the form factor P(q) and the structure factor S(q). The total scattering intensity is thus proportional to the product of these two parameters. The form factor can be understood by considering the scattering of one individual particle composed of many atoms. This scattering arises from the interference pattern produced by the scattering from each electron within the particle. This resulting scattering pattern oscillates characteristically for the shape/form of the particle. Considering solely one form of particles present, the overall size of the particle (largest distance between electrons) determines thereby the angle at which the scattering from constructive interference occurs (Fig. 20A). Mathematically, this concept arises from the Fourier transformation of the electron density.[151] However, in practice, numerous particles are illuminated simultaneously, leading to an averaged SAXS curve that is composed of contribution from different form factors of particles with different sizes. The relative polydispersity, a measure for the particles size distribution, can be extracted from a SAXS curve, as it highly correlates with the shape of the curve dependent on the form factor. Variations in particle sizes influence the q-value of the typical oscillations, resulting in a broadening of the oscillations rather than sharp peaks (Fig. 20B).[152,153]

When the number of particles exceeds a certain concentration, also interference from particles between each other must be considered. This interaction is described by the structure factor S(q), which represents the collective behavior of the particles in the sample. The structure factor represents a pair distribution function, which calculates the probability to find another particle/scatterer at a certain distance from each other. In a dilute system therefore, neglecting particle-particle interactions, the structure factor becomes 1 and solely the form factor contributes to the measured scattering pattern.[154]

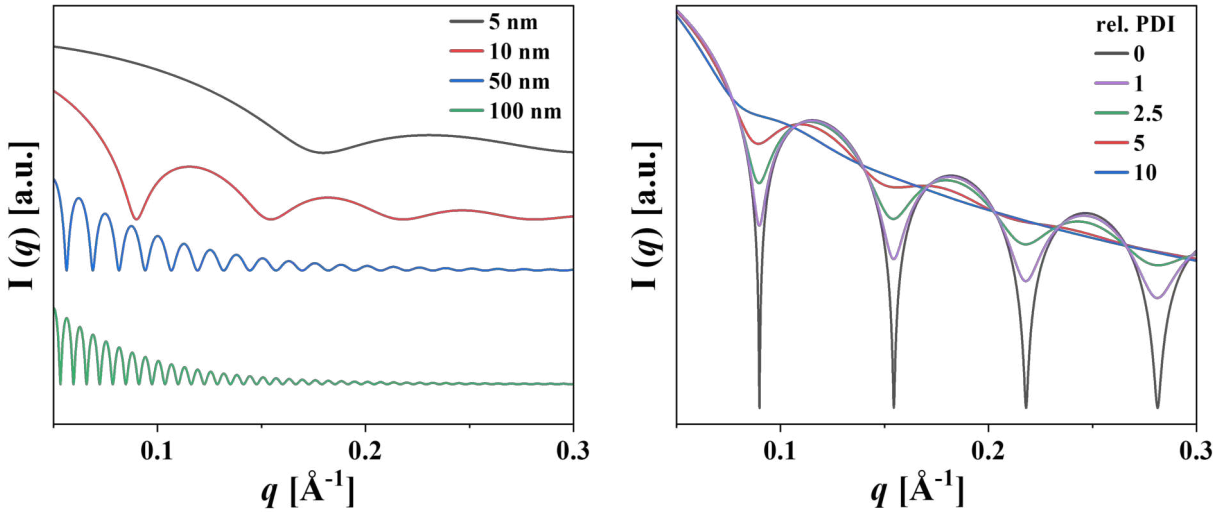

Figure 20: A) Simulated scattering intensity of spherical nanoparticles as a function of the scattering vector q, neglecting the structure factor S. Different colors represent different nanoparticle diameters. B) Simulated scattering intensity of nanoparticles with a diameter of 10 nm for different relative polydispersity indices (PDI).

1.4.2 Anomalous small angle X-ray scattering

The previous section described the fundamentals of SAXS, based on the measurement of the scattering intensity of elastically scattered X-rays with a constrained incident photon wavelength. So far, the influence of the size, shape and polydispersity for the scattered intensity as a function of q was discussed. However, the electron clouds as origin of scattering, were considered to be free, and consequently no interaction between the electrons and the bound atoms was considered. In reality, electrons are not simply free to respond passively to the incident X-rays as they are confined in orbitals. When the oscillatory frequency of the incident photons approaches the eigenfrequency of an atomic orbital, the induced electron vibration can resonate with a transition to other accessible orbitals. This can either result in the photo-absorption, as discussed above, but more important for our current focus, it can perturb the atomic scattering. This resonance near the element-characteristic absorption edge introduces significant changes in the scattering behavior, which is the underlying principle of anomalous SAXS (aSAXS).[155,156] These anomalous contributions (f^{Δ}) to the scattering behavior due to orbital interactions, lead to a more realistic description of the overall atomic scattering factor (f) in respect to the scattering (f^{0}), ignoring dispersion and absorption (Equation 6):[157–159]

$$f = f^0 + f^\Delta \tag{6}$$

This so-called anomalous scattering correction (f^Δ) can be decomposed into two parts: the real component *f'* and the imaginary component *f''*:

$$f^\Delta(E) = f'(E) + i\, f''(E) \tag{7}$$

The real component, known as dispersion corrections, accounts for changes in the phase velocity of the incident X-rays as their frequency approaches the eigenfrequency of the bound electrons, resulting in a phase shift of the scattered wave. The imaginary component *f''* can be termed absorption correction. This component describes the reduction in the amplitude of the scattered wave as a result of the energy loss due to an absorption process.[160] Thereby it becomes evident that both components are strongly energy dependent and change significantly near an absorption edge. Both components are shown below as a function of the energy, near the Au L3 absorption edge at 11,919 eV (Fig. 21A).

This energy dependent influence of the overall scattering intensity is exemplary shown for one sample, containing AuNPs, measured at different incident energies near this absorption edge (Fig.21B). As clearly seen in low q-values, and also in the inlet for a detailed view of the first prominent characteristic peak, the scattering intensity changes significantly as a function of the energy.

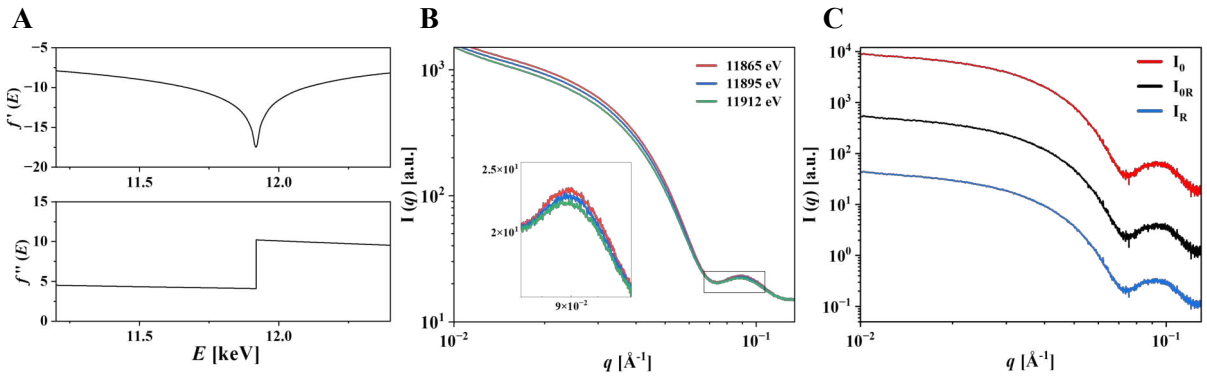

Figure 21: A) Energy dependence of the real (*f'*) and imaginary (*f''*) contribution of the atomic scattering function. Data extracted from NIST.[87] B) Recorded scattering intensity of a gold nanoparticle solution as a function of the scattering vector (q) at different incident energies near the Au L3 absorption edge. C) Deconvolution of the scattering curves of B), leading to the non-resonant scattering (I_0), a mixed scattering (I_{OR}), and the resonant scattering (I_R) intensity.

An approach to deconvolute different scattering components and thereby provides element specific contrast was introduced by Stuhrmann.[161] This method is based on the assumption that the total scattering intensity I (*q, E*), as the absolute square of the magnitude of the scattering amplitude (*A*) can be expressed as a sum of various contributions:

$$I\,(E,q) = \,|A(q,E)|^2 = \,I_0(q) + \,I_R\,(E,q) + \,I_{0R}\,(E,q) \tag{7}$$

Here (I_0) represents the non-resonant scattering contribution, while (I_R) describes the solely resonant contribution and (I_{0R}) as a cross term of superposition of both contributions. By measuring scattering curves with at least three energies (E_1, E_2, E_3) near the absorption edge of an element constitutes the following vector equation:

$$M_{i,j}\,(q,E) \bigotimes \vec{A}_j(q) = \,M_{i,j} \bigotimes \begin{bmatrix} |A_0\,(q)|^2 \\ Re\left(A_0(q)A_R(q)\right) \\ |A_R\,(q)|^2 \end{bmatrix} = \begin{bmatrix} I\,(q,E_1) \\ I\,(q,E_2) \\ I\,(q,E_3) \end{bmatrix} \tag{8}$$

With $M_{i,j}$ as a matrix including the energy-dependent anomalous scattering corrections f' and f'' for the certain energies. The column vector $\vec{A}_j$ contains the unknown scattering amplitudes, with A_0 for the non-resonant, and A_R for the resonant contribution.[162,163] To solve this system of linear equations, a gaussian elimination method can be employed to systematically reduce the system and retrieve all unknown parameters by back substitution. Alternatively, the eigenvector problem can be addressed, while more complex, offers a greater numerical stability and deeper insights into the data structure.[164] This approach enables similarly the extraction of the individual scattering components, but reduces the impact of measurement errors and provides robustness when using multiple energies for the aSAXS measurement. The so retrieved intensity contributions from the SAXS curves near the Au absorption edge (Fig. 21B), are exemplary shown in Fig. 21C.

Following this comprehensive discussion of the basics of (anomalous) small angle X-ray scattering and the meaning of the obtained scattering curves, the following paragraph explains how detailed information about the investigated sample can be obtained. Various fitting and modeling techniques are used to analyze and interpret the experimental data. A common and widely used method of data analysis is the use of mathematical models that allow theoretical scattering intensities to be calculated and compared with the acquired experimental data.

Although simple techniques, such as the Guinier approximation[165], can be used for the basic determination of parameters, such as the radius of the particles, an exclusively model-based fitting approach is pursued in this work. This approach leverages the previously discussed relationship between the intensity as a function of q and the scattering particles characteristics, such as size, shape or polydispersity. Although the Levenberg-Marquardt algorithm is widely used to fit experimental SAXS data, the Differential Evolution Adaptive Metropolis (DREAM)-fitting model was used for all data in this work. DREAM employs multiple parallel solution paths and systematically combines them to effectively find the best parameters, but at the cost of higher computational resources.[166,167] The algorithm stops iterating when the parallel solution paths converge, indicating that the optimal solution has been found. Compared to the Levenberg-Marquardt algorithm, this minimizes the risk of getting stuck in local minima and thereby leads to more robust and reliable results.

1.4.3 Materials

Sodium citrate (Sigma), Gold (III) chloride trihydrate (Sigma), Ethylenediaminetetraacetic acid disodium salt (Sigma), Citric Acid (Sigma), Bromine-PEG-thiol (Rapp Polymere), Amine-PEG-thiol (Rapp Polymere), Dithiothreitol (Sigma).

1.4.4 Methods

For this project, the synthesis and characterization procedures for the nanoparticles are identical to those previously described in detail in the Methods section 1.3.2. In short, to avoid redundancy, the nanoparticles were synthesized using an adjusted Turkevich method.[105] Prior to synchrotron scattering experiments the nanoparticles were characterized by transmission electron microscopy, dynamic light scattering, laser Doppler anemometry, and UV-visible absorbance spectroscopy. Any specific modifications or additional steps unique to this project will be highlighted in the relevant sections below.
Protein design, expression, Gd labeling and characterization was solely conducted by G. Guedes and A. L. Cortajarena. As the same protein was used for both experiments discussed this chapter, information can be found in supporting information of Ref.[104]

1.4.4.1 Covalent binding of proteins onto AuNPs

The formation of a protein corona around gold nanoparticles consisting of covalently immobilized proteins was adjusted from previously published protocols on inorganic 2D surfaces or semiconductor quantum dots.[168–170] Therefore, 500 µL PBS containing 7.5 nmol protein and 5 µmol dithiothreitol (DTT) were mixed and incubated for five minutes. Following, the protein was separated from DTT via size exclusion chromatography column. The protein was taken up in 1 mL miliQ water and subsequently 300 µL citrate stabilized AuNPs (100 nM) were added. The solution was left at 4°C overnight, followed by a cleaning procedure by centrifugation (25 000 rcf, 10 min) and exchanging the supernatant with PBS.

1.4.4.2 aSAXS experiments

Scattering experiments were conducted at SAXSMAT beamline P62 at DESY Petra III, Hamburg.[171] Therefore the nanoparticles were incubated at least one hour prior the measurement in deionized water, containing Gd-bearing proteins (at a 500:1 protein to NP

ratio). SAXS spectra were collected in five repetitions (each 0.5 s acquisition time) at four different energies before and/or after the Au-L3 edge (11,815 eV; 11,865 eV, 11,895 eV; 11,912 eV), Br-K edge (13,345 eV; 13,365 eV; 13,415 eV; 13,464 eV) and Gd-L3 edge (7,140 eV; 7,190 eV; 7,220 eV; 7,237 eV). The data was collected at room temperature and ambient pressure using a Si111 monochromator and an Eiger2 X 9M detector for SAXS signal. Sample-detector distance was determined to be 5.9778 m, or 2.8184 m for measurements at Gd-L3 edge, using silver behenate standard.

The azimuthal integration of the obtained 2D scattering patterns was performed by L. Klemeyer with a self-written script in a Python environment based on the PyFAI library.[172]

The resonant scattering contribution was extracted using a python script provided by X. Sun and S. Haas (P62 - DESY). The implemented logic is based on the calculations described in chapter 1.4.2. The so obtained scattering curves are consecutively evaluated using a DREAM model based fitting approach in SasView 5.0.6.[173] In order to assess the goodness of fit of our model against the experimental data, we employed the reduced chi-squared statistic ($Chi^2/Npts$) as a parameter. This statistical parameter is calculated by dividing the chi-squared value (sum of squared deviations between measured and model-predicted values), by the number of degrees of freedom (number of data points minus the number of fitted parameters). A reduced chi-squared value approaching 1 indicates an excellent fit, suggesting that the model accurately represents the data within the constraints of measurement uncertainties.

1.4.5 Results and Discussion

1.4.5.1 Initial particle characterization

Throughout this experiment, four distinct types of nanoparticles were prepared and examined, based on two batches of AuNP cores. The initial batch of AuNPs was successively functionalized through the covalent linkage of proteins bearing a N-terminal cysteine residue (designated as "@Protein"), thiolated PEG bearing a terminal bromine moiety (designated as "@PEG-Br"), or by thiolated PEG with an amino group (designated as "@PEG-NH2"), in that order. The second batch of AuNPs was functionalized by the addition of a molar ratio of 25% PEG-Br and 75% PEG-NH2 (designated as “@PEG-mix”). The two batches of gold nanoparticles, which serve as the inorganic core material, exhibit a narrow size distribution of 12.0 ± 0.9 nm (batch 1) and 12.6 ± 0.7 nm (batch 2), respectively, as determined by transmission electron microscopy evaluation (Fig. 22 A, B, D, E). The successful surface

modification was confirmed by a slight wavelength shift of the localized surface plasmon resonance (LSPR) peak of the AuNPs after the initial citrate ions, which served as capping agents, were replaced by PEG or the protein, respectively (Fig. 22 C, F). Furthermore, laser Doppler anemometry was employed to monitor the alterations in the particles' ζ-potential resulting from the surface modification. The initially citrate-capped AuNPs of batch 1 present a ζ-potential of -18.5 ± 0.6 mV, which changes to -18.9 ± 2.8 mV in the case of the protein coating, +26.3 ± 1.0 mV for PEG-NH2 functionalized AuNPs, or -0.9 ± 0.9 mV for the PEG-Br functionalized NPs. The ζ-potential of the second batch exhibited a notable shift from an initial value of -11.6 ± 2.4 mV (@citrate) to a final value of +8.6 ± 0.6 mV after modification with the mixed PEGs. This change in potential places the particles in a position between those with a fully PEG-NH_2 coating and those with a fully brominated PEG coating, suggesting the presence of a mixed ligand layer.

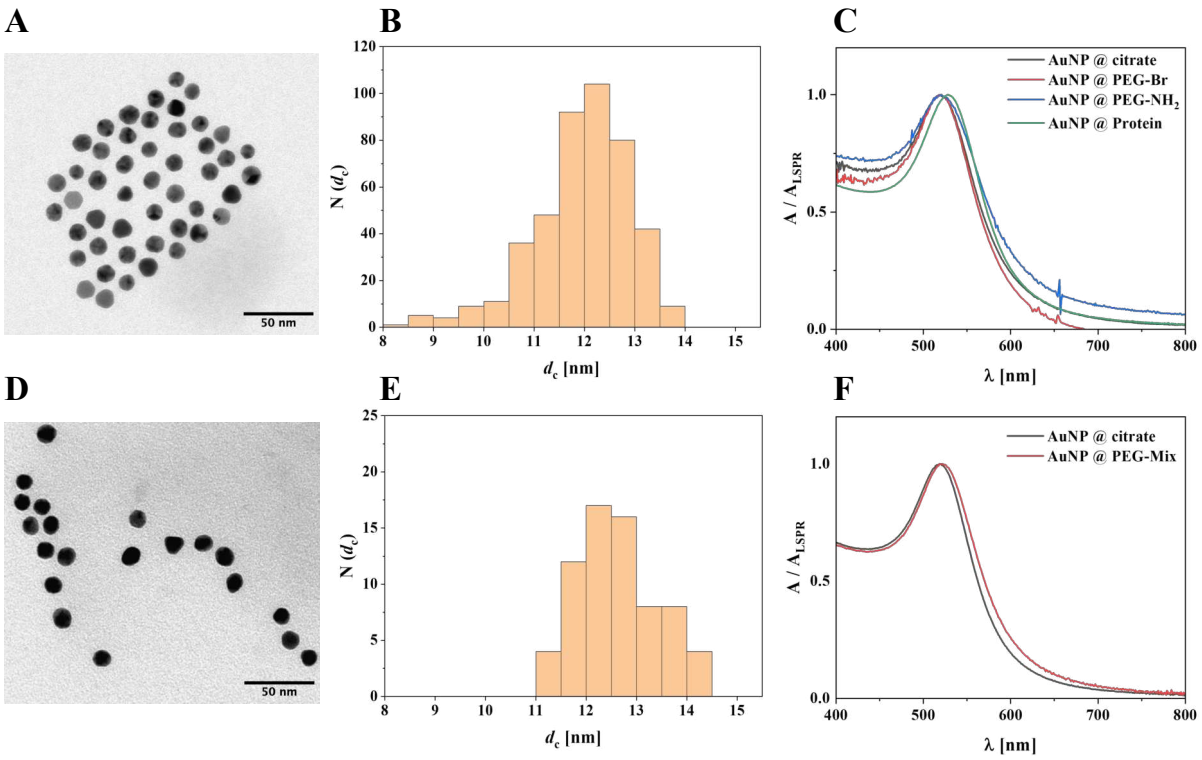

Figure 22: Colloidal characterization of the two NP batches used throughout the study. The upper row depicts batch 1, and the lower row depicts batch 2. A, D) Representative transmission electron microscopy (TEM) image of AuNPs used for the experiments. The scale bar indicates 50 nm. B, E) Histogram of NP core sizes (d_c) based on TEM images. C, F) Normalized UV-visible absorbance spectra of the AuNPs after different surface modifications.

1.4.5.2 AuNPs @ Protein

The size of the nanoparticles was determined through the use of both, dynamic light scattering and fitting of the resonant intensity curve obtained from anomalous small-angle X-ray scattering. The volume-distributed DLS reported a hydrodynamic core size of 12.9 ± 0.2 nm, while aSAXS at the Au-L edge provided a similar size of 12.2 ± 0.4 nm, thereby demonstrating consistent results obtained across both techniques and confirming the expected diameter of the AuNPs in comparison to TEM examinations. In this system, proteins were covalently immobilized directly onto the gold nanoparticles. Subsequent size measurements following immobilization demonstrated an increase of the hydrodynamic diameter to 29.0 ± 1.0 nm via DLS, indicative of the attachment of the protein layer. Similarly, aSAXS at the Gd-L edge agreed this observation with a closely aligned size measurement of 28.1 ± 0.4 nm, indicating that the protein layer had been effectively attached to the AuNP surface. The direct covalent immobilization of proteins onto AuNPs resulted in a distinct increase in nanoparticle size, as consistently observed with both DLS and aSAXS.

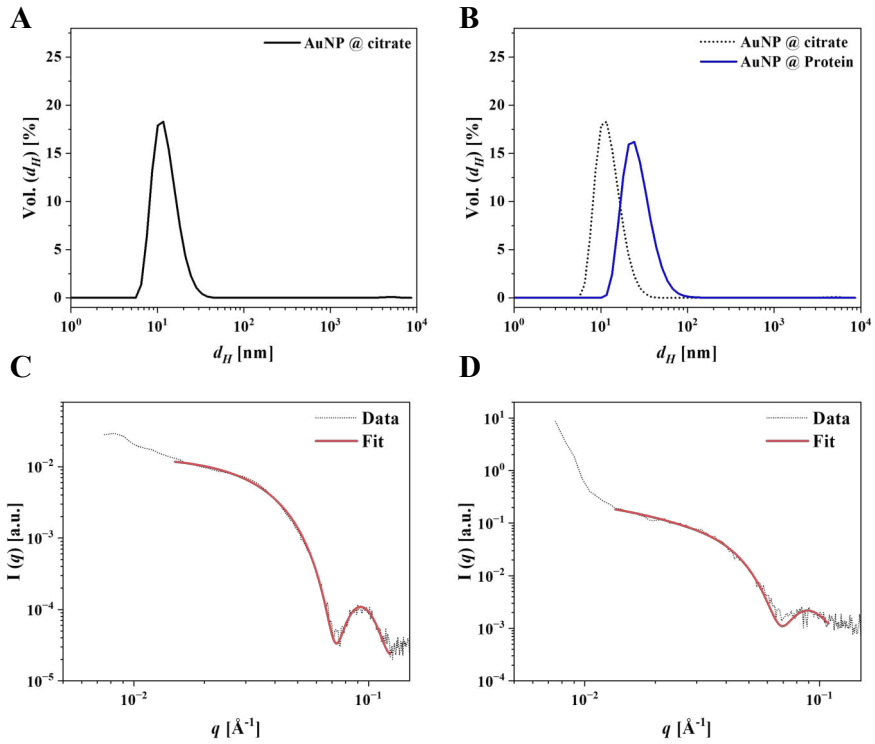

Figure 23: (A) DLS of citrate-capped AuNPs, showing the core size distribution without indications of larger aggregates. (B) DLS of the AuNP@protein system, indicating an increased size; dashed line represents size distribution from (A). (C) Resonant SAXS at the Au-L3 edge with fit supported by a goodness of fit ($Chi^2/Npts$ = 0.25). (D) Resonant SAXS at the Gd-L3 edge with fit supported by a goodness of fit ($Chi^2/Npts$ = 0.67).

1.4.5.3 AuNP @ PEG-NH_2

Verification of the core size of 12.9 ± 0.2 nm (Fig. 25A), as determined by DLS, and 13.0 ± 1.0 nm, as determined by aSAXS (Fig.25D), was consistent with the Au core structure of AuNP@Protein. As the functionalization with amino-terminated PEG did not provide a suitable label for the aSAXS examination, the DLS analysis was conducted as an individual analysis, which revealed that the altered hydrodynamic diameter of the AuNPs@PEG-NH_2 was 26.8 ± 0.3 nm (Fig. 25B). Subsequently, the adsorption of the protein resulted in an observable increase in the system's hydrodynamic size, as observed by DLS, with a value of +3.1 ± 0.9 nm. This alteration is also in accordance with the aSAXS size assessments, which indicate a shell thickness of 4.1 ± 0.3 nm, as determined by the fitting of the resonant scattering at the Gd-L3 edge. This provides evidence of the successful detection of protein adsorption by aSAXS. While the fitting seems slightly negatively affected by the presence of noise in the scattering data, as reflected in higher standard deviations of the obtained values compared to the previous data, it is noteworthy that the reduced chi square of the fit from the scattering data at the Au edge and Gd edge are still 0.29 and 0.39, respectively.

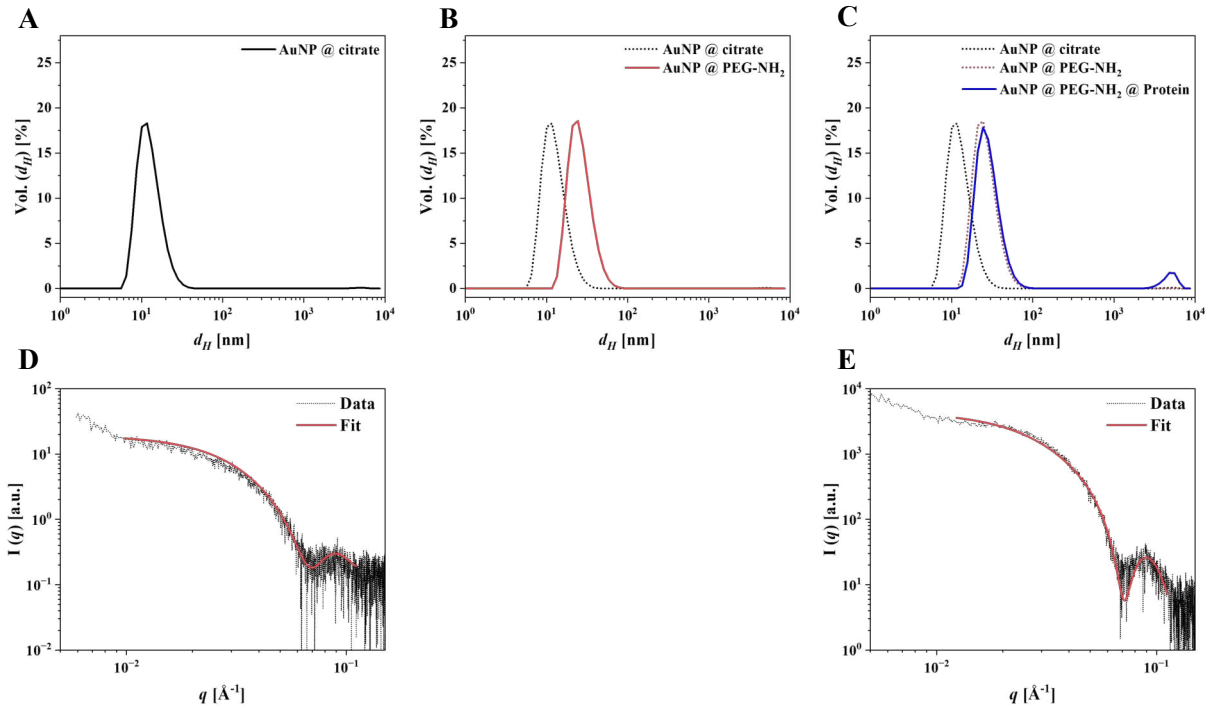

Figure 24: A) DLS of citrate-capped AuNPs, showing the core size distribution. B) DLS of the pegylated AuNPs, indicating an increased size; dashed line represents size distribution from panel (A). C) DLS of the amino-pegylated nanoparticles after introducing to Gd-bearing protein. Dashed lines represent sizes obtained from AuNP alone and after pegylation. D) Resonant SAXS at the Au-L3 edge with fit supported by a goodness of fit ($Chi^2/Npts = 0.29$). E) Resonant SAXS at the Gd-L edge with fit supported by a goodness of fit ($Chi^2/Npts = 0.39$).

1.4.5.4 AuNP @ PEG-Mix

The initial core size of the citrate-capped AuNPs of batch 2 was determined to be 13.1 ± 0.7 nm by DLS and 12.1 ± 0.1 nm by aSAXS, demonstrating the general agreement between the two techniques and consistent to the size of the gold core examined by TEM (12.6 ± 0.7 nm). Following the PEGylation, DLS measurements indicated an increase in size to 28.5 ± 1.0 nm. The nanoparticles were functionalized with a mixture of PEG-NH_2 and PEG-Br. The amino-functionalized PEG facilitated protein corona formation through electrostatic interactions, analogous to those observed in the previously discussed AuNP@PEG-NH_2 system. In addition, the presence of PEG with terminal bromide groups enabled further analysis using aSAXS. This further confirmed, the expanded size to be 28.1 ± 1.5 nm, extracted from the aSAXS at the Br-K edge. Subsequent adsorption of proteins onto the pegylated, covered surface led to additional increases in size, as indicated by DLS (+3.9 ± 0.5 nm) and verified by aSAXS (+3.9 ± 0.3 nm).

This increase conclusively demonstrates the effective formation of a protein corona is traceable by both methods.

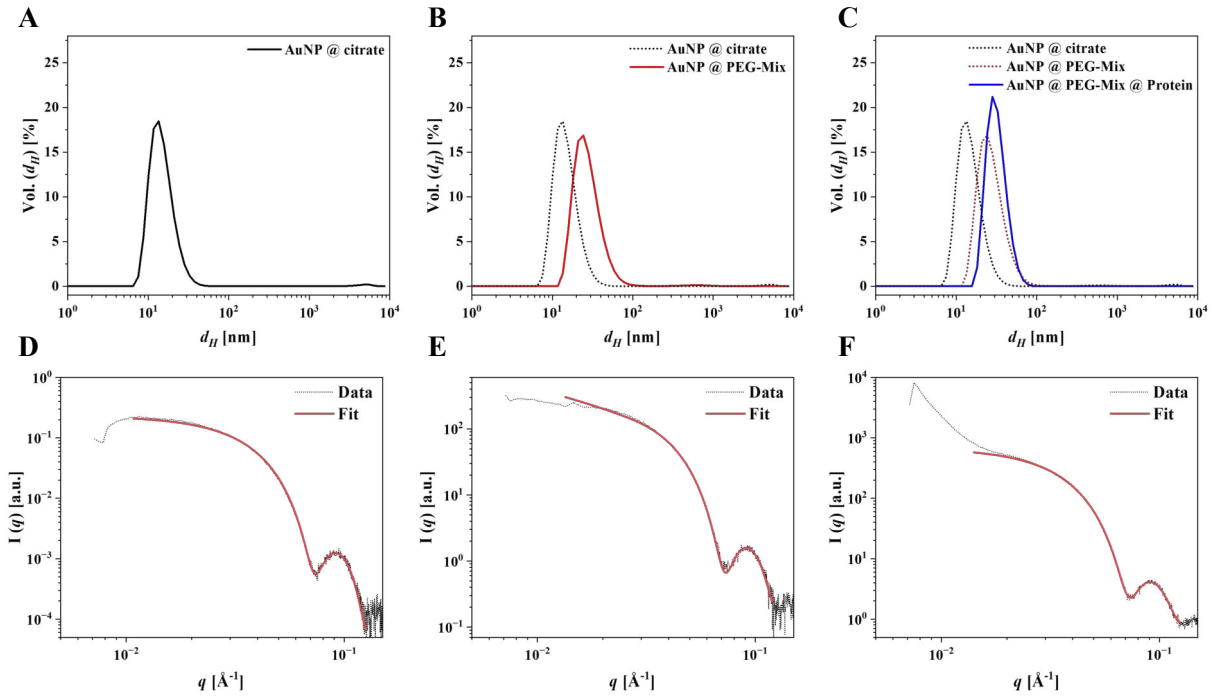

Figure 25: A) DLS of citrate-capped AuNPs, showing the core size distribution. B) DLS of the pegylated AuNPs, indicating an increased size; dashed line represents size distribution from panel (A). C) DLS of the mixed-pegylated nanoparticles after introducing to Gd-bearing protein. Dashed lines represent sizes obtained from AuNP alone and after pegylation. D) Resonant SAXS at the Au-L3 edge with fit supported by a goodness of fit ($Chi^2/Npts = 0.11$). E) Resonant SAXS at the Br-K edge with fit supported by a goodness of fit ($Chi^2/Npts = 0.18$). D) Resonant SAXS at the Gd-L edge with fit supported by a goodness of fit ($Chi^2/Npts = 0.19$).

1.4.5.5 AuNP @ PEG-Br

The initial core size of the citrate-capped AuNPs was determined to be 12.9 ± 0.2 nm by DLS (batch 1) and 12.6 ± 0.1 nm by aSAXS, demonstrating a consistent measurement across both techniques for this particle, which provides an accurate reference for the subsequent modifications. Following to the functionalization with PEG-Br, DLS measurements indicated an increase in hydrodynamic diameter to 21.7 ± 0.6 nm, reflecting the addition of the PEG layer. Similarly, aSAXS supporting this increase in size to 21.4 ± 0.1 nm. Upon the introduction of the protein, the DLS measurements demonstrated no significant increase in size, remaining at 20.5 ± 1.2 nm. Although not statistically significant, indeed, the mean value is observed to decrease slightly. This can be explained by the fact that the hydrodynamic diameter of the

nanoparticle remains constant, whereas the viscosity of the solution slightly increases with the addition of proteins. As this is not considered by the automatic fitting process from the software, a lower value is obtained. However, aSAXS at the Gd-L edge, which is sensitive to the Gd-labeled proteins, revealed a significant shell thickness of 4.0 ± 0.2 nm.

This observation may suggest two possible explanatory scenarios. Initially, one might consider whether the applied aSAXS method itself is not as accurately as expected, and this value possibly reflecting background noise. However, this is unlikely given the high agreement between shell thickness measurements using DLS and aSAXS for the other three nanoparticle systems. Alternatively, the data may indicate the presence of intercalated proteins within the PEG layer, which would not result in an increase in the overall hydrodynamic diameter. The ability of proteins to penetrate and intercalate within the PEG layer is supported by some evidence from previous studies. It has been reported that certain proteins with strong interaction potential, such as those possessing exposed thiol groups, can embed within PEG coatings and bind to nanoparticles.[174] Similarly, it has been indicated that lower PEG densities can result in increased interchain spacing, thereby facilitating protein penetration.[175] Additionally, it was previously shown that proteins may intercalate when the PEG layer is not densely packed, offering a space for proteins mainly driven by hydrophobic interactions.[176] In the two other cases with pegylated nanoparticles discussed above, in which DLS indicated protein adsorption, this phenomenon was predominantly attributable to electrostatic interactions. The amino groups at the end of the PEG chains facilitated the attachment, resulting in the formation of an additional layer of proteins outside the nanoparticle and thus increase the size.

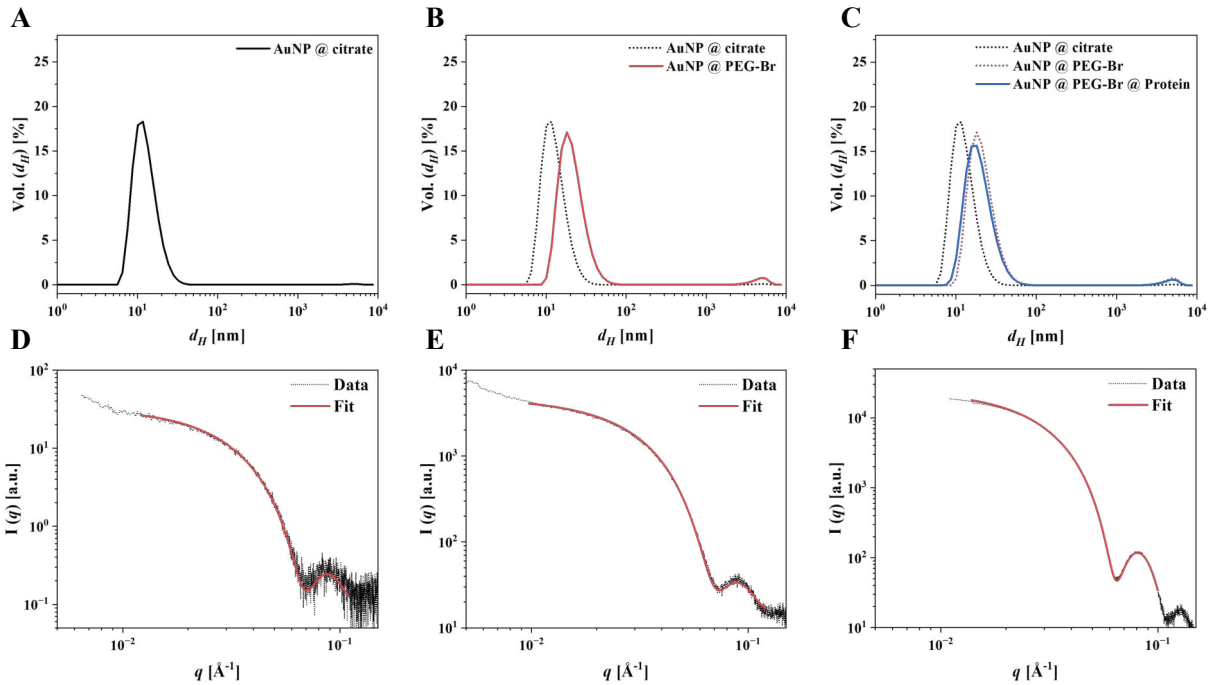

Figure 26: A) DLS of citrate-capped AuNPs, showing the core size distribution. B) DLS of the bromide-pegylated AuNPs, indicating an increased size; dashed line represents size distribution from panel (A). C) DLS of the Br-pegylated nanoparticles after introducing to Gd-bearing protein. Dashed lines represent sizes obtained from AuNP alone and after pegylation. D) Resonant SAXS at the Au-L3 edge with fit supported by a goodness of fit ($Chi^2/Npts = 0.15$). E) Resonant SAXS at the Br-K edge with fit supported by a goodness of fit ($Chi^2/Npts = 0.28$). D) Resonant SAXS at the Gd-L edge with fit supported by a goodness of fit ($Chi^2/Npts = 0.08$).

1.4.6 Conclusion

This study successfully demonstrated the characterization of gold nanoparticles (AuNPs) with different surface chemistries and their corona formation with a Gd-labeled engineered protein, using dynamic light scattering (DLS) and anomalous small-angle X-ray scattering (aSAXS). Across the experiments, the particles exhibited narrow size distributions, confirmed by consistent measurements between both techniques. The studied surface modifications ranged from covalent protein binding to thiolated PEG functionalization, bearing bromine as a label for the aSAXS and/or amino groups enhancing the protein corona formation. These modifications were confirmed by observing changes in the zeta potential and alterations in the localized surface plasmon resonance. The PEGylation and protein corona formation of the NPs led to a significant increase in particle size for most scenarios, which was consistently validated by both DLS and aSAXS measurements, showing good agreement across the analyses. The

study successfully demonstrated the effectiveness of DLS and aSAXS in characterizing the majority of nanoparticle modifications. However, there were some unexpected results, whereby a protein layer was detectable by aSAXS, but not observed by DLS. The hypothesis of protein intercalation within the PEG layer offers a potential explanation, though it requires further exploration. This limitation underscores the need for continued refinement and testing of the provided approach to further understand nanoparticle-protein interactions. Overall, dynamic light scattering is a well-established method for evaluating particle size variations. However, in order to provide detailed, step-by-step insights into particle changes, it is necessary to measure at each modification stage of the hybrid construct. In contrast, anomalous small-angle X-ray scattering offers a distinctive advantage, enabling comprehensive assessments of the entire nanoparticle assembly, including the AuNP core, PEG layer, and adsorbed proteins, through a single set of measurements. By employing energies near absorption edges of different elements, aSAXS effectively differentiates between individual “layers” of the hybrid particle. This experiment presents a highly promising methodology for comprehensive nanoparticle analysis and characterization.

In conclusion, this experiment demonstrates the complementary nature of DLS and aSAXS as analytical techniques for the detailed examination of nanoparticle surface modifications and protein interactions.

2 Biodegradable polyelectrolyte capsules: synthesis and intracellular imaging of delivered Se compounds

Polyelectrolyte multilayer capsules (PEC) are expected to be a promising advancement in the field of drug delivery. Their hollow structure allows the loading of a variety of different cargos, ranging from small molecules, oligonucleotides, proteins or inorganic nanoparticles.[177–180] The concept of these capsules was initially developed nearly four decades ago, emerging from the convergence of two pioneering ideas: the entrapment of drugs into polymeric materials and the layer by layer (LbL) assembly of ultrathin films using electrostatic interactions of oppositely charged polyelectrolytes.[181,182] This fusion has led to the development of hollow, biocompatible capsules as plausible drug delivery carriers.[183]

The synthesis of PEC involves two essential elements: the core template and the polyelectrolyte shell. The core can be constructed from a range of inorganic materials, *e.g*., silicon dioxide, cadmium carbonate or calcium carbonate.[184,185] The selection of the template materials is dependent on different factors, for instance residual cadmium ions negatively impact the biocompatibility. Whereas silicon dioxide is available from nano- to micrometer sized particles, it requires the use of highly toxic hydrofluoric acid, which limits their broad usage. Therefore, calcium carbonate has become widely accepted due to its easy manipulation in regard of size and shape, and biocompatibility.[186] The size of the calcium carbonate cores can be finely controlled by adjusting parameters such as reaction time, temperature or precursor concentration.[187–189] Biodegradable polyelectrolytes like dextran (DEX) and poly-L-arginine (PARG) are shown to be suitable building blocks for the capsule preparation onto the inorganic template.[190] The LbL assembly process is based on the adsorption of these oppositely charged polyelectrolytes onto the core template, driven by electrostatic attraction, to form a multi-layered capsule. During this adsorption process the adjustment of pH and salt ion concentration drastically affects the layer thickness and consequently its permeability.[191,192]

A significant advantage of polyelectrolyte capsules is their potential to enhance the bioavailability of hydrophobic or otherwise poorly aqueous soluble compounds, which is particularly relevant in the delivery of therapeutic selenium (Se) compounds. Selenium has emerged as a compelling element in cancer research for decades, offering promising avenues for therapeutic interventions. As an essential trace element with diverse biological functions, Se plays a pivotal role in cellular processes and redox regulation, whereby inorganic selenium salts show high toxicity. In contrast, organic selenium compounds, typically in the form of

seleno-amino acids, can be taken up by humans as a trace element from food and provide a Se source for protein synthesis. The first experimental animal study revealed that organic selenium compounds as supplements in drinking water effectively reduced cancer incidence and the number of tumors per animal.[193,194] Based on these results, subsequent studies in this field have focused on developing effective anticancer selenium compounds with higher biocompatibility as compared to pure selenomethionine**.**[195–197] Natural occurring selenium compounds such as seleno-amino acids, can be safely ingested through diet and have demonstrated effectiveness in reducing cancer incidence in animal studies. Whereas the synthetic selenium compound 1,4-phenylenebis(methylene)selenocyanate (p-XSC) stands out due its significant tumor inhibition properties across various cancer models. In animal models, p-XSC showed significant tumor inhibition effects on various types of cancer. While the functional mechanism has not yet been conclusively clarified, it is suggested that redox activity of p-XSC contributes to reactive oxygen species (ROS) induced DNA damage.[198–200] The clinical application of p-XSC is hindered by its hydrophobic nature and strong irreversible binding to albumin in the bloodstream, which limits its promising effect.[201] Herein polyelectrolyte capsules offer a viable solution by encapsulating p-XSC, thereby improving its bioavailability and enhancement of its therapeutic outcome by protecting it from albumin proteins.

However, it is important to note that the uptake mechanism and the subsequent intracellular distribution may differ between individual small molecules and the rather large micrometer-sized capsules. Therefore, it's crucial to understand the internalization and intracellular fate of the capsule and the entrapped cargo. The internalization of PEC by cells has been demonstrated the be generally non-specific across different cell types.[202] Recent data suggest a detailed mechanism for the capsules' uptake involving multiple stages and pathways.[203] Initially, electrostatic interactions induce a nonspecific binding of the PEC to the cell surface. This is followed by extensive actin reorganization that creates a phagocytic cup to stabilize the capsule at the outer cell plasma membrane. During this early engulfment phase, the capsules showed a co-localization with lipid rafts and an acidic environment, suggesting a lipid raft-mediated micropinocytosis as the primary mechanism. Consequently, phagocytotic pathways are recruited for the further intracellular trafficking.[203–205]

A critical aspect when employing PEC for drug delivery is to ensure the final efficient endosomal escape of the encapsulated compound. After the cellular uptake described above, the capsules are typically sequestered within cellular vesicles such as endo-/lysosomes. Though,

for the therapeutic effect, the encapsulated compound must escape into the cytosol. This process can be challenging, because endosomal membranes often act as a barrier.
Traditional methods for monitoring this endosomal escape involve labeling techniques such as fluorescent dyes or specifically pH-sensitive dyes.[206] While these methods have been shown to be effective, they may alter the physicochemical properties of the encapsulated compound, potentially also the intracellular distribution. To circumvent these issues, single cell X-ray fluorescence imaging provides a label-free alternative for visualizing the intracellular distribution of selenium-based compounds. In the following chapters, the synthesis and comprehensive characterization of the biodegradable polyelectrolyte capsules are presented, along with studies on their cell compatibility and uptake. Finally, the intracellular Se distribution after delivery via ~5 µm sized PEC is investigated by X-ray fluorescence imaging. Using this technique, we aim to better understand the degradation behavior and potential endosomal escape.

Most of the presented results of the following section are submitted and currently under review:

Skiba, M.; Reszegi, R. R.; Huang, Y.; Roy, S.; Han, J.; Brückner, D.; Sanchez-Cano, C.; Zhao, Y.; Hassan, M.; Feliu, N.; Falkenberg, G.; Parak, W.J.:
Exploring the intracellular distribution of Se compounds delivered by biodegradable polyelectrolyte capsules using X-ray fluorescence imaging.

Contribution:
The author contributed by synthesis and characterization of the particles, performing synchrotron experiments, formal analysis of the acquired data and by writing the manuscript.

2.1 Materials

Calcium chloride dihydrate (Sigma), sodium carbonate (Sigma), poly-L-arginine hydrochloride (PARG, Mw: 15 – 70 kDa), dextrane sulfate sodium salt (DEX, M_w = 40 kDa, Sigma), sodium poly-styrene sulfonate (PSS, Mw = 70 kDa), Poly(allylaminhydrochlorid) (PAH, Mw = 15 kDa, Merck), sodium ethylenediaminetetraacetic acid disodium salt (EDTA, Carl Roth), dimethyl sulfoxide (DMSO, Carl Roth), Acetonitrile (HPLC grade, Waters), Water (HPLC grade, Waters), 1,4-Phenylenebis(methylene)selenocyanate (p-XSC, Abcam), Si_3N_4 membranes

(Silson Ltd.), phosphate buffered saline (Sigma), Dulbecco's modified eagle's medium (DMEM, Carl Roth), 0.05% trypsin/EDTA (Gibco), penicillin streptomiycin (Gibco), poly-L-lysine (Sigma), ammonium acetate (Sigma), acetic acid (Sigma).

2.2 Methods

2.2.1 Synthesis and characterization of polyelectrolyte capsules

A well-established layer-by-layer assembly protocol was followed with some minor changes.[207] Both types of polyelectrolyte capsules (PEC) were synthesized using a layer-by-layer assembly technique according to previously described protocols. Briefly, 1 mL aqueous Na_2CO_3 (0.33 M) was mixed under rapid stirring (1000 rpm) with 1 mL aqueous $CaCl_2$ (0.33 M) solution. The mixture was stirred for 30 s, followed by 2 min standing without agitation. The suspension was washed 3 times by centrifugation (1500 rcf, 20 s) and the supernatant was replaced with miliQ water to remove unreacted salts. Layer-by-layer assembly was conducted on freshly prepared $CaCO_3$ microspheres by repetitive suspending of the particles in 1 mL polyelectrolyte solution of opposite charge (2 mg/mL, 0.05 M NaCl, pH 6.5), sonication for 2 min and agitated for 12 min. After each step unreacted polyelectrolytes were removed by two times centrifugation (1500 rcf, 20 s) and replacing the supernatant with miliQ water. Biodegradable capsules consist of 4 bilayers poly-L-arginine (PARG) and dextrane sufate (DEX). For non-biodegradable capsules alternating assembly of polyallylamine hydrochloride (PAH) and polystyrene sulfonate (PSS) was conducted. After the last layer was assembled, the washed particles were suspended in 1 mL sodium ethylenediaminetetraacetic acid (EDTA, 0.2 M, pH 6.4) for 16 h at 4°C, followed by three washing steps with miliQ water (280 rcf, 4 min). Finally, the polyelectrolyte capsules were suspended in 200 µL miliQ water and stored at 4°C for further use.

2.2.2 Loading of the polyelectrolyte capsules with p-XSC

For loading of the PEC with the hydrophobic low molecular weight compound p-XSC, a post-loading strategy, followed by heat shrinkage of the capsules was used.[208] The stock of the polyelectrolyte capsules was washed thrice with dimethyl sulfoxide (DMSO) (280 rcf, 4 min), followed by incubation in 1 mL p-XSC (3 mg/mL in DMSO) for 60 minutes. Next, the solution containing the capsules was heated to 60°C for 90 min to induce shrinkage and thereby

entrapment of the hydrophobic drug. Thermal stability of the encapsulated drug was confirmed by ESI-MS (Figure 28). Afterwards, the capsules were washed four times by centrifugation (280 rcf, 4 min), *i.e.* replacing the supernatant above the pelleted capsules with miliQ water, in order to remove free drug. The capsules were immersed in 200 µL miliQ water and used immediately for characterization and treatment. Control capsules were handled similar, but pure DMSO was used for incubation.

2.2.3 PEC morphology as evaluated by scanning electron microscopy

To probe the morphology of the synthesized polyelectrolyte capsules, the PEC stock solution was diluted 100-fold with miliQ water and 5 µL were deposited onto Si-waver and let dry in air. Consecutively scanning electron microscopy (SEM, Zeiss Sigma Gemini) was performed.

2.2.4 Size evaluation by phase contrast microscopy

The distribution of PEC diameters was determined by optical phase contrast microscopy. Polyelectrolyte capsules were diluted 50-fold with phosphate buffered saline (PBS, pH 7.4) and 10 µL were transferred to a cover slide. 100 capsules were manually analyzed using FiJi software V. 2.14.[109]

2.2.5 Concentration determination

To determine the capsule concentration $N_{capsule}/V_{medium}$ the PEC stock solutions were diluted 25-, 50-, and 100-fold with PBS and the PEC were manually counted using an improved Neubauer hemacytometer under an optical light microscope. The resulting three values were averaged. The concentration of the solutions of empty biodegradable capsules, p-XSC filled biodegradable capsules, and p-XSC filled non-biodegradable capsules was determined to be $N_{capsule}/V_{medium}$ = $1.40 \cdot 10^6$/mL, $5.13 \cdot 10^6$/mL, and $2.13 \cdot 10^6$/mL respectively.

2.2.6 Quantification of p-XSC *per* capsule

For the chemical digestion of polyelectrolyte capsules, 5 µL PEC stock solution was mixed with 95 µL of freshly prepared aqua regia, followed by the addition of 1900 µL HCl (2 vol.%). The amount of elemental selenium in this solution was determined by inductively coupled plasma – mass spectrometry (ICP-MS, Agilent, 7700 series). A calibration curve with the isotope ^{78}Se

was performed before each measurement using 9 concentration points (0 – 2500 ppb) by diluting a single element ICP standard (Carl Roth). The obtained counts per second were plotted against the known Se concentration and the following linear regression offers a linear regression coefficient $R \geq 0.9999$ for all conducted experiments. Finally, the p-XSC concentration was calculated by considering the dilution steps and the molecular composition of two Se atoms per p-XSC molecule. The density of water was approximated to be 1 g/mL, thus 1 ppb = 1 µg/L. Knowing the molar mass of Se M_{Se} = 78.971 g/mol and of p-XSC $M_{p\text{-}XSC}$ = 314.104 g/mol (each p-XSC molecule contains 2 Se atoms), the amount of p-XSC loaded in each capsule was calculated as $m_{p\text{-}XSC/capsule} = m_{Se/capsule} \cdot (M_{p\text{-}XSC}/2M_{Se})$.

To estimate the wt.% of the drug in respect to the PEC the following assumptions were made. As not all the polyelectrolytes offer a tabulated density, the density of the crystalline material of PSS (value from Sigma Aldrich) and PAH (value from Biosynth ®) was averaged, as we conclude a similar composition of both compounds in the capsule wall, which not differs to much from PARG and DEX. The thickness of the capsules was determined from scanning electron microscopy evaluations of broken capsules, offering a top view on the capsule wall. Assuming the capsule as a hollow sphere, with an outer diameter of 5 µm and the experimentally determined wall thicknesses, the volume of the wall can be assessed. Considering the average density of polyelectrolytes, the average weight of one capsule can be calculated. Knowing the amount of p-XSC per capsule, the wt.% can be assessed.

2.2.7 Determination of capsule leakage

To evaluate the stability of the capsules and leakage of the compound in cell medium, a membrane dialysis experiment was performed. For this purpose, 2 mL of serum supplemented Dulbecco's modified eagles' medium (DMEM) containing either freshly loaded non-biodegradable PEC@p-XSC, biodegradable PEC@p-XSC or free p-XSC were placed in a Spectra/Por ® Float-A-Lyzer™ dialysis membrane. The dialysis membrane has a molecular weight cut-off of 300 kDa, allowing p-XSC sequestered by albumin to pass through. The dialysis membrane was placed in a glass vial containing 10 mL of DMEM and incubated at 37°C, mimicking the conditions for cell incubation prior to X-ray fluorescence imaging experiments. The Se concentration of the solutions inside the dialysis membrane was determined at the start of the experiment (t = 0 h) and after 24h (t = 24 h). The ratio between Se concentration at t = 0 h and t = 24 h was used to evaluate the leakage of p-XSC from the capsules.

2.2.8 Electrospray ionization – mass spectrometry (ESI-MS)

To prove the thermal stability of p-XSC, 1 mg p-XSC was dissolved in 10 mL using a mix of DMSO/acetonitrile/water (2/49/49, v/v/v). At a flow rate of 10 µL/min, the sample was injected *via* direct infusion into an ESI-Q-TOF mass spectrometer (Synapt XS, Waters). All experiments were conducted in positive ion mode between m/z = 100 and 1000, capillary voltage 1 kV, sampling cone 35 V, source offset 4 V, source temperature 80°C, desolvation temperature 250°C, desolvation gas flow 500 L/h, nebulizer pressure 6.5 bar. m/z refers to the mass m of the ion X^{z-} as normalized to the unified atomic mass unit, divided by the charge state z of the ion. For the internal reference signal a lock mass of leucine-enkephalin (m/z = 556.2771) was sampled at the beginning at the end of each measurement. The sample was infused for 60 s and an ESI-MS spectrum was acquired. Then, the sample was incubated for 90 min at 60°C in a water bath, similar to the heat-shrinking procedure used for the polyelectrolyte capsules. Afterwards the sample was infused again and the spectrum was recorded for 60 s.

2.2.9 Cell culture

Human cervical carcinoma (HeLa) cells were cultured in Dulbecco's modified eagles' medium (DMEM), containing 100 U/mL penicillin-streptomycin and 10 vol.% fetal bovine serum. Cells were stored in a humidity-controlled incubator at 37°C at 5% CO_2. Subculturing was conducted every 2-3 days when confluency of ~80% was reached by chemical detachment using 0.05% Trypsin/EDTA.

2.2.10 Cell viability assay

Cell viability upon exposure of HeLa cells to all used compounds was evaluated by a resazurin based fluorescence assay.[209] Therefore V_{medium} = 100 µL of a N_{cell}/V_{medium} = 75,000 cells *per* mL stock were seeded *per* 96-well plate (seeding area A_{well} = 32 mm^2). The following day particles/drugs were diluted in serum supplemented Dulbecco's modified eagle's medium to different concentrations. Cells were incubated at 37°C with 100 µL DMEM containing the different compounds for 24, 48 h respectively. As a control at least 8 wells with cells were incubated with pure DMEM. After the different exposure times, each well was washed twice with 100 µL PBS, followed by the addition of 100 µL resazurin in DMEM (0.25 mg/mL). After

4 h at 37°C the fluorescence of resofurin was measured using 560 nm excitation and the emission at 570-610 nm was collected with a fluorimeter (Fluorolog, Horiba Jobin Yvon, Germany). The emission from pure resazurin was subtracted as background, and the emission intensity of the control group was set as V = 100% cell viability. The viability of the cells exposed to PEC and/or p-XSC was calculated by normalizing the emission intensities to that of the control.[209] Each concentration was tested in triplicate on a single 96-well plate.

2.2.11 EC_{50} calculation

For a better comparison of the cytotoxic effect originating from the different compounds, EC_{50} values were determined and depicted in Tab 1. The calculation was conducted in a python-based environment using a four-parameter-logistic function, according to Keshtkar *et.al.*[210]. The implemented code is shown below, allowing reproducibility and plausibility of the values. Function was defined by the parameters: *a* – minimum value, *b* – Hill's slope, *c* – point of inflection, *d* – maximum value. Experimentally obtained cell viability values < 0 where constrained to 0. Although experimentally slightly negative viabilities can occur, these make biologically no sense and influence the reasonableness of the fit.[211] The applied curve_fit as part of SciPy.Optimize package, is based on Levenberg-Marquardt algorithm. This algorithm terminates when further iterations do not result in significant improvements, as defined by the convergence criteria (no improvement based on least square difference between iterations). The EC_{50} value is directly derived from the fitting parameter *c,* as the transition between lower and upper asymptote occurs at this point. Standard deviation is calculated from the variances of *c,* provided by 'curve_fit'. As square root of this variances it represents the uncertainty of the fit and consequently be interpreted as standard deviation of *c*. The goodness of fit parameter R^2, is calculated by comparing the sum of squared deviations of the predictions from the actual experimentally assessed values, in order to determine the goodness of fit.

```
import matplotlib.pyplot as plt
import numpy as np
from scipy.optimize import curve_fit

# definition of four-parameter-logistic-function
def four_param_logistic(x, a, b, c, d):
    return d + (a - d) / (1 + (x / c) ** b)
```

```
# Data
data = np.array([
    [32, -2.97386, 1.12551, -3.59928, 5.17024],
    [16, -2.71011, 1.35499, -4.10238, 5.41483],
    [3.2, -1.4765, 2.29382, 0.00685, 4.84111],
    [1.6, 12.85349, 5.76061, 6.80237, 4.62776],
    [0.32, 90.52799, 6.27434, 103.19324, 5.01008],
    [0.16, 95.57389, 9.18005, 101.7648, 9.83577],
    [0.032, 100.88719, 15.15911, 105.92598, 14.95578],
    [0.016, 97.55777, 15.23421, 105.08143, 6.13845],
    [0.0032, 96.37806, 7.77825, 101.38459, 1.04225],
    [0.0016, 99.39373, 9.00109, 103.61122, 5.88875],
    [3.2E-4, 95.22972, 11.22584, 103.85616, 17.35133]
])

# get values from data
concentration = data[:, 0]  # concentration in µg/mL
viabilityvalues_1 = data[:, 1]  # Viability 24h
stdev_1 = data[:, 2]  # StDev Viability 24h
viabilityvalues_2 = data[:, 3]  # Viability 48h
stdev_2 = data[:, 4]  # StDev Viability 48h


# Viability <0 = 0
viabilityvalues_1[viabilityvalues_1 < 0] = 0
viabilityvalues_2[viabilityvalues_2 < 0] = 0

# fitting of four-parameter-log-function
initial_guess = [100, 1, 1, 0]  # a, b, c, d
bounds_1 = ([0, 0, 1e-10, 0], [np.inf, np.inf, np.inf, 100])
popt_1, pcov_1 = curve_fit(four_param_logistic, concentrations, viabilityvalues_1,
                           p0=initial_guess, bounds=bounds_1, maxfev=10000)

bounds_2 = ([0, 0, 1e-10, 0], [np.inf, np.inf, np.inf, 100])
popt_2, pcov_2 = curve_fit(four_param_logistic, concentrations, viabilityvalues_2,
                           p0=initial_guess, bounds=bounds_2, maxfev=10000)

# Calculate R_squared (COD) for both fits
def calculate_r_squared(y_true, y_pred):
    ss_res = np.sum((y_true - y_pred) ** 2) #sum of squares residuals
```

```
    ss_tot = np.sum((y_true - np.mean(y_true)) ** 2) #total sum of squares
    r_squared = 1 - (ss_res / ss_tot)
    return r_squared

y_pred_1 = four_param_logistic(concentration, *popt_1)
y_pred_2 = four_param_logistic(concentration, *popt_2)

r_squared_1 = calculate_r_squared(viabilityvalues_1, y_pred_1)
r_squared_2 = calculate_r_squared(viabilityvalues_2, y_pred_2)
```

Code Snippet 1: Implemented four-parameter-logistic function to calculate EC_{50}-values (*c*) and subsequent determination of the goodness of fit parameter R^2 with exemplary data.

2.2.12 Cell uptake experiments

Validation and quantification of p-XSC uptake by cells was done by inductively coupled plasma mass spectrometry. Therefore V_{medium} = 2 mL of a cell stock solution ($N_{cell}/V_{medium} = 10^5$ mL^{-1}) was seeded in a 6-well plate (surface area per well A_{well} = 960 mm^2). The following day, after removing the cell medium, V_{medium} = 2 mL of DMEM containing the PEC/p-XSC in different concentrations was added to each well. After 24, 48 h respectively, each well was washed thrice with 2 mL phosphate buffered saline (PBS) to remove non-internalized compounds. Then cells were chemically detached by addition of 100 µL of 0.05% Trypsin/ethylenediaminetetraacetic acid (EDTA), and addition of 1.9 mL DMEM after 2 min. Cells were manually counted (N_{cell}) using a Neubauer improved haemocytometer. Note, in all other context N_{cell} refers to the number of seeded cells. However, here N_{cell} refers to the cells counted before Se quantification with ICP-MS, and thus take into account rise in cell number due to proliferation.[212] Subsequently cells were pelleted by centrifugation (300 rcf, 5 min) and digested with 50 µL of HNO_3 (aq, 67 wt.%) overnight. The following day 100 µL HCl (aq, 37 wt%) was added before diluting the sample with 1950 µL of 2% v/v HCl. The amount of p-XSC per cell was obtained by measuring whole Se content in samples by ICP-MS and considering individual cell numbers and dilution steps.

2.2.13 Sample preparation for X-ray fluorescence imaging

For synchrotron X-ray fluorescence imaging first, $N_{cell} = 2 \times 10^5$ HeLa cells in DMEM (V_{medium} = 2 mL) were seeded in 6-well plates and incubated for 16 h at 37°C, 5% CO_2. Next, the medium was exchanged and replaced with DMEM containing $C_{p\text{-}XSC}$ = 1 µg/mL p-XSC, either in biodegradable capsules, non-biodegradable capsules, or as free drug. One well of cells was treated with 6×10^5 empty biodegradable capsules, which mimics around the same number of capsules, as compared to p-XSC filled capsules. After 24 h of incubation, the medium was removed, and cells were washed thrice with PBS before chemical detachment using 100 µL 0.05% Trypsin/EDTA. Cells were diluted to reach 5×10^4 cells/mL. One drop (10 µL) of each solution was placed on pre-arranged silicon nitride membranes (Silson Ltd, 500 nm thick) and incubated for 2 h before adding carefully 2 mL of DMEM to each membrane. Following 24 h of incubation medium was removed and cells were washed three times with ammonium acetate buffer (pH 7.2) and thrice in miliQ water. Membranes were blotted carefully with filter paper to remove residual liquids before plunge freezing in liquid ethane.[108] Finally, samples were freeze dried (Christ) while ramping temperature and pressure from -80°C, 0.01 mbar in 72 h to 25°C, 1 bar, respectively.

2.2.14 X-ray fluorescence imaging

Two-dimensional X-ray fluorescence imaging was conducted at the DESY-PETRA III P06 microprobe beamline.[133] The energy of incident beam was fixed to 17 keV for all measurements. For coarse scans, the beam size was determined to be 2.7 µm × 1.5 µm (h × v) with 100 ms dwell time on each spot. For fine cellular scans the beam was focused to a beam size of 420 nm × 260 nm (h × v), 100 ms dwell time. All measurements were conducted under standard atmospheric conditions, without the implementation of vacuum or cooling. A Vortex ME4 detector was positioned approximately 3 cm at an angle of 135° from the sample. Quantitative evaluation was performed by measuring a multi element standard (RF17-14-18C10) on a Si_3N_4 membrane (AXO DRESDEN GmbH) under the same condition as the samples. The standard contained the elements Fe, Cu, Mo, Pd, La, and Pb, covering a large energy range of XRF emission lines. For these elements a direct measurement of the calibration factors converting from counts to areal density was possible. The calibration factors of all other elements of interest were calculated from the measured calibration factors by using element-

specific parameters provided by the xraylib library.[213] For the elements of interest no absorption correction was necessary.

2.3 Results & Discussion

2.3.1 Synthesis and Characterization of the polyelectrolyte capsules

Three different types of PEC were synthesized. Biodegradable PEC consist of 4 bilayers PARG/DEX, whereas non-biodegradable PEC, as control, were synthesized using poly allylamine hydrochloride (PAH) and poly styrene sulfonate (PSS). As negative control, empty PEC were prepared, *i.e*. biodegradable PEC without p-XSC loading. All capsules investigated were reasonably uniform in spherical shape and size, as confirmed by scanning electron microscopy (SEM). To perform SEM, the PEC samples had to be dried and the reduced pressure used during the imaging led to a crushed structure (Figure 27 first row). Phase contrast light microscopy (PCM) was therefore used as alternative imaging technique. The average diameters (d) of the PEC were determined from the PCM images, by measuring 100 capsules in each group (Figure 27 second row). Empty biodegradable capsules ($(PARG/DEX)_4$) show a diameter of $d = 4.9 \pm 0.5$ µm, p-XSC filled biodegradable capsules (p-XSC @$(PARG/DEX)_4$) $d = 5.4 \pm 0.7$ µm, and the diameter of non-biodegradable capsules loaded with p-XSC (p-XSC @ $(PAH/PSS)_4$) was determined to be $d = 5.3 \pm 0.9$ µm (Figure 27 third row). The concentration of the solutions of empty biodegradable capsules, p-XSC filled biodegradable capsules, and p-XSC filled non-biodegradable capsules was determined to be $N_{capsule}/V_{medium} = 1.40 \cdot 10^6$/mL, $5.13 \cdot 10^6$/mL, and $2.13 \cdot 10^6$/mL respectively.

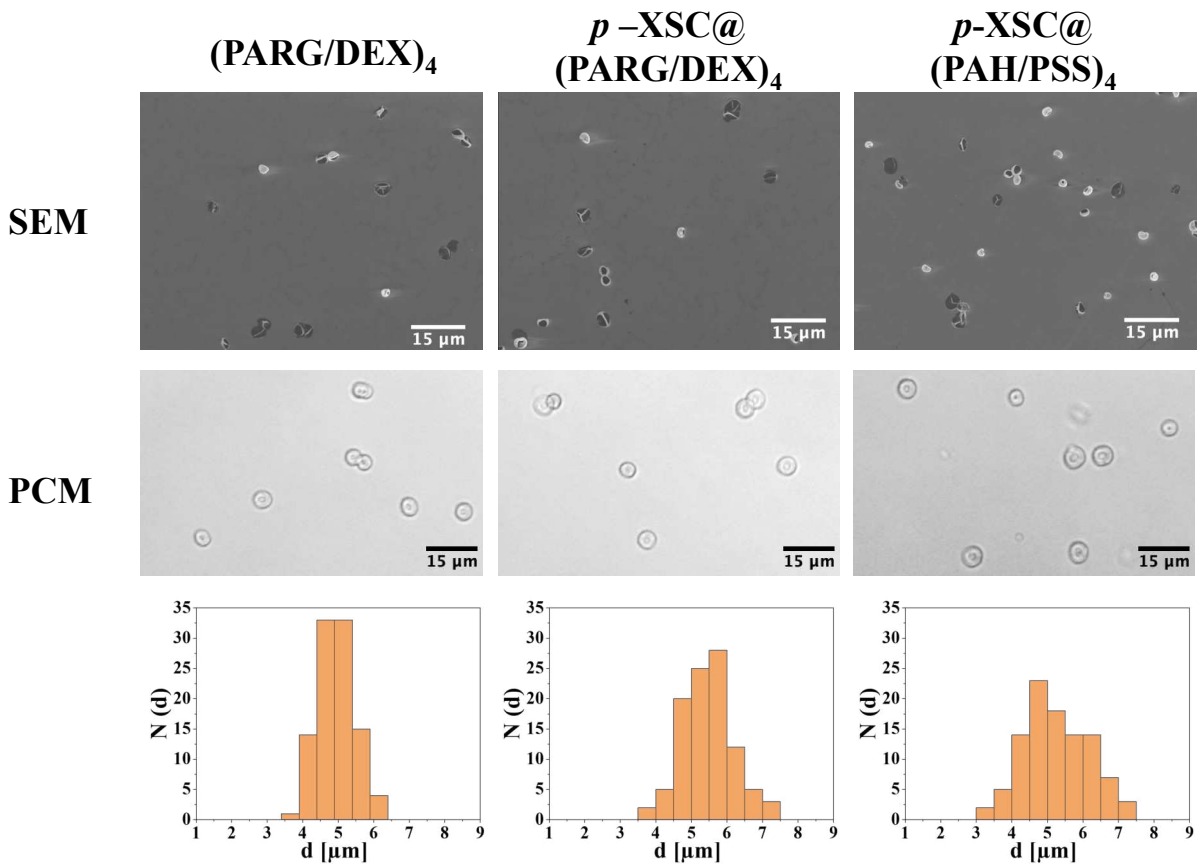

Figure 27: Characterization of the polyelectrolyte capsules used in this study. First row: scanning electron microscopy (SEM) images of empty biodegradable polyelectrolyte capsules, p-XSC filled biodegradable polyelectrolyte capsules and p-XSC filled non-biodegradable polyelectrolyte capsules. Scale bar = 15 µm. Second row: optical phase contrast microscopy (PCM) of the different PEC. Scale bar = 15 µm. Third row: Histogram N(d) showing the number of capsules found with a diameter d within 100 analyzed PEC.

The amount of elemental Se encapsulated per PEC $m_{Se/capsule}$ was determined by inductively coupled plasma – mass spectrometry (ICP-MS) measurements. In average each capsule of $(PARG/DEX)_4$ and $(PAH/PSS)_4$ PEC contained $m_{p\text{-}XSC/capsule} = 0.87 \pm 0.06$ pg and 0.81 ± 0.19 pg p-XSC, respectively. The estimate of the mass fraction of the loaded p-XSC is based on a calculation, assuming the capsule as a hollow sphere with a wall thickness determined by scanning electron microscopy images. The capsules wall thickness was determined to be 0.31 ± 0.06 µm for $(PARG/DEX)_4$ PEC, and 0.30 ± 0.05 µm for $(PAH/PSS)_4$ PEC. Thus, the average weight of one capsule was calculated to be 19.72 ± 2.09 pg for biodegradable and 18.99 ± 1.72 pg for the non-biodegradable capsules. The amount of p-XSC represents 4.2 ± 0.5 wt.% of the overall composition in case of biodegradable PEC, and

4.1 ± 1.0 wt.% for non-biodegradable capsules. The dialysis experiment to determine possible leakage of the capsules revealed that after 24 h, 96.1% ± 4.0% of the initial Se was found for nonbiodegradable $(PAH/PSS)_4$@p-XSC PEC, 95.2% ± 3.6% for biodegradable $(PARG/DEX)_4$@p-XSC PEC and 9.0% ± 7.1% for p-XSC, in the solution inside the dialysis membrane. The higher standard deviation observed in the case of p-XSC can be attributed to the Se approaching the detection limit of the used ICP-MS after 24 hours.

To exam the thermal stability of the p-XSC compound, direct infusion electrospray ionization mass spectrometry was performed before and after heating the compound for 90 minutes to 60°C, whereas no indications of smaller fragments nor a significant drop in intensity was indicated (Figure 28 A, B).

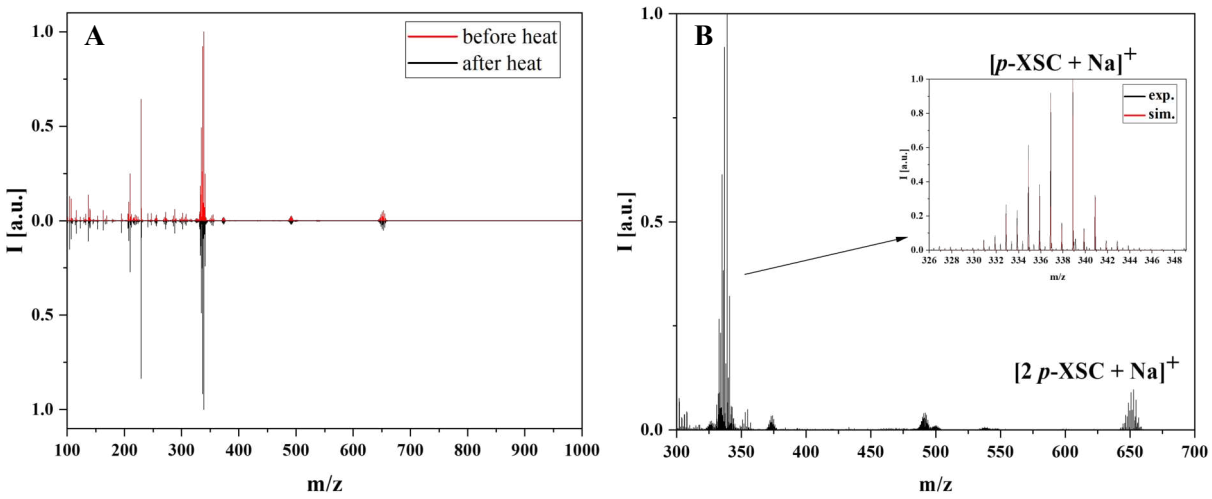

Figure 28: A) Direct infusion ESI-MS spectra of *p*-XSC before (red) and after (black) incubation for 90 min at 60°C, showing the normalized intensity I over the mass/charge ration m/z. m/z refers to the mass m of the ion X^{z-} as normalized to the unified atomic mass unit, divided by the charge state z of the ion. B) Direct infusion ESI-MS spectra of *p*-XSC. The inlay shows the magnified region between m/z = 326 and 349 showing the main peak, identified as the sodium adduct of *p*-XSC.

2.3.2 Cell compatibility and cellular uptake evaluation

In order to choose a suitable range of condition for cell study, different amounts of capsules were added ($N_{capsule/cell}$) and cell viability was measured using a resazurin based assay. A human cervical carcinoma cell line (HeLa) was used as a well-recognized *in vitro* model for cytotoxicity evaluation.[214] N_{cell} = 7,500 cells were hereby seeded in a volume of V_{medium} = 0.1 mL and exposed to the PEC. The 5 µm PEC sediment and stick to the bottom of the wells,

which are used as cell culture substrate. Similar to previous studies, empty biodegradable capsules showed decrease cytotoxicity only at high exposure concentrations $N_{capsule/cell} > 10$ (Figure 29A). [215] For capsules filled with p-XSC, the capsules exposure concentration was not determined by counting of the capsules, but by quantification of Se and thus of p-XSC in solution with ICP-MS ($C_{p\text{-}XSC}$). Then by knowing the mass of p-XSC per capsule ($m_{p\text{-}XSC/capsule}$) as described above. The number of capsules added per cell could be calculated as: $N_{capsule/cell} = (C_{p\text{-}XSC}/m_{p\text{-}XSC/capsule})\cdot V_{medium}/N_{cell}$. Non-biodegradable p-XSC filled capsules exhibited cytotoxic effect whith an EC_{50} value of 4.20 ± 0.48 µg/mL at 24 h and 9.7 ± 2.35 µg/mL at 48 h (Fig. 29B, Table 1). This cytotoxicity is slightly higher as compared to the empty biodegradable capsules, which might be due to a minimal leakage of p-XSC from the capsules under the harsh conditions after endosomal uptake (Figure 2B). Biodegradable (PARG/DEX) capsules filled with p-XSC started to induce cellular toxicity with an EC_{50} value of 2.37 ± 0.12 µg/mL at 24 h and 2.02 ± 0.05 µg/mL at 48 h (Figure 29C). This is assumed to be due the degradation of the capsule shells and thus presence of p-XSC inside endosomes/lysosomes, similar to that of free p-XSC (which will be discussed in detail later-on in the XFI section). Free p-XSC dissolved in serum supplemented media showed the highest cytotoxic response for HeLa cells, with EC_{50} values of 1.16 ± 0.15 µg/mL at 24 h and 0.98 ± 0.07 µg/mL at 48 h. The lower cytotoxicity of the encapsulated compound compared to the free drug during this time frame is similar to previously reported studies of doxorubicin loaded (PARG/DEX) capsules.[216] Interestingly the incubation time in our experiment (24 h *versus* 48 h) did not have a significant effect regarding the toxicity induced by the capsules under the investigated exposure conditions. One possible explanation could be that cell proliferation during the prolonged incubation time (24 h) compensate capsules induced cytotoxicity.

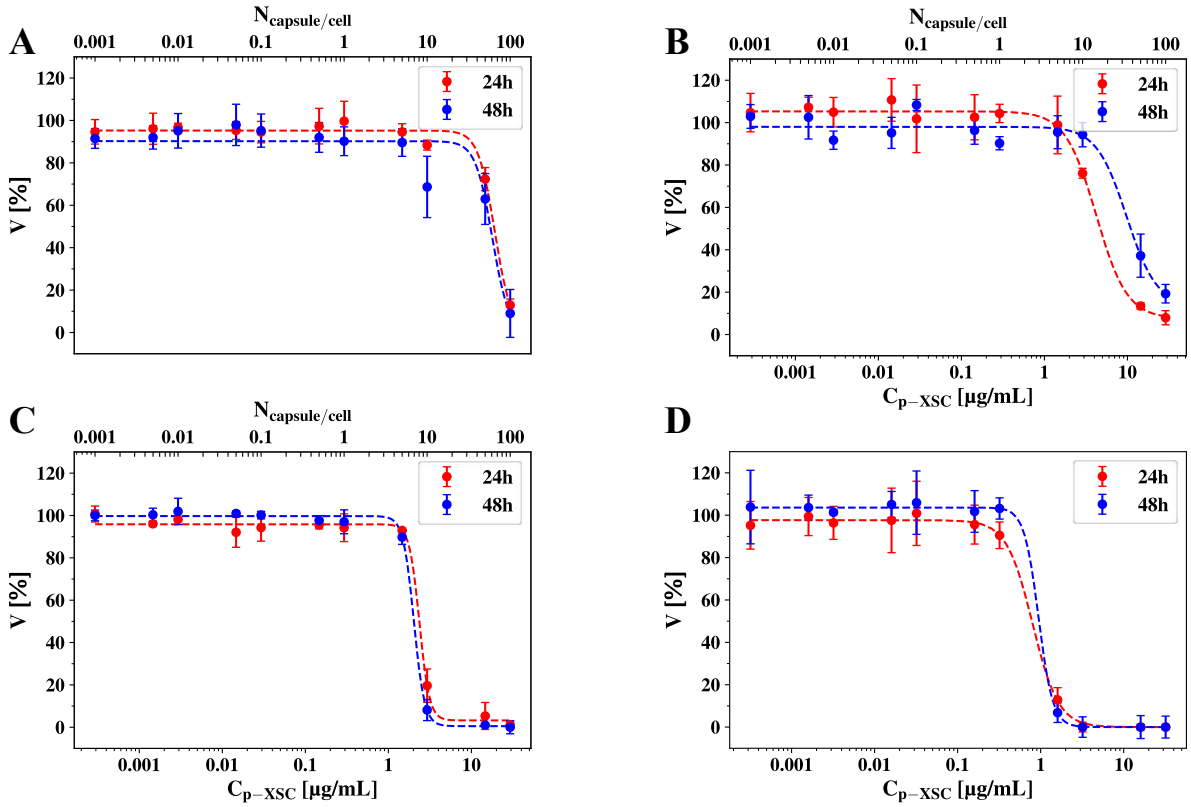

Figure 29: Resazurin based cell viability (V) assay results of HeLa cells incubated for 24 h (blue) or 48 h (red) in serum supplemented medium in presence of different compounds, A) empty biodegradable capsules, B) Se filled non-biodegradable capsules, C) Se filled biodegradable capsules, and D) free p-XSC. The displayed results depict mean values (dots) in % with their standard deviation from three individual assays. In the case of PEC loaded with p-XSC the exposure concentration is display as number of capsules added per seeded cell $N_{capsule/cell}$ and the concentration of p-XSC $C_{p\text{-}XSC}$ in the medium of volume V_{medium}. The dashed lines represent the fits of four-parameter-logic function used to calculate EC_{50} – values.

Table 1: Calculated EC_{50} values obtained from the experimental data, fitted by a four-parameter-logistic function, for all different conditions used for the experiments. EC_{50} values are expressed either in $C_{p\text{-}XSC}$ [µg/mL], for selenium containing compounds, and/or $N_{Capsules/Cell}$ for compounds consisting of PEC. R^2 as goodness of fit parameter shows that all fits are in appropriate agreement with the experimental data.

Composition	$(PARG/DEX)_4$		p-XSC@ $(PAH/PSS)_4$		p-XSC@ $(PARG/DEX)_4$		p-XSC	
Incubation time [h]	24	48	24	48	24	48	24	48
$C_{p\text{-}XSC}$ [µg/mL]	-	-	4.20 ± 0.48	9.77 ± 2.35	2.37 ± 0.12	2.02 ± 0.05	1.16 ± 0.15	0.98 ± 0.07
$N_{Capsules/Cell}$	67.77 ± 31.81	58.89 ± 34.92	13.36 ± 1.95	34.83 ± 9.49	8.48 ± 0.37	7.37 ± 0.20	-	-
R^2	0.988	0.915	0.993	0.968	0.996	0.999	0.999	0.999

ICP-MS was used to confirm the cellular uptake of p-XSC and quantify the intracellular amount $m_{p\text{-}XSC/}$cell. This technique allowed to quantify the mass of intracellular Se ($m_{Se/cell}$) and from this the mass of intracellular p-XSC was calculated ($m_{p\text{-}XSC/cell} = m_{Se/cell} \cdot (M_{p\text{-}XSC}/2M_{Se})$). HeLa cells were exposed to serum supplemented medium ($V_{medium} = 2$ mL, $N_{cell} = 200{,}000$) containing different concentrations of p-XSC ranging from 0 ~ 15 µg/mL of p-XSC filled $(PAH/PSS)_4$ and $(PARG/DEX)_4$ capsules, and free p-XSC drug for 24 h and 48 h (Figure 30). It is assumed that p-XSC (and in particular PEC) not internalized by cells was removed by washing steps before ICP-MS analysis.[202] For the non-degradable PEC the overall amount of intracellular p-XSC is lower, which is possibly due to reduced uptake of $(PAH/PSS)_4$ *versus* $(PARG/DEX)_4$ PEC, *i.e.* dependent on the PEC carrier matrix, or due to excretion of the whole capsule without releasing the encapsulated drug (which according to their size is however not likely).[125] The detected amount of p-XSC was comparable between biodegradable PEC loaded p-XSC *and* free p-XSC for all tested exposure concentrations.

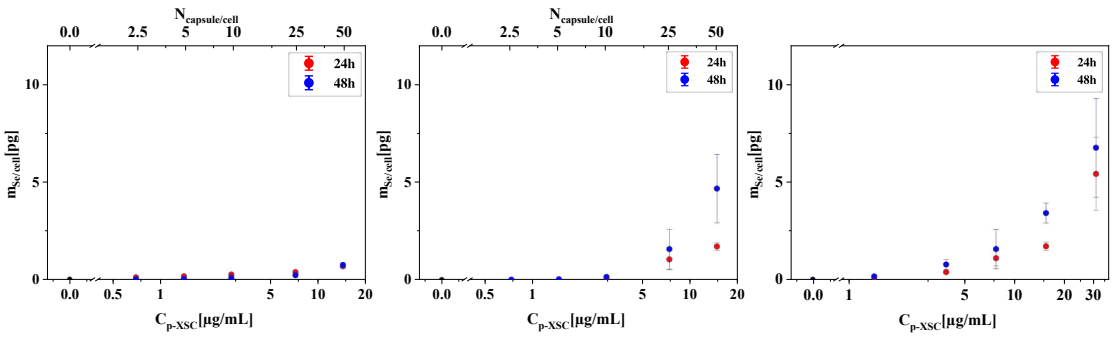

Figure 30: Uptake study of HeLa cells incubated for 24 h (blue) and 48 h (red) with medium containing A) non-biodegradable $(PAH/PSS)_4$ p-XSC filled capsules, B) biodegradable $(PARG/DEX)_4$ p-XSC filled capsules, and C) free p-XSC in different concentrations. The detected amount of Se for untreated cells ($C_{p\text{-}XSC}$ = 0 µg/mL) was below the detection limit of the ICP-MS, indicated by • in the figure.

2.3.3 X-ray fluorescence imaging

ICP-MS analysis only allows the quantification of the amount of p-XSC inside cells, without the information about its intracellular location. Intracellular p-XSC distribution in HeLa cells was further investigated using XFI. Before imaging Se treated HeLa cells were cryo-fixed and freeze dried. First coarse scans were acquired with an incident beam energy of 17 keV, focused to 2.7 µm × 1.5 µm (FWHM, h × v) with a step size of 1.5 µm × 1.5 µm to identify cells suitable for fine imaging, chosen by their shape, intense K - K_α and Se - K_α emission. This was followed by high resolution scans (beam size FWHM: 420 nm × 260 nm, 300 nm × 300 nm step size, 100 ms dwell time).

The spectra were consecutively fitted using PyMCA allowing to identify and distinguishe emissions from different elements. A representative spectrum from a HeLa cell without p-XSC treatment (A) and one for a treated cell (B) is shown in Figure 31.

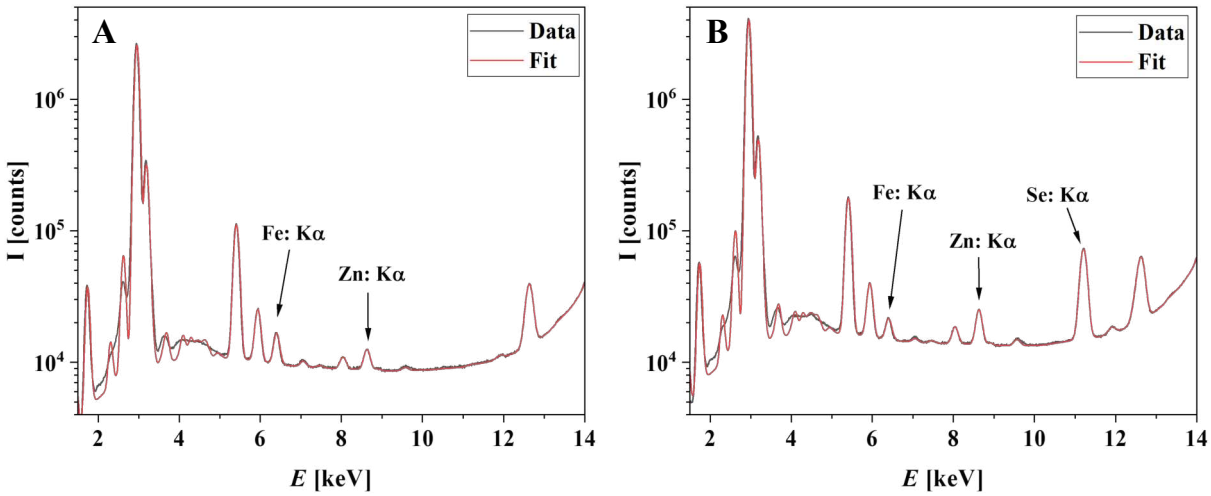

Figure 31: Summed X-ray fluorescence spectra I(E) for A) HeLa cell treated with empty biodegradable capsules for 24 h, and B) HeLa cell treated for 24 h with p-XSC-filled biodegradable capsule, showing an additional Se peak.

By fitting of each individual spectrum for the cellular maps under different conditions, and minding the concentration correction factors obtained by the standard measurement, quantitative 2-dimensional images were obtained. One representative image for each condition is shown in Figure 32, and all other images used for analysis can be found in the Appendix (Figures A11 – A14). The K_α emission of K was utilized throughout the experiments to trace and define the cellular outlines for whole cell quantification (Figure 32, first column). The Zn K_α emission depicts mostly the cellular nucleus, thus a clear and intense signal represents vital cells before cryo-preservation (Figure 32, second column).

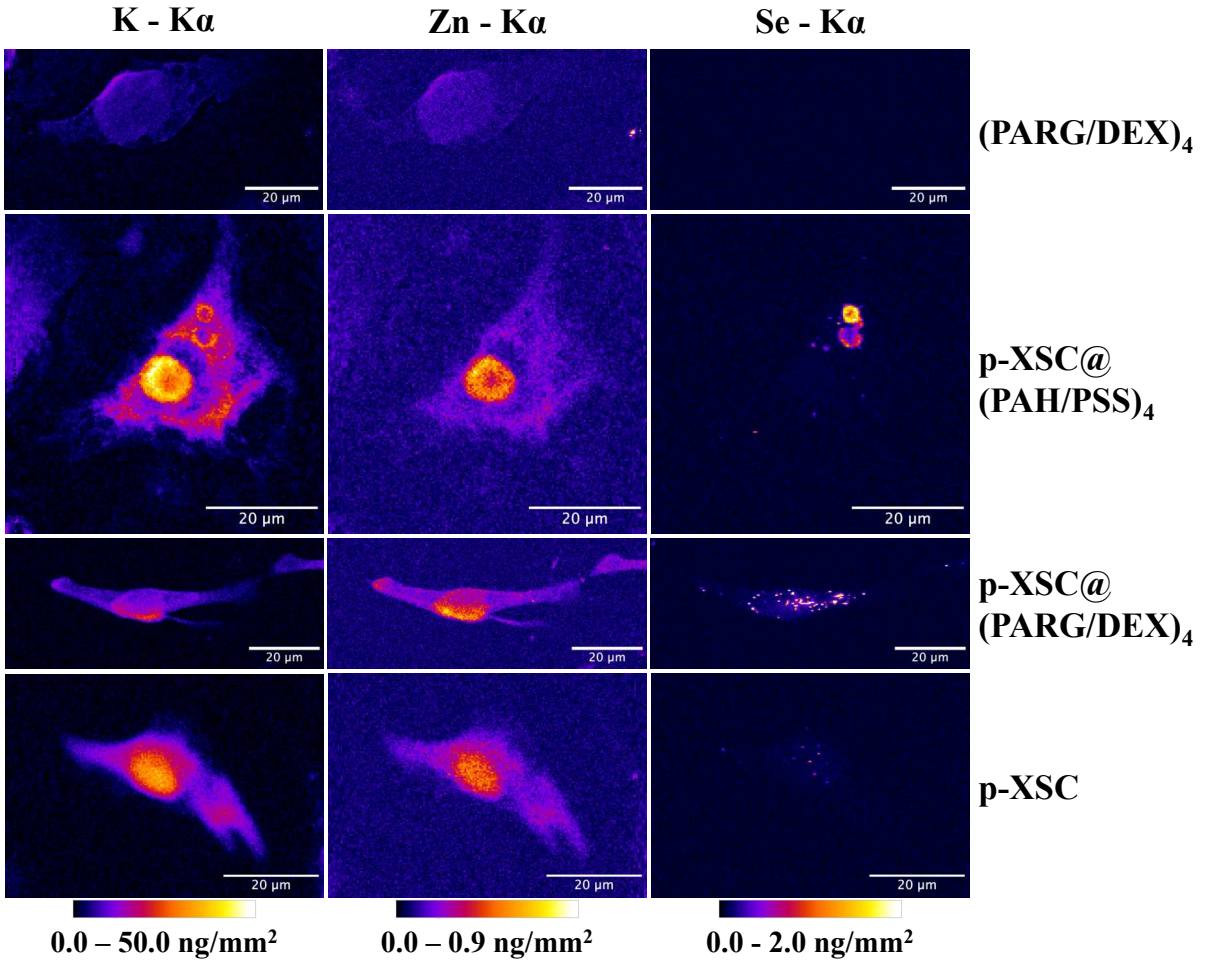

Figure 32: Pseudo-coloured X-ray fluorescence images comparing the intracellular distribution density of different elements (ρ_K, ρ_{Zn}, and ρ_{Se}) after exposure to p-XSC using different vehicles. The signals originated from the K K_α emission (first column), Zn K_α emission (second column), and Se K_α emission (third column). The control HeLa cells in the first row were treated with biodegradable unfilled capsules $(PARG/DEX)_4$. In the next row non-biodegradable $(PAH/PSS)_4$ p-XSC-filled capsules were employed. In the third row cells were exposed to p-XSC-filled biodegradable $(PARG/DEX)_4$ capsules. In the last row cells had been exposed to free p-XSC. The scale bars indicate 20 µm.

Detection of the signal from natural intracellular Se was determined by imaging one cell treated with biodegradable capsules $(PARG/DEX)_4$ without encapsulated p-XSC ($N_{capsule/cell}$ = 3, 24 h exposure; Figure 4 first row). As the cells were not exposed to p-XSC, the obtained Se signal represents the background caused by inherent intracellular selenium. Using potassium emission as a mask for the cellular area (A_{cell}), the integrated p-XSC amount was determined to be $m_{p\text{-}XSC/cell}$ = 0.015 pg in the control cell (again, the p-XSC mass was calculated from the Se mass as derived from the Se signal; $m_{Se/cell}$ = 0.0075 pg). The XFI map represents the complete intracellular distribution of the Se (*i.e.* Se in the projection of the whole cell), whereby all metal

atoms are excited and emit uniformly across the cell, as absorption interference from the soft cellular tissue is negligible in this energy range. In this way the intracellular average area concentration can be calculated as $\rho_{p\text{-}XSC} = m_{p\text{-}XSC/cell}/A_{cell} = 5$ pg/mm^2 ($\rho_{Se} = 2.5$ pg/mm^2).

In the 2nd row of Figure 32 the XFI image of a cell that had been exposed to non-biodegradable capsules $(PAH/PSS)_4$ containing p-XSC is shown ($N_{capsule/cell} = 3.5$, $C_{p\text{-}XSC} = 1$ µg/mL, 24 h exposure). As expected, a significant amount of p-XSC was retained within the capsules, indicating that the PEC shell had remained intact without degradation. p-XSC therefore remains inside the lysosomes in which the endocytosed PEC are located. However, XFI images indicated that a small amount of Se locates outside the capsules. This can be attributed to the leakage of p-XSC originating from the capsules. Inside cells on average $m_{p\text{-}XSC/cell} = 0.061 \pm 0.017$ pg p-XSC was detected ($m_{Se/cell} = 0.031 \pm 0.008$ pg), equivalent to $\rho_{p\text{-}XSC} = 91 \pm 7$ pg/mm^2 ($\rho_{Se} = 45 \pm 4$ pg/mm^2).

The intracellular location of Se was different when Hela cells were treated with biodegradable capsules $(PARG/DEX)_4$ loaded with p-XSC ($N_{capsule/cell} = 3.4$, $C_{p\text{-}XSC} = 1$ µg/mL, 24 h exposure). Se is no longer localized with the PEC but distributed as grainy structure over the whole cell area (Figure 4, 3rd row). This indicates that the PEC shell of endocytosed capsules was degraded, and the previously encapsulated p-XSC has relocated from the lysosome where the PEC had located after endocytosis. The XFI imaging is not able to differentiate if the released cytosolic Se is present in free form, or located in small intracellular vesicles, similar to previous reported degradation studies based on fluorescence.[217] Quantitative data revealed an average p-XSC area density of $\rho_{p\text{-}XSC} = 558 \pm 370$ pg/mm^2 ($\rho_{Se} = 280 \pm 186$ pg/mm^2). Based on the cellular area, Se density is converted to to $m_{p\text{-}XSC/cell} = 0.175 \pm 0.017$ pg p-XSC per cell ($m_{Se/cell} = 0.088 \pm 0.008$ pg), which is closely to the result obtained by ICP-MS quantification ($m_{Se/cell} = 0.203 \pm 0.032$ pg). A comparison of the intracellular p-XSC amount as determined by ICP-MS and XFI for all the groups is shown below (Figure 33).

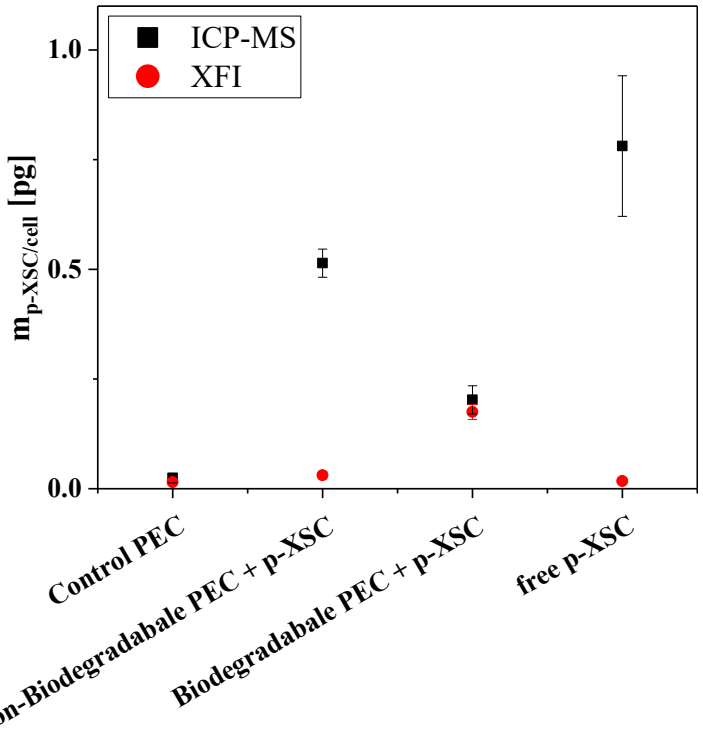

Figure 33: Comparison of the amount of intracellular Se as determined by ICP-MS (black) and XFI (red) for different administration conditions.

Cells were also exposed to free p-XSC (Figure 32 4th row; $C_{p\text{-}XSC}$ = 1 µg/mL, 24 h exposure). It was anticipated that due to the hydrophobic nature of p-XSC only a small amount could be internalized by the cell (*i.e.* p-XSC sequestered by albumin and thus entering cells via endocytosis of albumin).[218] The XFI measurement indicates a low Se signal from the p-XSC in the intracellular area. By integrating the semi-quantitative p-XSC amount over whole cellular area, $m_{p\text{-}XSC/cell}$ = 0.017 ± 0.005 pg p-XSC was detected per cell ($m_{Se/cell}$ = 0.008 ± 0.003 pg), which is not significantly higher as compared to the control cell. However, keeping the cellular area in mind, and thus neglecting the individual cellular size, the p-XSC amount per area is indeed higher $\rho_{p\text{-}XSC}$ = 64 ± 2 pg/mm^2 (ρ_{Se} = 32 ± 1 pg/mm^2). However, the $m_{Se/cell}$ value as obtained with ICP-MS is much higher than the one as obtained from the XFI data (*cf.* Figure 33). In addition, after exposure to free p-XSC, intracellular p-XSC is distributed in grainy structure across the whole cell area, similar to the location pattern observed in cells treated with p-XSC loaded biodegradable capsules. Again, also here XFI does not allow to distinguish between p-XSC free in the cytosol and p-XSC located in small intracellular vesicles.

In most cases the quantitative results of intracellular p-XSC ($m_{p\text{-}XSC/cell}$) are different between the ICP-MS and XFI measurements, whereby the ICP-MS values are in general higher (*cf.*

Figure 33). In both cases the signal originates from elemental Se in p-XSC. In general, the ICP-MS values should be more reliable for the absolute quantification of the amount of intracellular Se. ICP-MS values are obtained as average value derived from ~ 200,000 cells. On the other hand, with XFI individual cells were imaged and the average value was calculated based on only 4 cells in this work. Due to longer measurement procedure (in the present work the time to collect one of the images shown in Figure 32 was around 180 min, depending on the cellular area) the statistics in XFI will be worse in general as compared to ICP-MS. In addition, as XFI records the distribution of p-XSC, a more complicated sample is required, as here done by cryo-fixation, followed by freeze drying. During this preparation step some intracellular p-XSC may have been lost, as the cells were chemically detached from the wells after 24h of treatment and transferred on SiNx membranes. This process was in our case, necessary as previous experiments showed PEC tend to bind on SiN_x membranes and thereby increase the background signal of Se.

On the other hand, to visualize the intracellular Se distribution, XFI is needed, as ICP-MS cannot provide any lateral resolution. Only XFI, but not ICP-MS can provide the evidence regarding whether p-XSC is still located in the original lysosomes where it has been delivered with the PEC, or if it is distributed across the whole cell. XFI tells also, that in the present case washing to remove p-XSC that has not been endocytosed by cells, and was sticking only to the outer cell membrane (either in free or encapsulated form)[219] does not play a significant role, as it was not observed in the images shown in Figure 32.

In this study, we investigated the intracellular Se amount and Se location in HeLa cells after receiving the treatment of p-XSC in different formulations. In summary, p-XSC encapsulated in nondegradable PEC remains to a large amount within the PEC (XFI, Figure 32) and thus is not biologically effective, *i.e.* does impair cell viability (resazurin assay, Figure 29). When comparing the delivery of free p-XSC versus p-XSC encapsulated in biodegradable PEC, there is comparable uptake of p-XSC as delivered in free form and encapsulated in biodegradable PEC (ICP-MS, Figure 30). In the present case thus, the encapsulation does not improve the intracellular p-XSC concentration. In both formulations, p-XSC is spread across the whole cell in the same grainy pattern (XFI, Figure 32), suggesting a similar intracellular biodistribution. The cytotoxicity of free p-XSC is higher than encapsulated p-XSC (viability assay, Figure 29). This may be due to the biodegradable PEC are not fully degraded and p-XSC is not fully released.

Despite the current study using HeLa cells did not show apparent advantage of loading p-XSC in biodegradable capsules this may be due to the limited number of cancer cell lines investigated. It was reported before that p-XSC is effective in leukemia cell lines, whereas in other cell lines the effect of p-XSC transport *via* endocytosis of serum albumins [218] is less pronounced.[201] The plan is to further investigate such an anti-cancer effect through study intracellular distribution of p-XSC in other hematological cancers and solid tumor cells more comprehensively.

2.3.4 Conclusion

Using X-ray fluorescence imaging (XFI) and ICP-MS, this study demonstrates the dynamic intracellular distribution of an organic Se compound and its intracellular uptake as delivered in different formulations. XFI proves to be a very suitable method for characterizing the intracellular localization of drugs containing metals and determining quantitative values after internalization. However, due to the tedious sample preparation procedure (*e.g.* cryo-preservation), complementary methods for the quantification of absolute Se amount (*e.g.* ICP-MS) are important.

While our findings did not reveal a notable improvement in cellular uptake or cytotoxicity with encapsulated p-XSC, our investigation offers crucial insights into the efficacy of this encapsulation approach. Importantly, our investigation utilized X-ray fluorescence imaging (XFI) to unravel the intracellular pathway of the Se compound and validate its lysosomal escape and redistribution inside mammalian cells. This highlights the utility of XFI as a precise and non-invasive method for tracking the intricate dynamics of hydrophobic metal-based substances delivered *via* polyelectrolyte capsules. Our study explored using of XFI to study intracellular level dynamic of p-XSC and its encapsulated formulation in combination with its anti-cancer efficacy, which may advance the field of future targeted therapeutics and improve treatment outcomes for various diseases. Furthermore, due to the properties of the polyelectrolyte capsules including biocompatibility and the ability of co-loading with different drugs such as anticancer drugs and contrast agents they hold the prospect for development aiming at improved anticancer therapies. Further research should aim at the use of external stimuli *e.g*. light, ultrasound or magnetic field to provide controlled in-situ drug release or synergetic therapeutic effect in tumor.

3 Conclusion

This thesis presents a comprehensive examination of two advanced synchrotron-based methodologies for the characterization and analysis of nano- and microparticle interactions with biological entities, focusing on intracellular environments. By exploiting advanced imaging (X-ray fluorescence imaging) and analytical techniques (anomalous small angle X-ray scattering), this study has contributed to a more insightful understanding of nanoparticle behavior and their promising applications in biomedical fields.

In the first project, the intracellular fate of a pre-formed protein corona around gold nanoparticles is investigated using X-ray fluorescence imaging. The results demonstrate that the technique is capable of following this degradation process to a certain degree, indicated by a lower colocalization and decreased molar ratios, specifically inside trafficking vesicles. The study is constrained by cell-to-cell variations and small sample populations, which are a consequence of the lengthy acquisition times inherent to state-of-the-art nano-focused X-ray fluorescence imaging experiments. In the future, the use of next-generation synchrotron facilities will allow for the analysis of a larger number of samples, as the increased photon flux will significantly reduce the acquisition time for these experiments. Furthermore, a triple-labeled system was developed, consisting of a gold nanoparticle core, a mixed polyethylene glycol layer bearing bromine tags, and a Gd-labeled protein forming the corona. The system was comprehensively characterized through a comparison of dynamic light scattering and anomalous small-angle X-ray scattering. The results obtained thereby confirmed that aSAXS is indeed capable of providing crucial information about the individual parts of the system. In comparison to dynamic light scattering, this methodology offers the advantage of being able to be employed after the system is fully formed, whereas DLS must be utilized between each modification. Furthermore, aSAXS can be employed in optically dense samples, such as tissue, and can be utilized as an imaging technique.

In the last chapter, the intracellular distribution of an organic selenium compound upon delivery in different formulations, including biodegradable polyelectrolyte capsules, was investigated using X-ray fluorescence imaging and inductively coupled plasma mass spectrometry. X-ray fluorescence imaging provided excellent mapping of the intracellular drug localization, highly suggesting the occurrence of lysosomal escape and redistribution. Despite these limitations observed with encapsulated drugs did not offer enhanced *in vitro* response compared to the non-encapsulated drug, this study supports the value of XFI in the improvement of innovative therapeutic strategies without exogenous labels.

4 Appendix

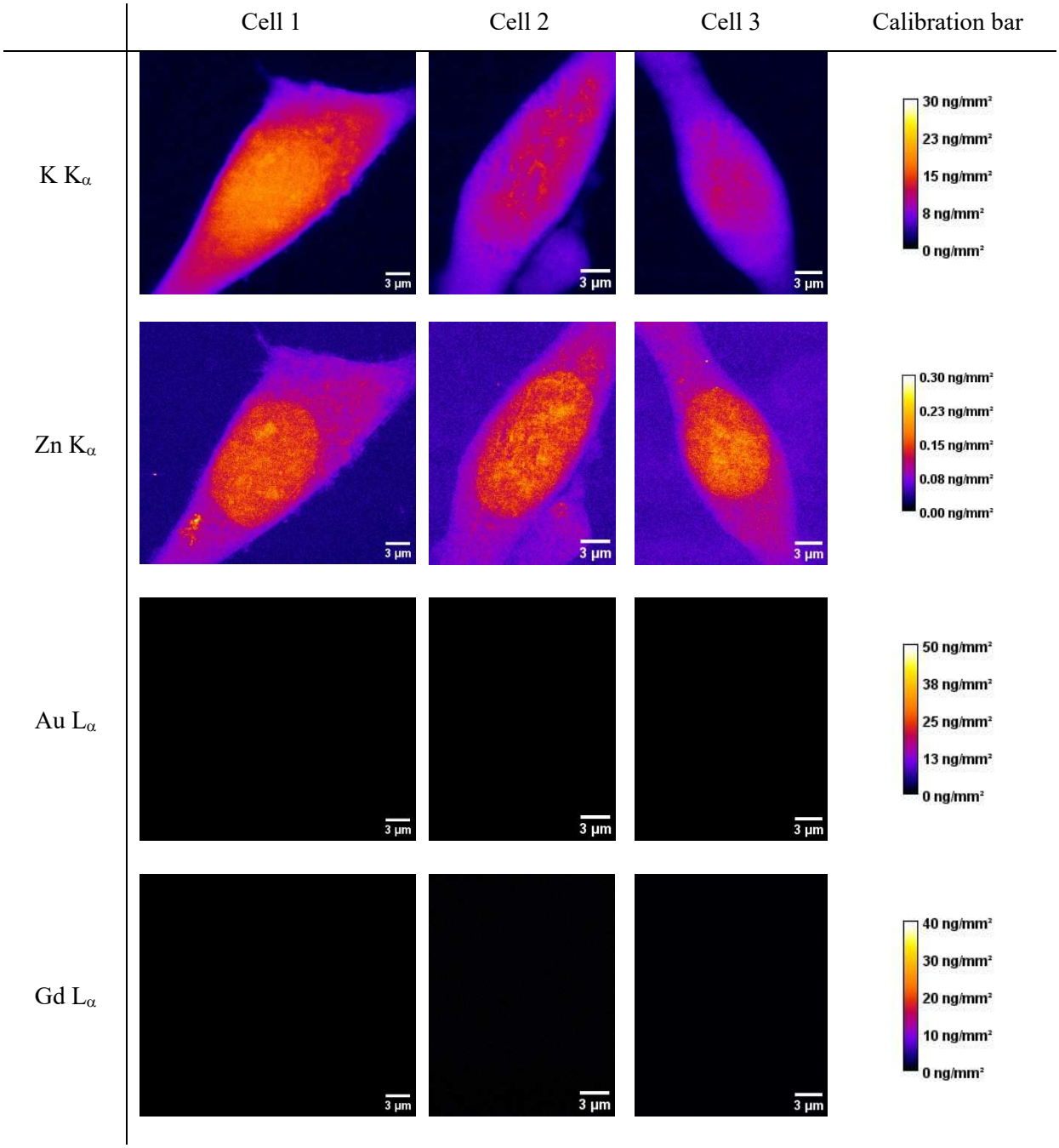

Figure A 1: Pseudo colored images of 3T3 cells kept in AMEM growth media for 24 h acquired by XFI. The signals originated from: K K_α emission (first row), Zn K_α emission (second row), Au L_α emission (third row), and Gd L_α emission (fourth row). The scale bars indicate 3 µm.

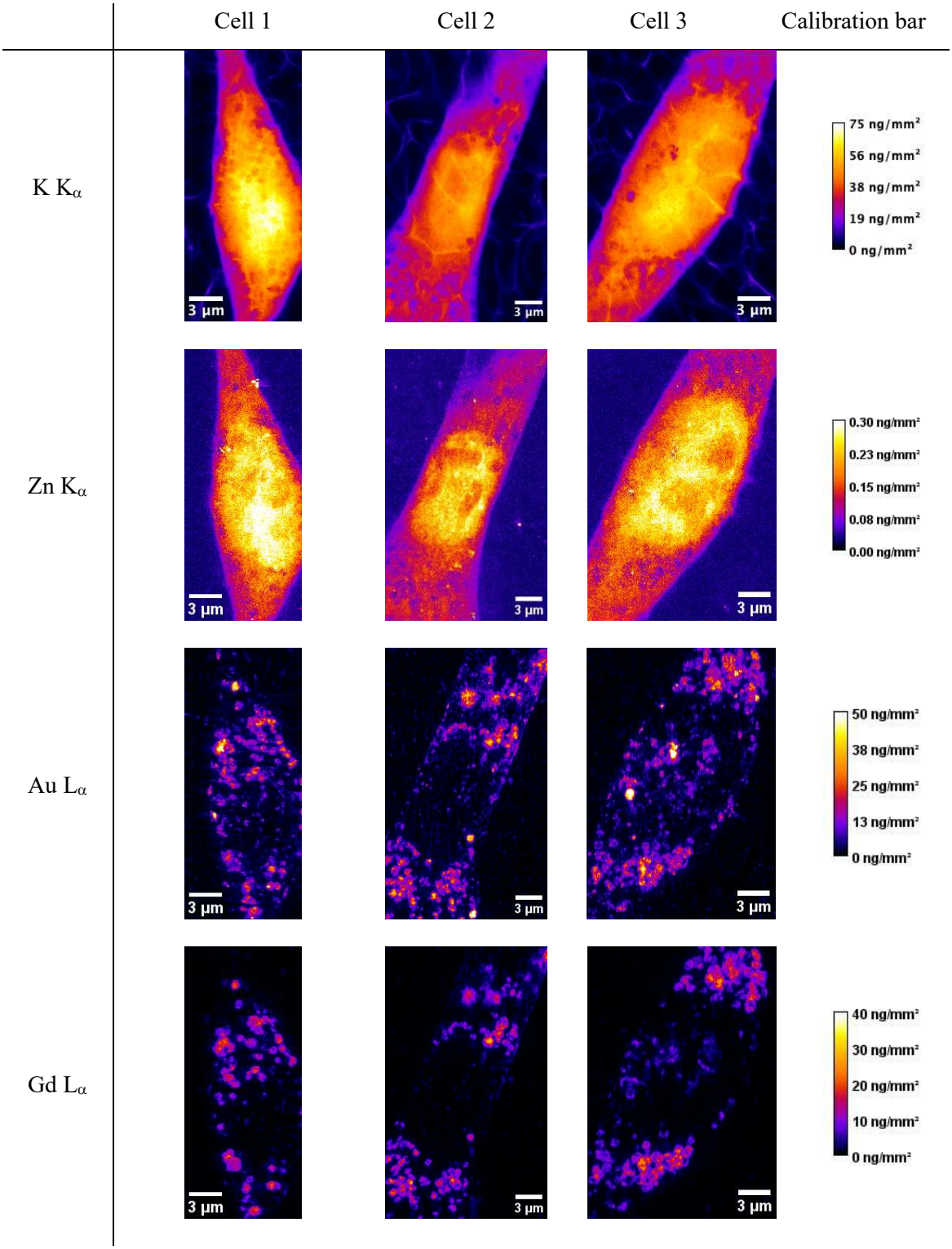

Figure A 2: Pseudo colored images of 3T3 cells after 24 h of exposure with AuNP@CTPR-Gd (C_{Au} ~10 µg/mL), without incubation time in NP-free medium ($t_{inc} = 0$), acquired by XFI The signals originated from: K K_α emission (first row), Zn K_α emission (second row), Au L_α emission (third row), and Gd L_α emission (fourth row). The scale bars indicate 3 µm.

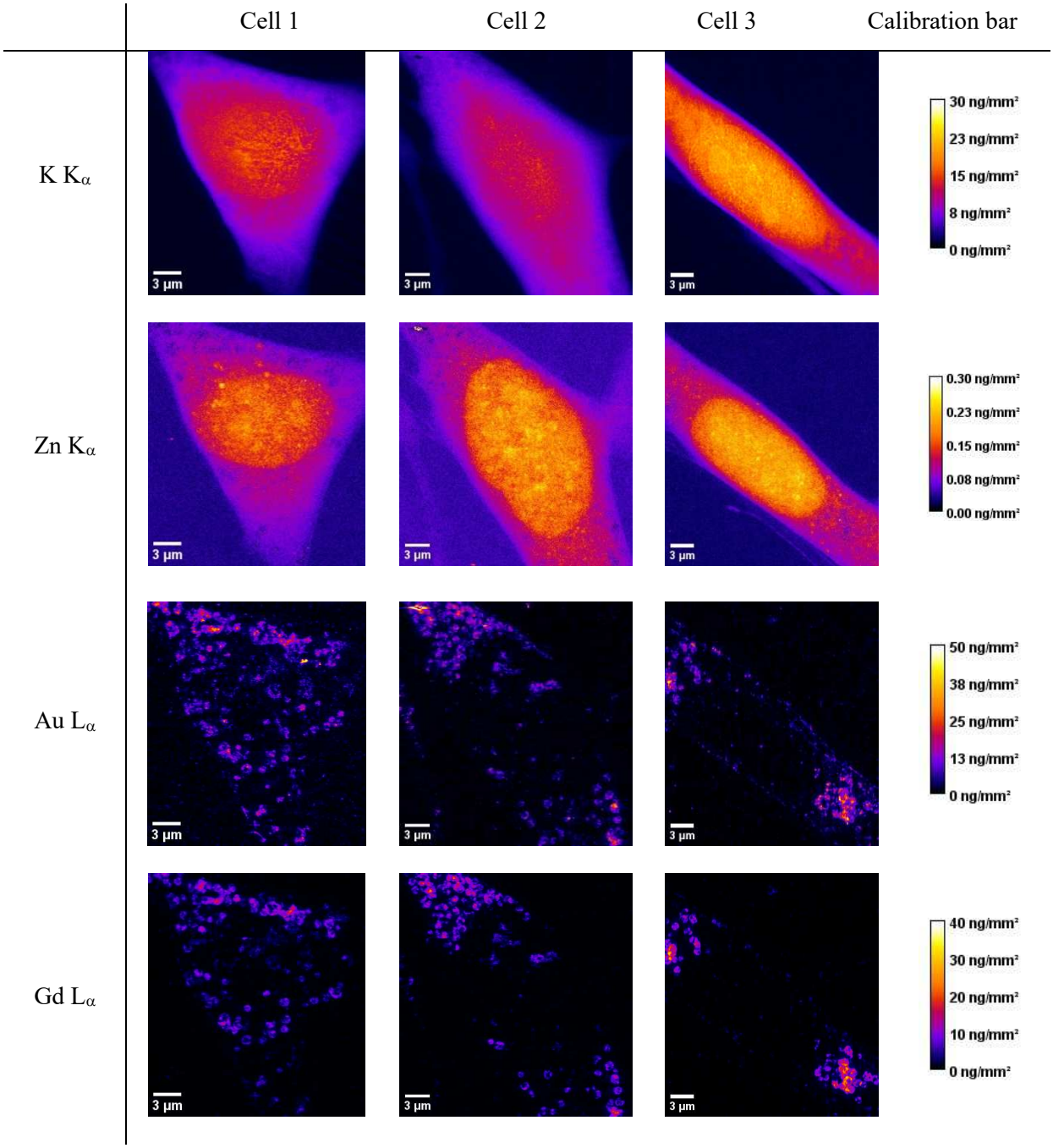

Figure A 3: Pseudo colored images of 3T3 cells after 24 h of exposure with AuNP@CTPR-Gd (C_{Au} ~10 µg/mL) followed by t_{inc} = 30 min incubation time in NP-free medium, acquired by XFI. The signals originated from: K Kα emission (first row), Zn Kα emission (second row), Au Lα emission (third row), and Gd Lα emission (fourth row). The scale bars indicate 3 µm.

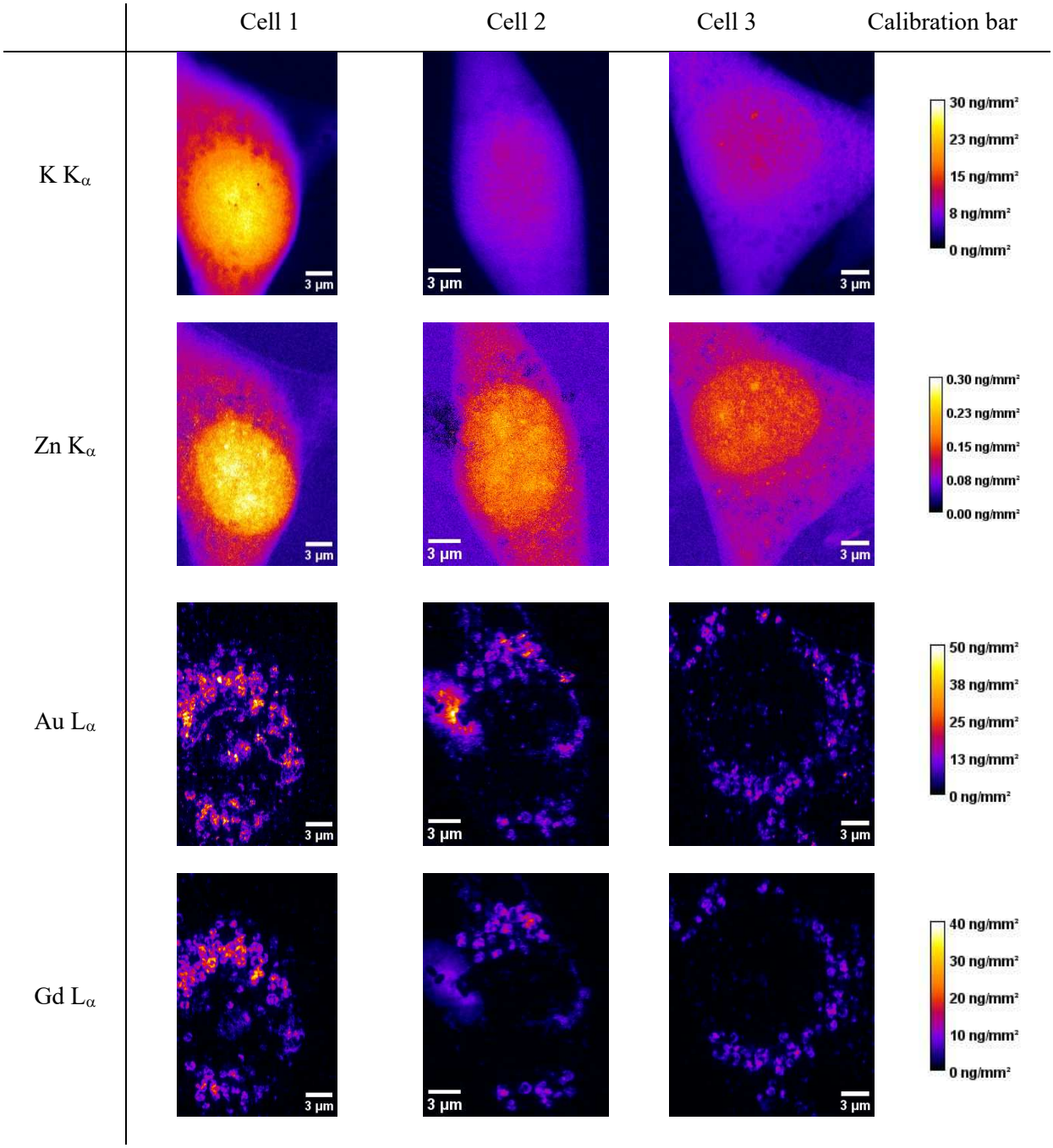

Figure A 4: Pseudo colored images of 3T3 cells after 24 h of exposure with AuNP@CTPR-Gd (C_{Au} ~10 µg/mL) followed by t_{inc} = 60 min incubation time in NP-free medium, acquired by XFI. The signals originated from: K Kα emission (first row), Zn Kα emission (second row), Au Lα emission (third row), and Gd Lα emission (fourth row). The scale bars indicate 3 µm.

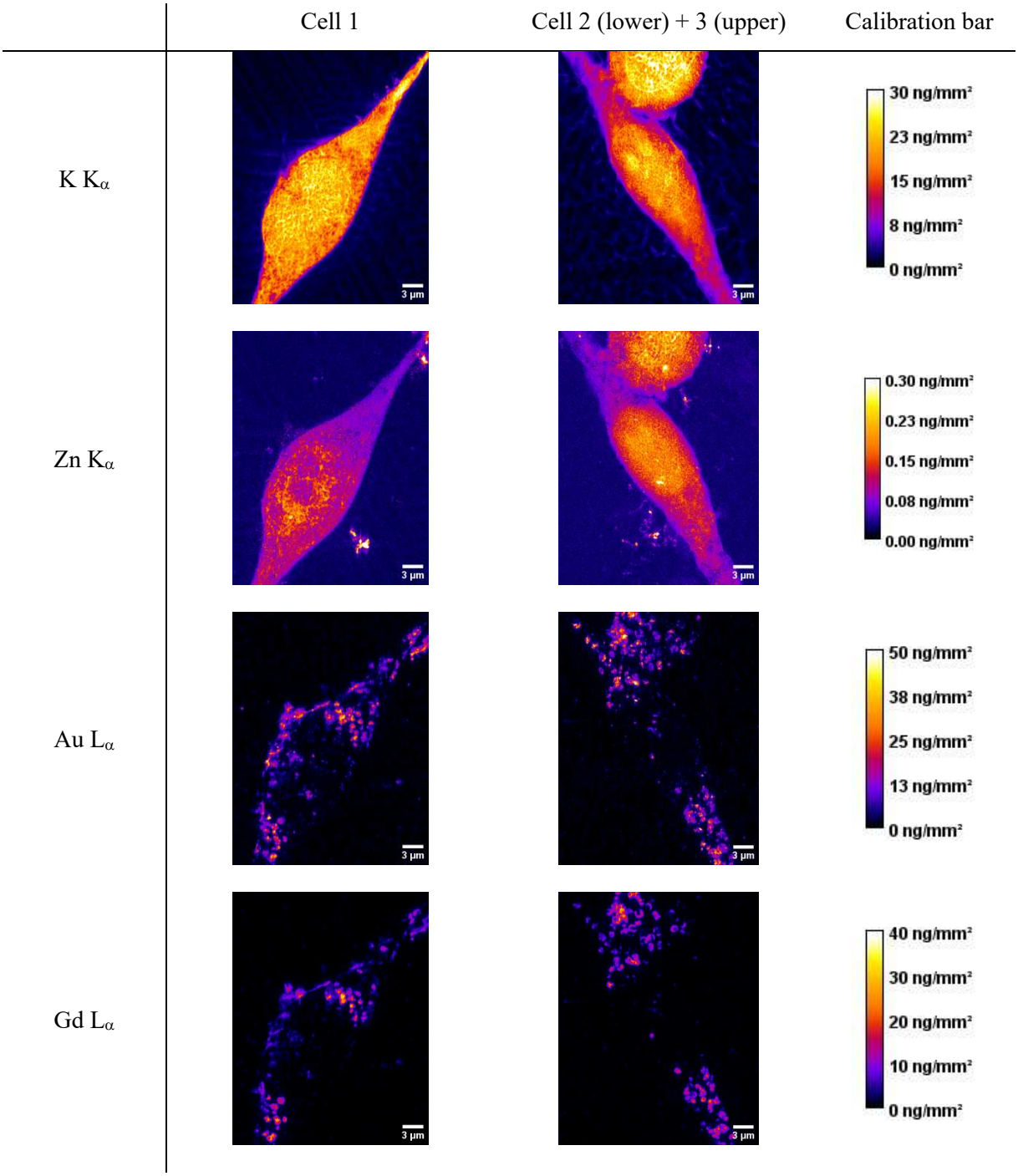

Figure A 5: Pseudo colored images of 3T3 cells after 24 h of exposure with AuNP@CTPR-Gd (C_{Au} ~10 µg/mL) followed by t_{inc} = 120 min incubation time in NP-free medium, acquired by XFI. The signals originated from: K K_α emission (first row), Zn K_α emission (second row), Au L_α emission (third row), and Gd L_α emission (fourth row). The scale bars indicate 3 µm.

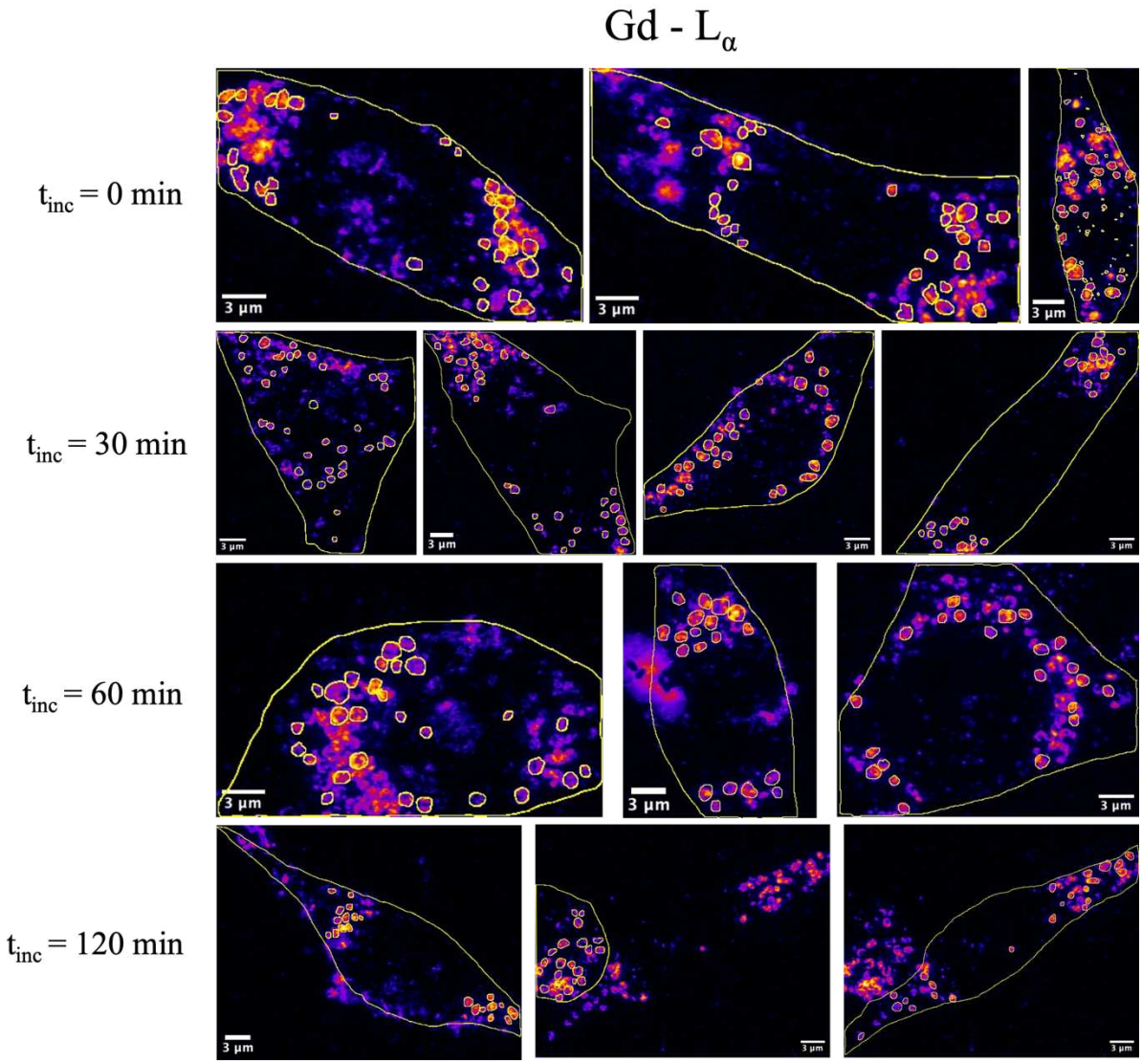

Figure A 6: Pseudo colored images of 3T3 cells after 24 h of exposure to AuNP@CTPR-Gd (C_{Au} ~10 µg/mL), followed by t_{inc} = 0 min incubation time in NP-free medium (first row), t_{inc} = 30 min (second row), t_{inc} = 60 min (third row), and t_{inc} = 120 min (fourth row). The signal originated from Gd L_α emission. Regions of interest as outlined in yellow, show nearly spherical structures, smaller than 1 µm in diameter, which were used for analysis. The scale bars indicate 3 µm.

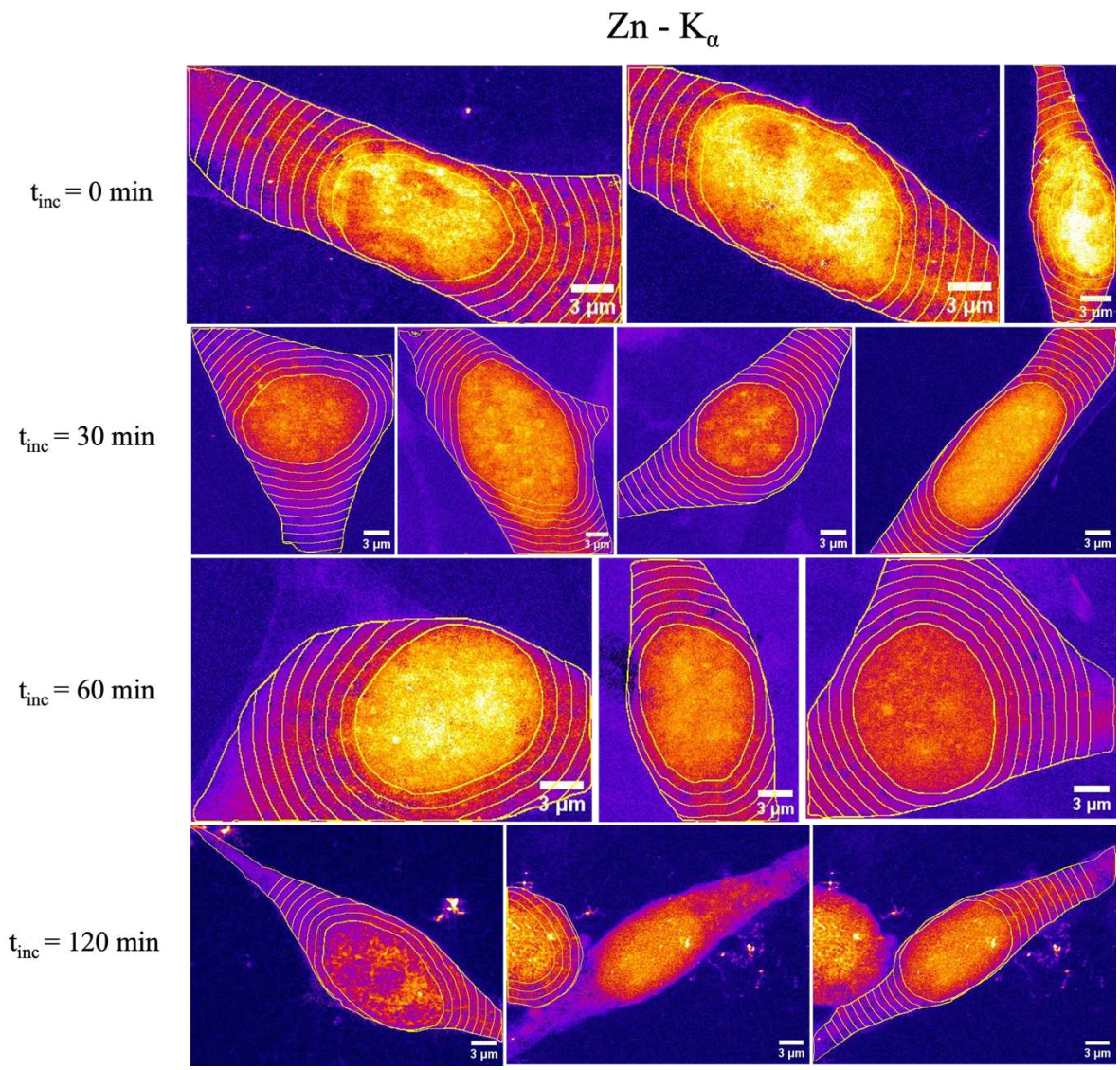

Figure A 7: Pseudo colored images of 3T3 cells after 24 h of exposure to AuNP@CTPR-Gd (C_{Au} ~10 µg/mL), without additional incubation time t_{inc} = 0 (first row), with additional t_{inc} = 30 min incubation time in NP-free medium (second row), t_{inc} = 60 min (third row), or t_{inc} = 120 min (fourth row), respectively. The signal originated from Zn K_α emission. Yellow regions of interest show cellular nuclei (inner circle) and subsequent 1 µm distance steps inside cells. The scale bars indicate 3 µm.

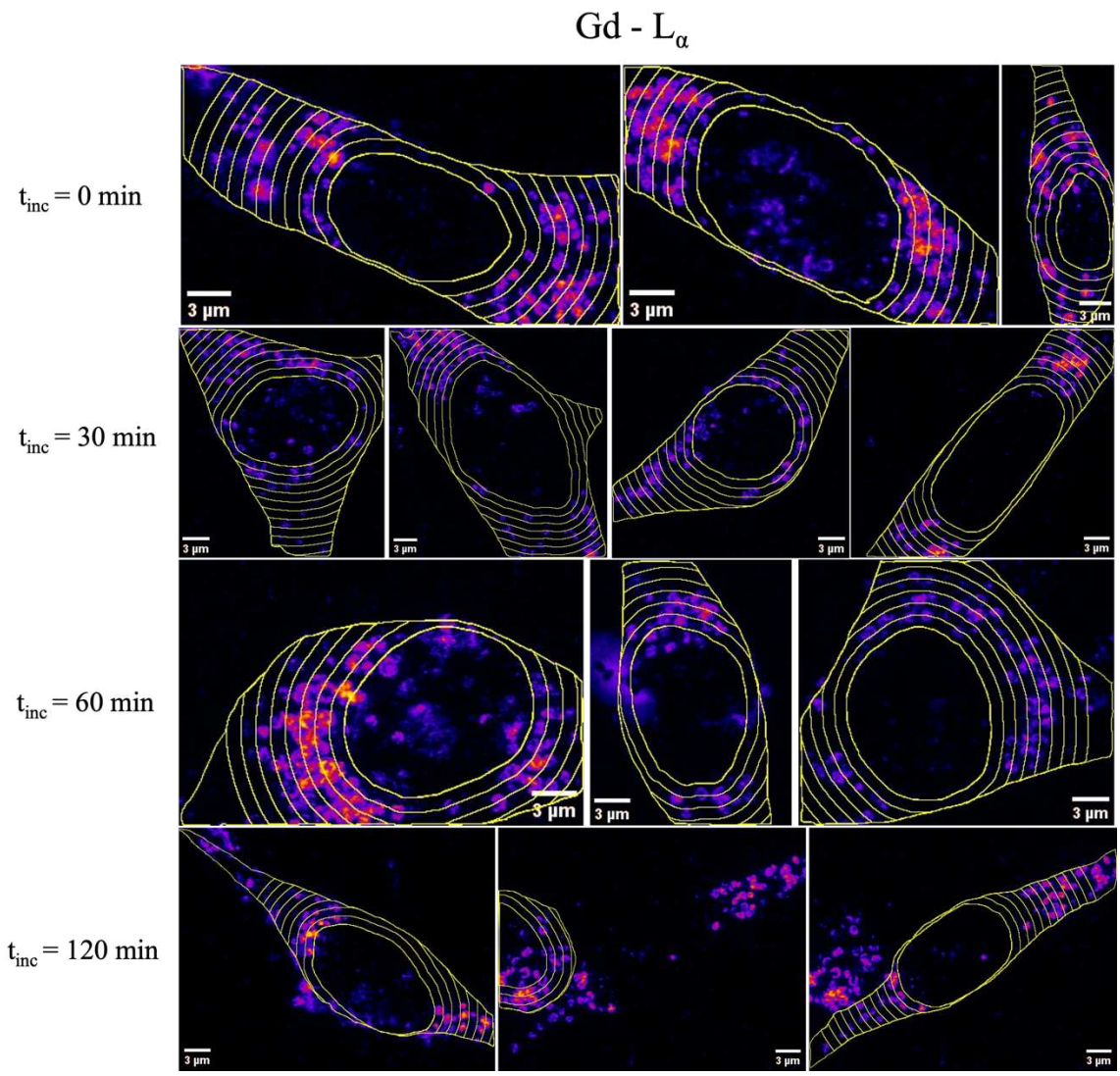

Figure A 8: Pseudo colored images of 3T3 cells after 24 h of exposure to AuNP@CTPR-Gd (C_{Au} ~10 µg/mL), without additional incubation time t_{inc} = 0 (first row), with additional tinc = 30 min incubation time in NP-free medium (second row), t_{inc} = 60 min (third row), or t_{inc} = 120 min (fourth row), respectively. The signal originated from Gd L_α emission. Yellow regions of interest show cellular nuclei (inner circle) and subsequent 1 µm distance steps inside cells. The scale bars indicate 3 µm.

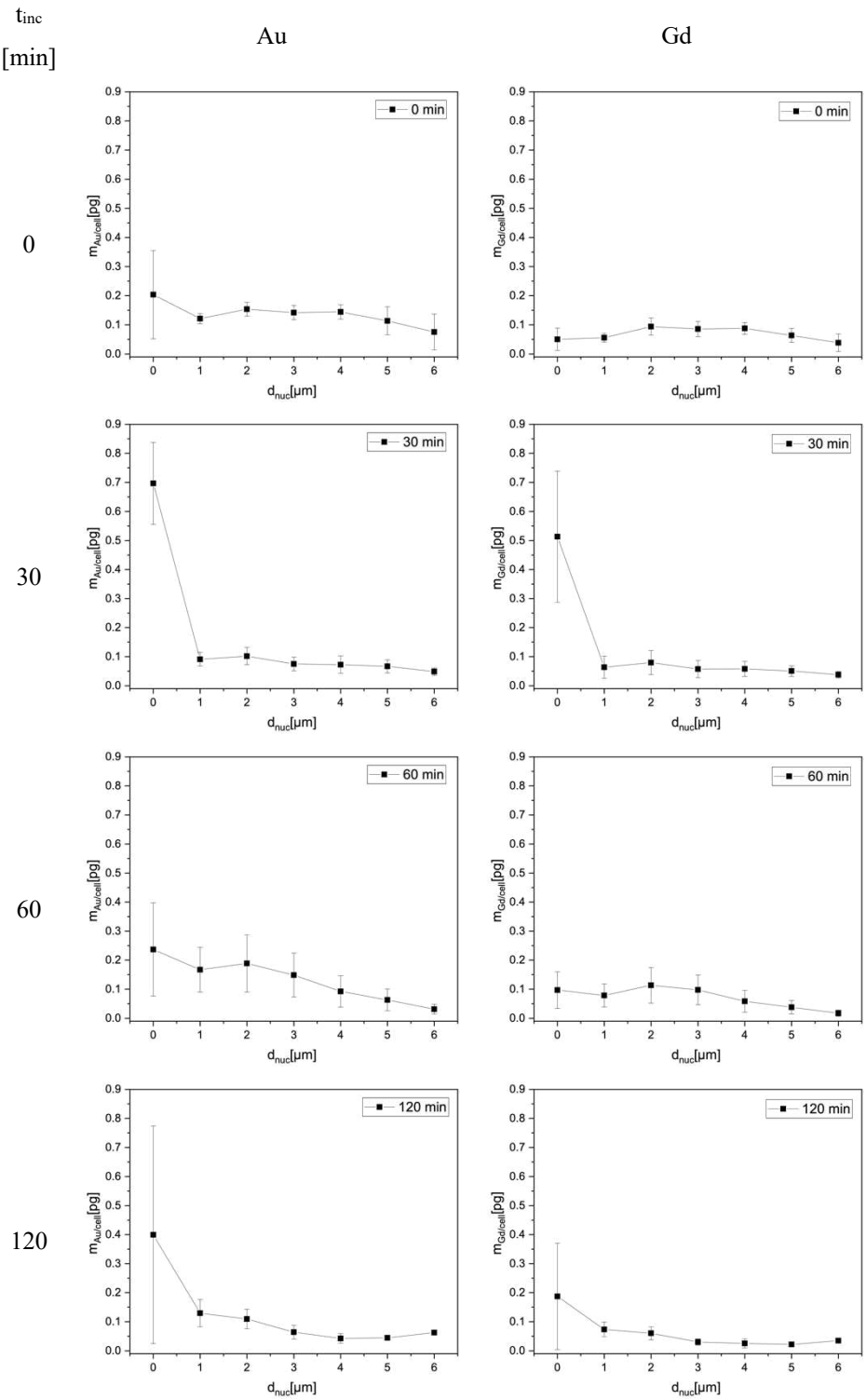

Figure A 9: Quantities of Au ($m_{Au/cell}$, left) and Gd ($m_{Gd/cell}$, right) for different incubation times in NP-free medium t_{inc} as a function of the distance to the cellular nucleus d_{nuc}, as calculated from XFI maps.

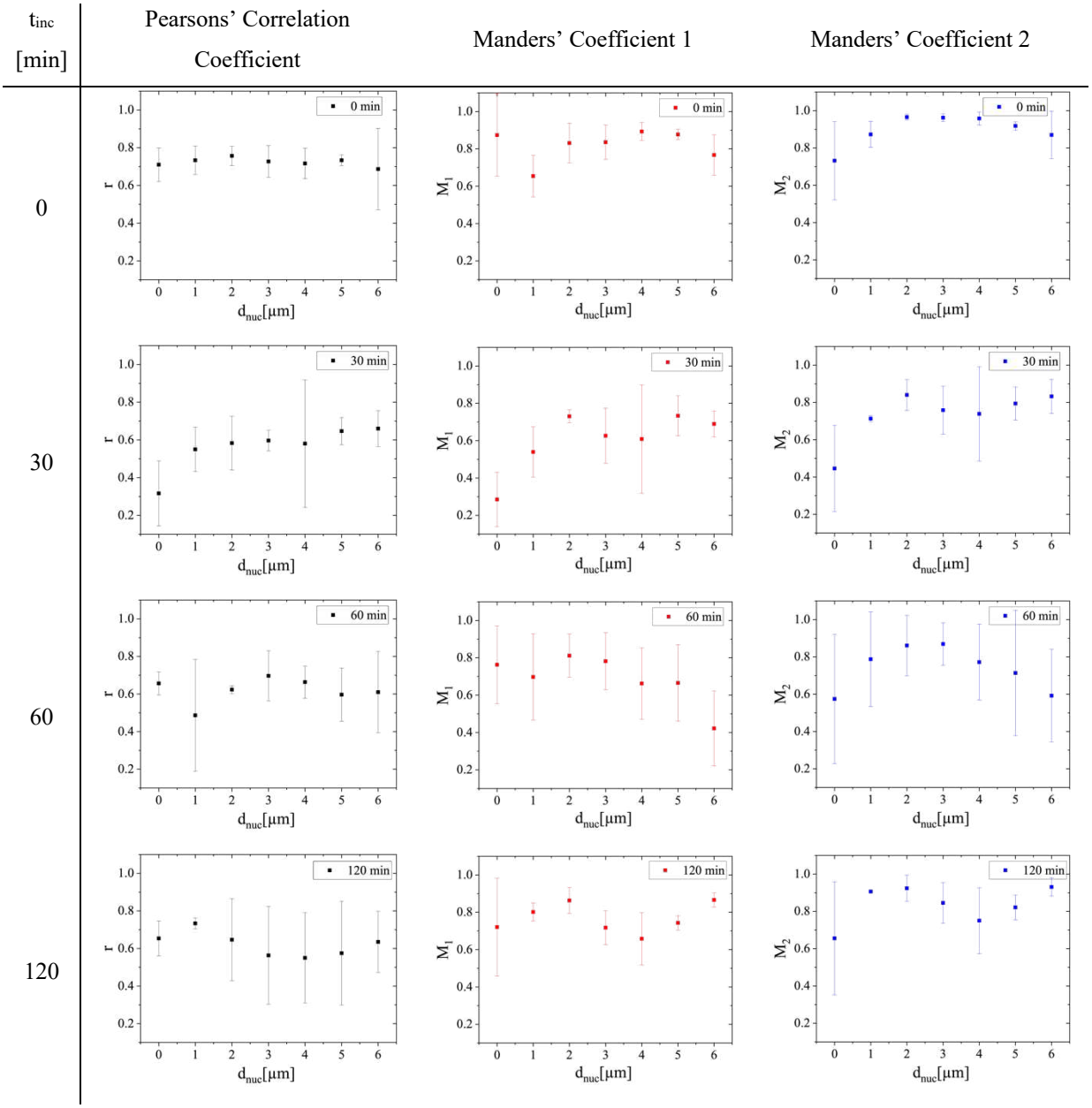

Figure A 10: Colocalization between Au and Gd as a function of distance to the nucleus d_{nuc} in 3T3 cells exposed to AuNP@CTPR-Gd (C_{Au} ~10 µg/mL) followed by different incubation times in NP-free medium (t_{inc} = 0, 30, 60, and 120 min).

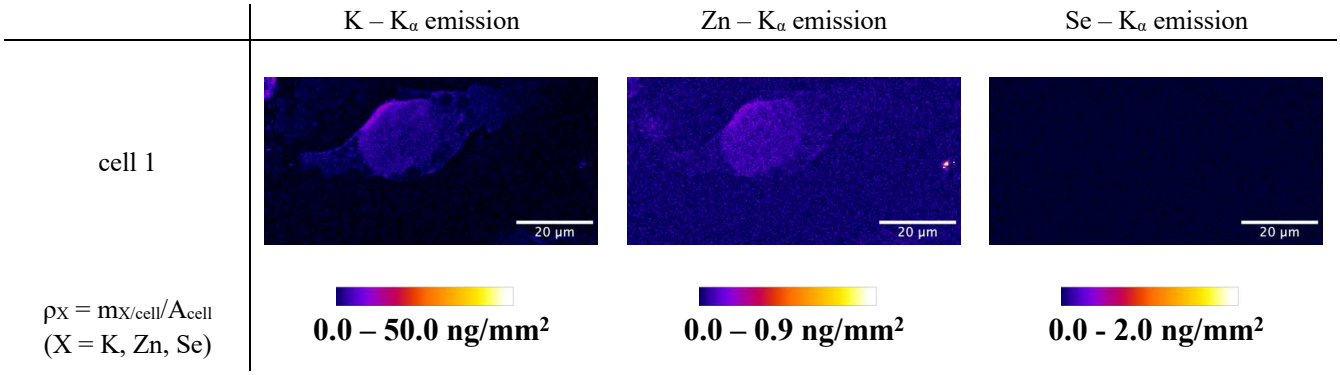

Figure A 11: XFI images after incubation of cells with biodegradable empty capsules.

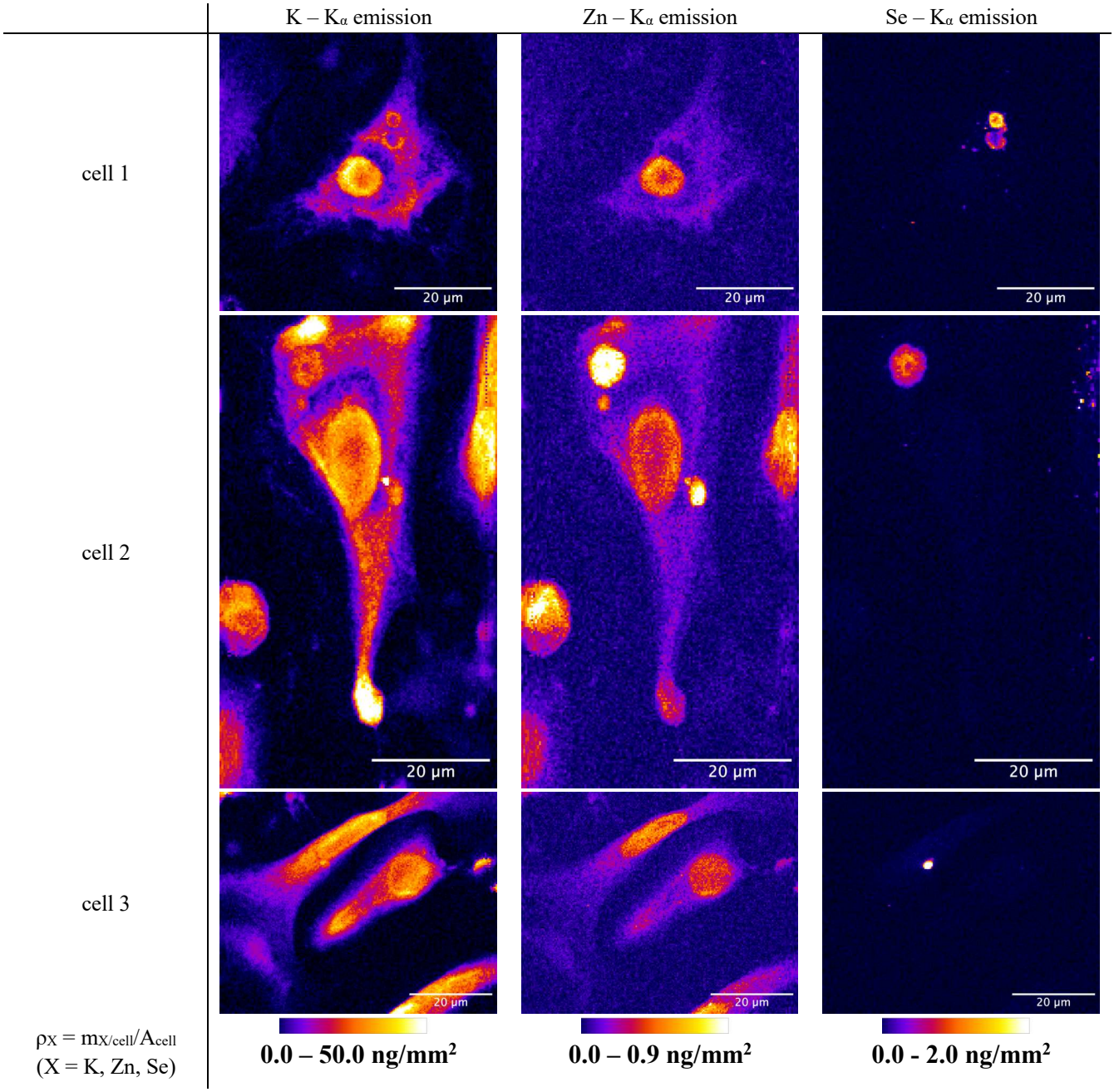

Figure A 12: XFI images after incubation of cells with nondegradable p-XSC-filled capsules.

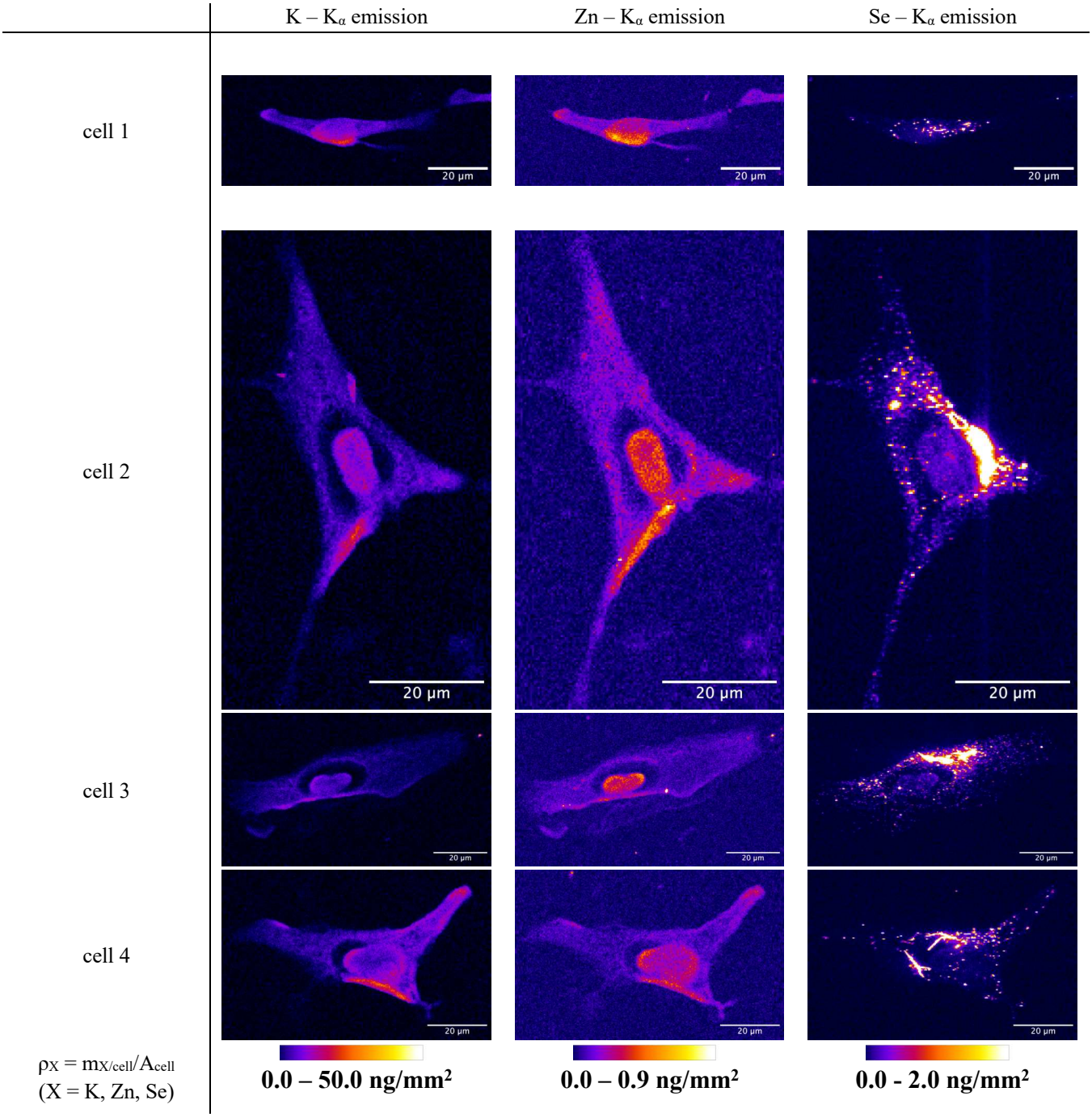

Figure A 13: XFI images after incubation of cells with biodegradable p-XSC-filled capsules.

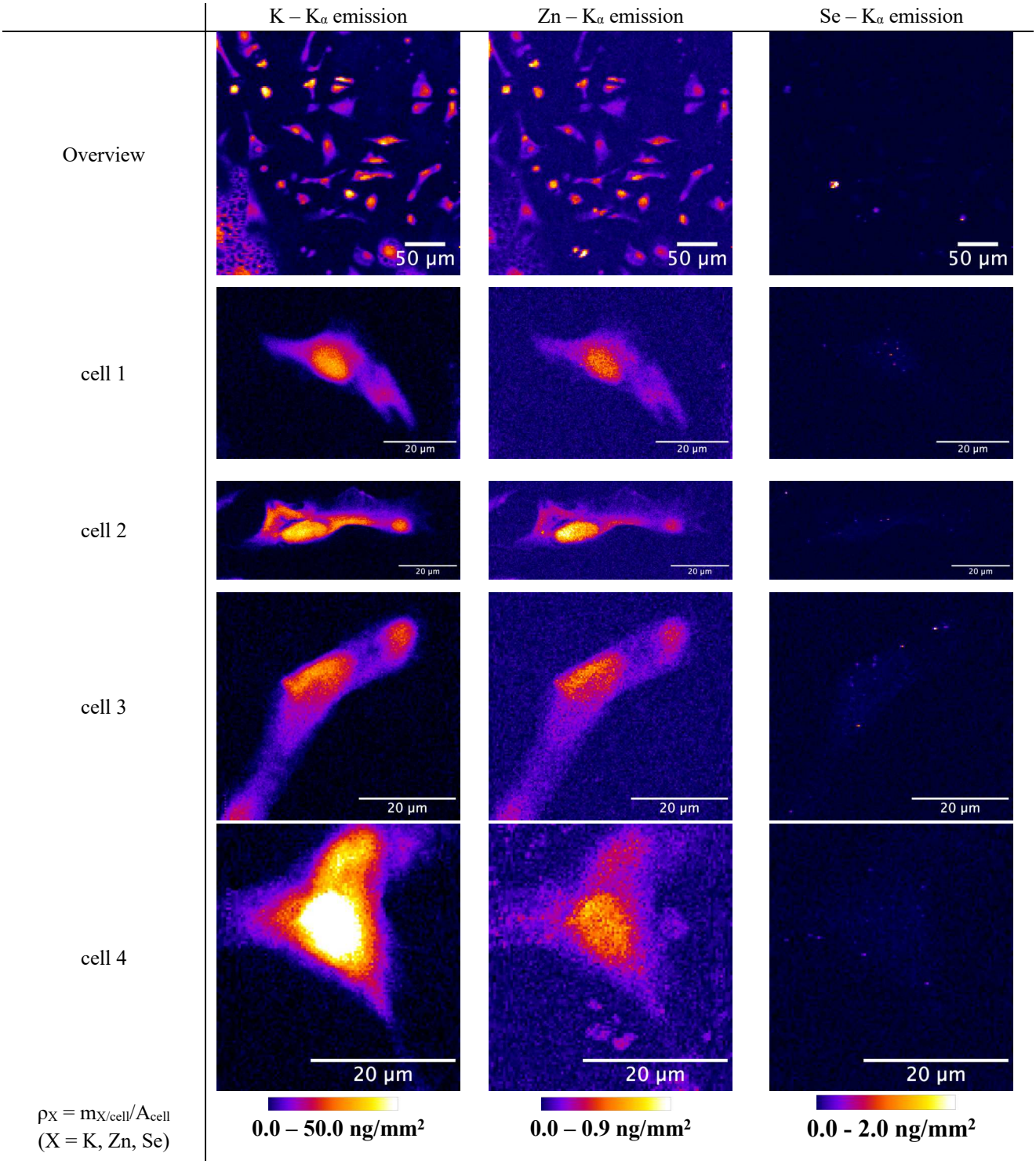

Figure A 14: XFI images after incubation of cells with free p-XSC.

5 References

(1) Simon, C. G.; Borgos, S. E.; Calzolai, L.; Nelson, B. C.; Parot, J.; Petersen, E. J.; Roesslein, M.; Xu, X.; Caputo, F. Orthogonal and Complementary Measurements of Properties of Drug Products Containing Nanomaterials. Journal of Controlled Release 2023, 354, 120–127. https://doi.org/10.1016/j.jconrel.2022.12.049.

(2) Vance, M. E.; Kuiken, T.; Vejerano, E. P.; McGinnis, S. P.; Hochella, M. F.; Hull, D. R. Nanotechnology in the Real World: Redeveloping the Nanomaterial Consumer Products Inventory. Beilstein Journal of Nanotechnology 2015, 6 (1), 1769–1780. https://doi.org/10.3762/bjnano.6.181.

(3) D'Mello, S. R.; Cruz, C. N.; Chen, M. L.; Kapoor, M.; Lee, S. L.; Tyner, K. M. The Evolving Landscape of Drug Products Containing Nanomaterials in the United States. Nat Nanotechnol 2017, 12 (6), 523–529. https://doi.org/10.1038/nnano.2017.67.

(4) Đorđević, S.; Gonzalez, M. M.; Conejos-Sánchez, I.; Carreira, B.; Pozzi, S.; Acúrcio, R. C.; Satchi-Fainaro, R.; Florindo, H. F.; Vicent, M. J. Current Hurdles to the Translation of Nanomedicines from Bench to the Clinic. Drug Delivery and Translational Research. Springer March 1, 2022, pp 500–525. https://doi.org/10.1007/s13346-021-01024-2.

(5) Anselmo, A. C.; Mitragotri, S. Nanoparticles in the Clinic: An Update. Bioeng Transl Med 2019, 4 (3). https://doi.org/10.1002/btm2.10143.

(6) Li, Y. Der; Chi, W. Y.; Su, J. H.; Ferrall, L.; Hung, C. F.; Wu, T. C. Coronavirus Vaccine Development: From SARS and MERS to COVID-19. Journal of Biomedical Science. BioMed Central Ltd December 1, 2020. https://doi.org/10.1186/s12929-020-00695-2.

(7) Zhang, G.; Tang, T.; Chen, Y.; Huang, X.; Liang, T. MRNA Vaccines in Disease Prevention and Treatment. Signal Transduction and Targeted Therapy. Springer Nature December 1, 2023. https://doi.org/10.1038/s41392-023-01579-1.

(8) Ruiz-Hitzky, E.; Darder, M.; Wicklein, B.; Ruiz-Garcia, C.; Martín-Sampedro, R.; del Real, G.; Aranda, P. Nanotechnology Responses to COVID-19. Advanced Healthcare Materials. Wiley-VCH Verlag October 1, 2020. https://doi.org/10.1002/adhm.202000979.

(9) Barenholz, Y. Doxil® - The First FDA-Approved Nano-Drug: Lessons Learned. Journal of Controlled Release. June 10, 2012, pp 117–134. https://doi.org/10.1016/j.jconrel.2012.03.020.

(10) Wang, Y.-X. J. Superparamagnetic Iron Oxide Based MRI Contrast Agents: Current Status of Clinical Application. Quant Imaging Med Surg 2011, 1 (1), 35–40. https://doi.org/10.3978/j.issn.2223-4292.2011.08.03.

(11) Matsumura, Y.; Maeda, H. A New Concept for Macromolecular Therapeutics in Cancer Chemotherapy: Mechanism of Tumoritropic Accumulation of Proteins and the Antitumor Agent Smancs. Cancer Res 1986, 46, 6387–6392.

(12) Prabhakar, U.; Maeda, H.; K. Jain, R.; Sevick-Muraca, E. M.; Zamboni, W.; Farokhzad, O. C.; Barry, S. T.; Gabizon, A.; Grodzinski, P.; Blakey, D. C. Challenges and Key Considerations of the Enhanced Permeability and Retention Effect for Nanomedicine Drug Delivery in Oncology. In Cancer Research; 2013; Vol. 73, pp 2412–2417. https://doi.org/10.1158/0008-5472.CAN-12-4561.

(13) Nguyen, L. N. M.; Ngo, W.; Lin, Z. P.; Sindhwani, S.; MacMillan, P.; Mladjenovic, S. M.; Chan, W. C. W. The Mechanisms of Nanoparticle Delivery to Solid Tumours. Nature Reviews Bioengineering 2024, 2 (3), 201–213. https://doi.org/10.1038/s44222-024-00154-9.

(14) Nguyen, L. N. M.; Lin, Z. P.; Sindhwani, S.; MacMillan, P.; Mladjenovic, S. M.; Stordy, B.; Ngo, W.; Chan, W. C. W. The Exit of Nanoparticles from Solid Tumours. Nat Mater 2023, 22 (10), 1261–1272. https://doi.org/10.1038/s41563-023-01630-0.

(15) Wilhelm, S.; Tavares, A. J.; Dai, Q.; Ohta, S.; Audet, J.; Dvorak, H. F.; Chan, W. C. W. Analysis of Nanoparticle Delivery to Tumours. Nat Rev Mater 2016, 1 (5), 1–12.

(16) Cheng, Y. H.; He, C.; Riviere, J. E.; Monteiro-Riviere, N. A.; Lin, Z. Meta-Analysis of Nanoparticle Delivery to Tumors Using a Physiologically Based Pharmacokinetic Modeling and Simulation Approach. ACS Nano 2020, 14 (3), 3075–3095. https://doi.org/10.1021/acsnano.9b08142.

(17) Jain, R. K.; Stylianopoulos, T. Delivering Nanomedicine to Solid Tumors. Nature Reviews Clinical Oncology. November 2010, pp 653–664. https://doi.org/10.1038/nrclinonc.2010.139.

(18) Hirn, S.; Semmler-Behnke, M.; Schleh, C.; Wenk, A.; Lipka, J.; Schäffler, M.; Takenaka, S.; Möller, W.; Schmid, G.; Simon, U.; Kreyling, W. G. Particle Size-Dependent and Surface Charge-Dependent Biodistribution of Gold Nanoparticles after Intravenous Administration. European Journal of Pharmaceutics and Biopharmaceutics 2011, 77 (3), 407–416. https://doi.org/10.1016/j.ejpb.2010.12.029.

(19) Arnida; Janát-Amsbury, M. M.; Ray, A.; Peterson, C. M.; Ghandehari, H. Geometry and Surface Characteristics of Gold Nanoparticles Influence Their Biodistribution and Uptake by Macrophages. European Journal of Pharmaceutics and Biopharmaceutics 2011, 77 (3), 417–423. https://doi.org/10.1016/j.ejpb.2010.11.010.

(20) Elci, S. G.; Jiang, Y.; Yan, B.; Kim, S. T.; Saha, K.; Moyano, D. F.; Yesilbag Tonga, G.; Jackson, L. C.; Rotello, V. M.; Vachet, R. W. Surface Charge Controls the Suborgan Biodistributions of Gold Nanoparticles. ACS Nano 2016, 10 (5), 5536–5542. https://doi.org/10.1021/acsnano.6b02086.

(21) Ouyang, B.; Poon, W.; Zhang, Y. N.; Lin, Z. P.; Kingston, B. R.; Tavares, A. J.; Zhang, Y.; Chen, J.; Valic, M. S.; Syed, A. M.; MacMillan, P.; Couture-Senécal, J.; Zheng, G.; Chan, W. C. W. The Dose Threshold for Nanoparticle Tumour Delivery. Nat Mater 2020, 19 (12), 1362–1371. https://doi.org/10.1038/s41563-020-0755-z.

(22) Yi, Y.; Kim, H. J.; Zheng, M.; Mi, P.; Naito, M.; Kim, B. S.; Min, H. S.; Hayashi, K.; Perche, F.; Toh, K.; Liu, X.; Mochida, Y.; Kinoh, H.; Cabral, H.; Miyata, K.; Kataoka, K. Glucose-Linked Sub-50-Nm Unimer Polyion Complex-Assembled Gold Nanoparticles for Targeted SiRNA Delivery to Glucose Transporter 1-Overexpressing Breast Cancer Stem-like Cells. Journal of Controlled Release 2019, 295, 268–277. https://doi.org/10.1016/j.jconrel.2019.01.006.

(23) Ahmad, A.; Khan, F.; Mishra, R. K.; Khan, R. Precision Cancer Nanotherapy: Evolving Role of Multifunctional Nanoparticles for Cancer Active Targeting. Journal of Medicinal Chemistry. American Chemical Society December 12, 2019, pp 10475–10496. https://doi.org/10.1021/acs.jmedchem.9b00511.

(24) Pant, K.; Neuber, C.; Zarschler, K.; Wodtke, J.; Meister, S.; Haag, R.; Pietzsch, J.; Stephan, H. Active Targeting of Dendritic Polyglycerols for Diagnostic Cancer Imaging. Small 2020, 16 (7). https://doi.org/10.1002/smll.201905013.

(25) Bhattacharyya, S.; Singh, R. D.; Pagano, R.; Robertson, J. D.; Bhattacharya, R.; Mukherjee, P. Switching the Targeting Pathways of a Therapeutic Antibody by Nanodesign. Angewandte Chemie - International Edition 2012, 51 (7), 1563–1567. https://doi.org/10.1002/anie.201105432.

(26) Deng, Z. J.; Liang, M.; Monteiro, M.; Toth, I.; Minchin, R. F. Nanoparticle-Induced Unfolding of Fibrinogen Promotes Mac-1 Receptor Activation and Inflammation. Nat Nanotechnol 2011, 6 (1), 39–44. https://doi.org/10.1038/nnano.2010.250.

(27) Teichroeb, J. H.; Forrest, J. A.; Jones, L. W. Size-Dependent Denaturing Kinetics of Bovine Serum Albumin Adsorbed onto Gold Nanospheres. European Physical Journal E 2008, 26 (4), 411–415. https://doi.org/10.1140/epje/i2007-10342-9.

(28) Monopoli, M. P.; Bombelli, F. B.; Dawson, K. A. Nanoparticle Coronas Take Shape. Nat Nanotechnol 2011, 6 (1), 11–12. https://doi.org/10.1038/nnano.2010.267.

(29) Monopoli, M. P.; Åberg, C.; Salvati, A.; Dawson, K. A. Biomolecular Coronas Provide the Biological Identity of Nanosized Materials. Nat Nanotechnol 2012, 7 (12), 779–786. https://doi.org/10.1038/nnano.2012.207.

(30) Caracciolo, G.; Farokhzad, O. C.; Mahmoudi, M. Biological Identity of Nanoparticles In Vivo: Clinical Implications of the Protein Corona. Trends in Biotechnology. Elsevier Ltd March 1, 2017, pp 257–264. https://doi.org/10.1016/j.tibtech.2016.08.011.

(31) Dawson, K. A.; Yan, Y. Current Understanding of Biological Identity at the Nanoscale and Future Prospects. Nat Nanotechnol 2021, 16 (3), 229–242. https://doi.org/10.1038/s41565-021-00860-0.

(32) Mahmoudi, M.; Bertrand, N.; Zope, H.; Farokhzad, O. C. Emerging Understanding of the Protein Corona at the Nano-Bio Interfaces. Nano Today 2016, 11 (6), 817–832. https://doi.org/10.1016/j.nantod.2016.10.005.

(33) Walkey, C. D.; Chan, W. C. W. Understanding and Controlling the Interaction of Nanomaterials with Proteins in a Physiological Environment. Chem Soc Rev 2012, 41 (7), 2780–2799. https://doi.org/10.1039/c1cs15233e.

(34) Braun, N. J.; Debrosse, M. C.; Hussain, S. M.; Comfort, K. K. Modification of the Protein Corona-Nanoparticle Complex by Physiological Factors. Materials Science and Engineering C 2016, 64, 34–42. https://doi.org/10.1016/j.msec.2016.03.059.

(35) Matczuk, M.; Legat, J.; Shtykov, S. N.; Jarosz, M.; Timerbaev, A. R. Characterization of the Protein Corona of Gold Nanoparticles by an Advanced Treatment of CE-ICP-MS Data. Electrophoresis 2016, 37 (15–16), 2257–2259. https://doi.org/10.1002/elps.201600152.

(36) Blume, J. E.; Manning, W. C.; Troiano, G.; Hornburg, D.; Figa, M.; Hesterberg, L.; Platt, T. L.; Zhao, X.; Cuaresma, R. A.; Everley, P. A.; Ko, M.; Liou, H.; Mahoney, M.; Ferdosi, S.; Elgierari, E. M.; Stolarczyk, C.; Tangeysh, B.; Xia, H.; Benz, R.; Siddiqui, A.; Carr, S. A.; Ma, P.; Langer, R.; Farias, V.; Farokhzad, O. C. Rapid, Deep and Precise Profiling of the Plasma Proteome with Multi-Nanoparticle Protein Corona. Nat Commun 2020, 11 (1). https://doi.org/10.1038/s41467-020-17033-7.

(37) Shang, L.; Nienhaus, G. U. In Situ Characterization of Protein Adsorption onto Nanoparticles by Fluorescence Correlation Spectroscopy. Acc Chem Res 2017, 50 (2), 387–395. https://doi.org/10.1021/acs.accounts.6b00579.

(38) Martinez-Moro, M.; Di Silvio, D.; Moya, S. E. Fluorescence Correlation Spectroscopy as a Tool for the Study of the Intracellular Dynamics and Biological Fate of Protein Corona. Biophys Chem 2019, 253. https://doi.org/10.1016/j.bpc.2019.106218.

(39) Casals, E.; Pfaller, T.; Duschl, A.; Oostingh, G. J.; Puntes, V. Time Evolution of the Nanoparticle Protein Corona. ACS Nano 2010, 4 (7), 3623–3632. https://doi.org/10.1021/nn901372t.

(40) Palchetti, S.; Pozzi, D.; Capriotti, A. L.; Barbera, G. La; Chiozzi, R. Z.; Digiacomo, L.; Peruzzi, G.; Caracciolo, G.; Laganà, A. Influence of Dynamic Flow Environment on Nanoparticle-Protein Corona: From Protein Patterns to Uptake in Cancer Cells. Colloids Surf B Biointerfaces 2017, 153, 263–271. https://doi.org/10.1016/j.colsurfb.2017.02.037.

(41) Rahman, M.; Laurent, S.; Tawil, N.; Yahia, L.; Mahmoudi, M. Nanoparticle and Protein Corona BT - Protein-Nanoparticle Interactions: The Bio-Nano Interface; Rahman, M., Laurent, S., Tawil, N., Yahia, L., Mahmoudi, M., Eds.; Springer Berlin Heidelberg: Berlin, Heidelberg, 2013; pp 21–44. https://doi.org/10.1007/978-3-642-37555-2_2.

(42) Stepien, G.; Moros, M.; Pérez-Hernández, M.; Monge, M.; Gutiérrez, L.; Fratila, R. M.; Las Heras, M. De; Menao Guillén, S.; Puente Lanzarote, J. J.; Solans, C.; Pardo, J.; De La Fuente, J. M. Effect of Surface Chemistry and Associated Protein Corona on the Long-Term Biodegradation of Iron Oxide Nanoparticles in Vivo. ACS Appl Mater Interfaces 2018, 10 (5), 4548–4560. https://doi.org/10.1021/acsami.7b18648.

(43) Ilinskaya, A. N.; Dobrovolskaia, M. A. Interaction Between Nanoparticles and Plasma Proteins: Effects on Nanoparticle Biodistribution and Toxicity. In Polymer Nanoparticles for Nanomedicines: A Guide for their Design, Preparation and Development; Vauthier, C., Ponchel, G., Eds.; Springer International Publishing: Cham, 2016; pp 505–520. https://doi.org/10.1007/978-3-319-41421-8_15.

(44) Walkey, C. D.; Olsen, J. B.; Song, F.; Liu, R.; Guo, H.; Olsen, D. W. H.; Cohen, Y.; Emili, A.; Chan, W. C. W. Protein Corona Fingerprinting Predicts the Cellular Interaction of Gold and Silver Nanoparticles. ACS Nano 2014, 8 (3), 2439–2455. https://doi.org/10.1021/nn406018q.

(45) Müller, R. H.; Gohla, S.; Keck, C. M. State of the Art of Nanocrystals – Special Features, Production, Nanotoxicology Aspects and Intracellular Delivery. European Journal of Pharmaceutics and Biopharmaceutics 2011, 78 (1), 1–9. https://doi.org/https://doi.org/10.1016/j.ejpb.2011.01.007.

(46) Dominguez-Medina, S.; Blankenburg, J.; Olson, J.; Landes, C. F.; Link, S. Adsorption of a Protein Monolayer via Hydrophobic Interactions Prevents Nanoparticle Aggregation under Harsh Environmental Conditions. ACS Sustain Chem Eng 2013, 1 (7), 833–842. https://doi.org/10.1021/sc400042h.

(47) Dal Magro, R.; Albertini, B.; Beretta, S.; Rigolio, R.; Donzelli, E.; Chiorazzi, A.; Ricci, M.; Blasi, P.; Sancini, G. Artificial Apolipoprotein Corona Enables Nanoparticle Brain Targeting. Nanomedicine 2018, 14 (2), 429–438. https://doi.org/https://doi.org/10.1016/j.nano.2017.11.008.

(48) Guo, J.; O'Driscoll, C. M.; Holmes, J. D.; Rahme, K. Bioconjugated Gold Nanoparticles Enhance Cellular Uptake: A Proof of Concept Study for SiRNA Delivery in Prostate Cancer Cells. Int J Pharm 2016, 509 (1), 16–27. https://doi.org/https://doi.org/10.1016/j.ijpharm.2016.05.027.

(49) Moghimi, S. M.; Szebeni, J. Stealth Liposomes and Long Circulating Nanoparticles: Critical Issues in Pharmacokinetics, Opsonization and Protein-Binding Properties. Prog Lipid Res 2003, 42 (6), 463–478. https://doi.org/https://doi.org/10.1016/S0163-7827(03)00033-X.

(50) Böhmert, L.; Voß, L.; Stock, V.; Braeuning, A.; Lampen, A.; Sieg, H. Isolation Methods for Particle Protein Corona Complexes from Protein-Rich Matrices. Nanoscale Advances. Royal Society of Chemistry February 1, 2020, pp 563–582. https://doi.org/10.1039/c9na00537d.

(51) Balmori, A.; Sandu, R.; Gheorghe, D.; Botea-Petcu, A.; Precupas, A.; Tanasescu, S.; Sánchez-García, D.; Borrós, S. Revising Protein Corona Characterization and Combining ITC and Nano-DSC to Understand the Interaction of Proteins With Porous Nanoparticles. Front Bioeng Biotechnol 2021, 9. https://doi.org/10.3389/fbioe.2021.650281.

(52) Tanand, X.; Welsher, K. Particle-by-Particle In Situ Characterization of the Protein Coronavia Real-Time 3D Single-Particle-Tracking Spectroscopy**. https://doi.org/10.26434/chemrxiv.13521332.v1.

(53) Dolci, M.; Wang, Y.; Nooteboom, S. W.; Soto Rodriguez, P. E. D.; Sánchez, S.; Albertazzi, L.; Zijlstra, P. Real-Time Optical Tracking of Protein Corona Formation on Single Nanoparticles in Serum. ACS Nano 2023. https://doi.org/10.1021/acsnano.3c05872.

(54) Otto, F.; Sun, X.; Schulz, F.; Sanchez-cano, C.; Feliu, N.; Westermeier, F.; Parak, W. J. X-Ray Photon Correlation Spectroscopy Towards Measuring Nanoparticle Diameters in Biological Environments Allowing for the In Situ Analysis of Their Bio-Nano Interface. 2022, 2201324, 1–10. https://doi.org/10.1002/smll.202201324.

(55) Carril, M.; Padro, D.; Del Pino, P.; Carrillo-Carrion, C.; Gallego, M.; Parak, W. J. In Situ Detection of the Protein Corona in Complex Environments. Nat Commun 2017, 8 (1). https://doi.org/10.1038/s41467-017-01826-4.

(56) Padro, D.; Cienskowski, P.; Lopez-Fernandez, S.; Chakraborty, I.; Carrillo-Carrion, C.; Feliu, N.; Parak, W. J.; Carril, M. Toward Diffusion Measurements of Colloidal Nanoparticles in Biological Environments by Nuclear Magnetic Resonance. Small 2020, 16 (36). https://doi.org/10.1002/smll.202001160.

(57) Arango, J. M.; Padro, D.; Blanco, J.; Lopez-Fernandez, S.; Castellnou, P.; Villa-Valverde, P.; Ruiz-Cabello, J.; Martin, A.; Carril, M. Fluorine Labeling of Nanoparticles and in Vivo 19F Magnetic Resonance Imaging. ACS Appl Mater Interfaces 2021, 13 (11), 12941–12949. https://doi.org/10.1021/acsami.1c01291.

(58) Iranpour Anaraki, N.; Liebi, M.; Ong, Q.; Blanchet, C.; Maurya, A. K.; Stellacci, F.; Salentinig, S.; Wick, P.; Neels, A. In-Situ Investigations on Gold Nanoparticles Stabilization Mechanisms in Biological Environments Containing HSA. Adv Funct Mater 2022, 32 (9). https://doi.org/10.1002/adfm.202110253.

(59) Bertoli, F.; Garry, D.; Monopoli, M. P.; Salvati, A.; Dawson, K. A. The Intracellular Destiny of the Protein Corona: A Study on Its Cellular Internalization and Evolution. ACS Nano 2016, 10 (11), 10471–10479. https://doi.org/10.1021/acsnano.6b06411.

(60) Carrillo-Carrion, C.; Bocanegra, A. I.; Arnaiz, B.; Feliu, N.; Zhu, D.; Parak, W. J. Triple-Labeling of Polymer-Coated Quantum Dots and Adsorbed Proteins for Tracing Their Fate in Cell Cultures. ACS Nano 2019, 13 (4), 4631–4639. https://doi.org/10.1021/acsnano.9b00728.

(61) Han, S.; da Costa Marques, R.; Simon, J.; Kaltbeitzel, A.; Koynov, K.; Landfester, K.; Mailänder, V.; Lieberwirth, I. Endosomal Sorting Results in a Selective Separation of the

Protein Corona from Nanoparticles. Nat Commun 2023, 14 (1), 295. https://doi.org/10.1038/s41467-023-35902-9.

(62) Tao, X.; Chang, X.; Wan, X.; Guo, Y.; Zhang, Y.; Liao, Z.; Song, Y.; Song, E. Impact of Protein Corona on Noncovalent Molecule-Gold Nanoparticle-Based Sensing. Anal Chem 2020, 92 (22), 14990–14998. https://doi.org/10.1021/acs.analchem.0c02850.

(63) Ash, C.; Dubec, M.; Donne, K.; Bashford, T. Effect of Wavelength and Beam Width on Penetration in Light-Tissue Interaction Using Computational Methods. Lasers Med Sci 2017, 32 (8), 1909–1918. https://doi.org/10.1007/s10103-017-2317-4.

(64) Sanchez-cano, C.; Alvarez-puebla, R. A.; Abendroth, J. M.; Beck, T.; Blick, R.; Cao, Y.; Caruso, F.; Chakraborty, I.; Chapman, H. N.; Chen, C.; Cohen, B. E.; Cormode, D. P.; Cui, D.; Dawson, K. A.; Falkenberg, G.; Conceic, A. L. C.; Fan, C.; Feliu, N.; Gao, M.; Gargioni, E.; Glu, C.; Gru, F.; Hassan, M.; Hu, Y.; Huang, Y.; Huber, S.; Huse, N.; Kang, Y.; Khademhosseini, A.; Keller, T. F.; Ko, C.; Kotov, N. A.; Koziej, D.; Liang, X.; Liu, B.; Ma, X.; Machicote, A.; Maison, W.; Liu, S.; Liu, Y.; Liu, Z.; Liz-marza, L. M.; Mancuso, A. P.; Megahed, S.; Nickel, B.; Otto, F.; Palencia, C.; Pascarelli, S.; Richardson, J. J.; Rosenhahn, A.; Pearson, A.; Pen, O.; Qi, B.; Ra, J.; Rothkamm, K.; Ru, M.; Sanyal, M. K.; Schaak, R. E.; Schlemmer, H.; Schmidt, M.; Schmutzler, O.; Schotten, T.; Schulz, F.; Sood, A. K.; Spiers, K. M.; Staufer, T.; Stemer, D. M.; Stierle, A.; Sun, X.; Tsakanova, G.; Weiss, P. S.; Weller, H.; Westermeier, F.; Xu, M.; Yan, H.; Zeng, Y.; Zhao, Y.; Zhao, Y. X - Ray-Based Techniques to Study the Nano − Bio Interface. ACS Nano 2021, 15 (3), 3754–3807. https://doi.org/10.1021/acsnano.0c09563.

(65) Niclis, J. C.; Murphy, S. V; Parkinson, D. Y.; Zedan, A.; Sathananthan, A. H.; Cram, D. S.; Heraud, P. Three-Dimensional Imaging of Human Stem Cells Using Soft X-Ray Tomography. J R Soc Interface 2015, 12 (108), 20150252. https://doi.org/10.1098/rsif.2015.0252.

(66) Conesa, J. J.; Otón, J.; Chiappi, M.; Carazo, J. M.; Pereiro, E.; Chichón, F. J.; Carrascosa, J. L. Intracellular Nanoparticles Mass Quantification by Near-Edge Absorption Soft X-Ray Nanotomography. Sci Rep 2016, 6 (1), 22354. https://doi.org/10.1038/srep22354.

(67) Lin, Z.; Zhang, X.; Nandi, P.; Lin, Y.; Wang, L.; Chu, Y. S.; Paape, T.; Yang, Y.; Xiao, X.; Liu, Q. Correlative Single-Cell Hard X-Ray Computed Tomography and X-Ray Fluorescence Imaging. Commun Biol 2024, 7 (1), 280. https://doi.org/10.1038/s42003-024-05950-y.

(68) Langer, M.; Peyrin, F. 3D X-Ray Ultra-Microscopy of Bone Tissue. Osteoporosis International 2016, 27 (2), 441–455. https://doi.org/10.1007/s00198-015-3257-0.

(69) Li, T.; Dresselhaus, J. L.; Ivanov, N.; Prasciolu, M.; Fleckenstein, H.; Yefanov, O.; Zhang, W.; Pennicard, D.; Dippel, A.-C.; Gutowski, O.; Villanueva-Perez, P.; Chapman, H. N.; Bajt, S. Dose-Efficient Scanning Compton X-Ray Microscopy. Light Sci Appl 2023, 12 (1), 130. https://doi.org/10.1038/s41377-023-01176-5.

(70) Villanueva-Perez, P.; Bajt, S.; Chapman, H. N. Dose Efficient Compton X-Ray Microscopy. Optica 2018, 5 (4), 450–457. https://doi.org/10.1364/OPTICA.5.000450.

(71) Luo, Y.; Paunesku, T.; Antipova, O.; Liu, Y.; Zaluzec, N. J.; Di, Z.; Woloschak, G.; Chen, S. A Reliable Workflow for Improving Nanoscale X-Ray Fluorescence Tomographic Analysis on Nanoparticle-Treated HeLa Cells. Metallomics 2022, 14 (9), mfac025. https://doi.org/10.1093/mtomcs/mfac025.

(72) Shaker, K.; Vogt, C.; Katsu-Jiménez, Y.; Kuiper, R. V; Andersson, K.; Li, Y.; Larsson, J. C.; Rodriguez-Garcia, A.; Toprak, M. S.; Arsenian-Henriksson, M.; Hertz, H. M. Longitudinal In-Vivo X-Ray Fluorescence Computed Tomography With Molybdenum Nanoparticles. IEEE Trans Med Imaging 2020, 39 (12), 3910–3919. https://doi.org/10.1109/TMI.2020.3007165.

(73) Sanchez-Cano, C.; Romero-Canelón, I.; Yang, Y.; Hands-Portman, I. J.; Bohic, S.; Cloetens, P.; Sadler, P. J. Synchrotron X-Ray Fluorescence Nanoprobe Reveals Target Sites for Organo-Osmium Complex in Human Ovarian Cancer Cells. Chemistry - A European Journal 2017, 23 (11), 2512–2516. https://doi.org/10.1002/chem.201605911.

(74) Gollwitzer, C.; Bartczak, D.; Goenaga-Infante, H.; Kestens, V.; Krumrey, M.; Minelli, C.; Pálmai, M.; Ramaye, Y.; Roebben, G.; Sikora, A.; Varga, Z. A Comparison of Techniques for Size Measurement of Nanoparticles in Cell Culture Medium. Analytical Methods 2016, 8 (26), 5272–5282. https://doi.org/10.1039/C6AY00419A.

(75) Otto, F.; Dallari, F.; Westermeier, F.; Wieland, D. C. F.; Parak, W. J.; Lehmkühler, F.; Schulz, F. The Dynamics of PEG-Coated Nanoparticles in Concentrated Protein Solutions up to the Molecular Crowding Range. Aggregate 2024, 5 (3), e483. https://doi.org/https://doi.org/10.1002/agt2.483.

(76) Wang, L.; Zhang, T.; Li, P.; Huang, W.; Tang, J.; Wang, P.; Liu, J.; Yuan, Q.; Bai, R.; Li, B.; Zhang, K.; Zhao, Y.; Chen, C. Use of Synchrotron Radiation-Analytical Techniques To Reveal Chemical Origin of Silver-Nanoparticle Cytotoxicity. ACS Nano 2015, 9 (6), 6532–6547. https://doi.org/10.1021/acsnano.5b02483.

(77) Röntgen, C. W. On a New Kind of Rays. Nature 1896, 53 (1369), 274. https://doi.org/10.1038/053274a0.

(78) Dössel, O. Bildgebende Verfahren in Der Medizin.

(79) Thwaites, D. I.; Tuohy, J. B. Back to the Future: The History and Development of the Clinical Linear Accelerator. Phys Med Biol 2006, 51 (13). https://doi.org/10.1088/0031-9155/51/13/R20.

(80) Bahrdt, J. Shaping Photon Beams with Undulators and Wigglers. In Synchrotron Light Sources and Free-Electron Lasers: Accelerator Physics, Instrumentation and Science Applications; Jaeschke, E., Khan, S., Schneider, J. R., Hastings, J. B., Eds.; Springer International Publishing: Cham, 2019; pp 1–84. https://doi.org/10.1007/978-3-319-04507-8_16-3.

(81) Mobilio, S.; Boscherini, F.; Meneghini, C. Synchrotron Radiation; Springer Science and Business Media Deutschland GmbH, 2015. https://doi.org/10.5059/yukigoseikyokaishi.54.384.

(82) Willmott, P. An Introduction to Synchrotron Radiation, 2nd ed.; Wiley, 2019.

(83) Kirkpatrick, P.; Baez, A. V. Formation of Optical Images by X-Rays. J. Opt. Soc. Am. 1948, 38 (9), 766–774. https://doi.org/10.1364/JOSA.38.000766.

(84) Matsuyama, S.; Mimura, H.; Yumoto, H.; Hara, H.; Yamamura, K.; Sano, Y.; Endo, K.; Mori, Y.; Yabashi, M.; Nishino, Y.; Tamasaku, K.; Ishikawa, T.; Yamauchi, K. Development of Mirror Manipulator for Hard-x-Ray Nanofocusing at Sub-50-Nm Level. Review of Scientific Instruments 2006, 77 (9). https://doi.org/10.1063/1.2349594.

(85) Yano, J.; Yachandra, V. K. X-Ray Absorption Spectroscopy. Photosynth Res 2009, 102 (2), 241–254. https://doi.org/10.1007/s11120-009-9473-8.

(86) Wang, M.; Árnadóttir, L.; Xu, Z. J.; Feng, Z. In Situ X-Ray Absorption Spectroscopy Studies of Nanoscale Electrocatalysts. Nanomicro Lett 2019, 11 (1), 47. https://doi.org/10.1007/s40820-019-0277-x.

(87) National Institute of Standards and Technology. X-Ray Form Factor, Attenuation, and Scattering Tables Main Page. https://physics.nist.gov/PhysRefData/FFast/html/form.html.

(88) van Bokhoven, J. A.; Lamberti, C. X-Ray Absorption and X-Ray Emission Spectroscopy: Theory and Applications; X-ray Absorption and X-ray Emission Spectroscopy: Theory and Applications; Wiley, 2016.

(89) HEVESY, G.; LAY, H. Fluorescent Yield of X-Ray Emission. Nature 1934, 134 (3377), 98–99. https://doi.org/10.1038/134098b0.

(90) BAMBYNEK, W.; CRASEMANN, B.; FINK, R. W.; FREUND, H.-U.; MARK, H.; SWIFT, C. D.; PRICE, R. E.; RAO, P. V. X-Ray Fluorescence Yields, Auger, and Coster-Kronig Transition Probabilities. Rev Mod Phys 1972, 44 (4), 716–813. https://doi.org/10.1103/RevModPhys.44.716.

(91) Brunetti, A.; Sanchez del Rio, M.; Golosio, B.; Simionovici, A.; Somogyi, A. A Library for X-Ray–Matter Interaction Cross Sections for X-Ray Fluorescence Applications. Spectrochim Acta Part B At Spectrosc 2004, 59 (10), 1725–1731. https://doi.org/https://doi.org/10.1016/j.sab.2004.03.014.

(92) Beckhoff, B.; Kanngießer, B.; Langhoff, N.; Wedell, R.; Wolff, H. Handbook of Practical X-Ray Fluorescence Analysis; Springer Science and Business Media Deutschland GmbH, 2006.

(93) Jenkins, R.; Manne, R.; Robin, R.; Senemaud, C. IUPAC—Nomenclature System for x-Ray Spectroscopy. X-Ray Spectrometry 1991, 20 (3), 149–155. https://doi.org/https://doi.org/10.1002/xrs.1300200308.

(94) Knoll, G. F. Radiation Detection and Measurement; Wiley, 2010.

(95) Pushie, M. J.; Pickering, I. J.; Korbas, M.; Hackett, M. J.; George, G. N. Elemental and Chemically Specific X-Ray Fluorescence Imaging of Biological Systems. Chem Rev 2014, 114 (17), 8499–8541. https://doi.org/10.1021/cr4007297.

(96) Villar, F.; Andre, L.; Baker, R.; Bohic, S.; da Silva, J. C.; Guilloud, C.; Hignette, O.; Meyer, J.; Pacureanu, A.; Perez, M.; Salome, M.; van der Linden, P.; Yang, Y.; Cloetens, P. Nanopositioning for the ESRF ID16A Nano-Imaging Beamline. Synchrotron Radiat News 2018, 31 (5), 9–14. https://doi.org/10.1080/08940886.2018.1506234.

(97) Solé, V. A.; Papillon, E.; Cotte, M.; Walter, P.; Susini, J. A Multiplatform Code for the Analysis of Energy-Dispersive X-Ray Fluorescence Spectra. Spectrochim Acta Part B At Spectrosc 2007, 62 (1), 63–68. https://doi.org/10.1016/j.sab.2006.12.002.

(98) BEARDEN, J. A. X-Ray Wavelengths. Rev Mod Phys 1967, 39 (1), 78–124. https://doi.org/10.1103/RevModPhys.39.78.

(99) Krause, M. O.; Oliver, J. H. Natural Widths of Atomic K and L Levels, Kα X-ray Lines and Several KLL Auger Lines. J Phys Chem Ref Data 1979, 8 (2), 329–338. https://doi.org/10.1063/1.555595.

(100) Broll, N. Quantitative X-Ray Fluorescence Analysis. Theory and Practice of the Fundamental Coefficient Method. X-Ray Spectrometry 1986, 15 (4), 271–285. https://doi.org/https://doi.org/10.1002/xrs.1300150410.

(101) Shiraiwa, T.; Fujino, N. Theoretical Calculation of Fluorescent X-Ray Intensities in Fluorescent X-Ray Spectrochemical Analysis. Jpn J Appl Phys 1966, 5 (10), 886. https://doi.org/10.1143/JJAP.5.886.

(102) Pessanha, S.; Fonseca, C.; Santos, J. P.; Carvalho, M. L.; Dias, A. A. Comparison of Standard-Based and Standardless Methods of Quantification Used in X-Ray Fluorescence Analysis: Application to the Exoskeleton of Clams. X-Ray Spectrometry 2018, 47 (2), 108–115. https://doi.org/https://doi.org/10.1002/xrs.2819.

(103) Carvalho, P. M. S.; Pessanha, S.; Machado, J.; Silva, A. L.; Veloso, J.; Casal, D.; Pais, D.; Santos, J. P. Energy Dispersive X-Ray Fluorescence Quantitative Analysis of Biological Samples with the External Standard Method. Spectrochim Acta Part B At Spectrosc 2020, 174, 105991. https://doi.org/https://doi.org/10.1016/j.sab.2020.105991.

(104) Skiba, M.; Guedes, G.; Karpov, D.; Feliu, N.; L. Cortajarena, A.; Parak, W. J.; Sanchez-Cano, C. Probing the Cellular Fate of the Protein Corona around Nanoparticles with Nanofocused X-Ray Fluorescence Imaging. Int J Mol Sci 2024, 25 (1). https://doi.org/10.3390/ijms25010528.

(105) Schulz, F.; Homolka, T.; Bastús, N. G.; Puntes, V.; Weller, H.; Vossmeyer, T. Little Adjustments Significantly Improve the Turkevich Synthesis of Gold Nanoparticles. Langmuir 2014, 30 (35), 10779–10784.

(106) Stockert, J. C.; Horobin, R. W.; Colombo, L. L.; Blázquez-Castro, A. Tetrazolium Salts and Formazan Products in Cell Biology: Viability Assessment, Fluorescence Imaging, and Labeling Perspectives. Acta Histochemica. Elsevier GmbH April 1, 2018, pp 159–167. https://doi.org/10.1016/j.acthis.2018.02.005.

(107) Strober, W. Trypan Blue Exclusion Test of Cell Viability. Curr Protoc Immunol 2015, 111 (1), A3.B.1-A3.B.3. https://doi.org/10.1002/0471142735.ima03bs111.

(108) Bissardon, C.; Reymond, S.; Salomé, M.; André, L.; Bayat, S.; Cloetens, P.; Bohic, S. Cell Culture on Silicon Nitride Membranes and Cryopreparation for Synchrotron X-Ray Fluorescence Nano-Analysis. Journal of Visualized Experiments 2019, 2019 (154), 1–11. https://doi.org/10.3791/60461.

(109) Schindelin, J.; Arganda-Carreras, I.; Frise, E.; Kaynig, V.; Longair, M.; Pietzsch, T.; Preibisch, S.; Rueden, C.; Saalfeld, S.; Schmid, B.; Tinevez, J. Y.; White, D. J.;

Hartenstein, V.; Eliceiri, K.; Tomancak, P.; Cardona, A. Fiji: An Open-Source Platform for Biological-Image Analysis. Nature Methods. July 2012, pp 676–682. https://doi.org/10.1038/nmeth.2019.

(110) Pike, J. A.; Styles, I. B.; Rappoport, J. Z.; Heath, J. K. Quantifying Receptor Trafficking and Colocalization with Confocal Microscopy. Methods 2017, 115, 42–54. https://doi.org/10.1016/j.ymeth.2017.01.005.

(111) Bolte, S.; Cordelières, F. P. A Guided Tour into Subcellular Colocalization Analysis in Light Microscopy. J Microsc 2006, 224 (3), 213–232. https://doi.org/10.1111/j.1365-2818.2006.01706.x.

(112) Manders, E. M. M.; Verbeek, F. J.; Aten, J. A. Measurement of Co-localization of Objects in Dual-colour Confocal Images. J Microsc 1993, 169 (3), 375–382. https://doi.org/10.1111/j.1365-2818.1993.tb03313.x.

(113) Costes, S. V.; Daelemans, D.; Cho, E. H.; Dobbin, Z.; Pavlakis, G.; Lockett, S. Automatic and Quantitative Measurement of Protein-Protein Colocalization in Live Cells. Biophys J 2004, 86 (6), 3993–4003. https://doi.org/10.1529/biophysj.103.038422.

(114) Milani, S.; Baldelli Bombelli, F.; Pitek, A. S.; Dawson, K. A.; Rädler, J. Reversible versus Irreversible Binding of Transferrin to Polystyrene Nanoparticles: Soft and Hard Corona. ACS Nano 2012, 6 (3), 2532–2541. https://doi.org/10.1021/nn204951s.

(115) Stepanenko, A. A.; Dmitrenko, V. V. Pitfalls of the MTT Assay: Direct and off-Target Effects of Inhibitors Can Result in over/Underestimation of Cell Viability. Gene 2015, 574 (2), 193–203. https://doi.org/10.1016/j.gene.2015.08.009.

(116) Sousa De Almeida, M.; Susnik, E.; Drasler, B.; Taladriz-Blanco, P.; Petri-Fink, A.; Rothen-Rutishauser, B. Understanding Nanoparticle Endocytosis to Improve Targeting Strategies in Nanomedicine. Chemical Society Reviews. Royal Society of Chemistry May 7, 2021, pp 5397–5434. https://doi.org/10.1039/d0cs01127d.

(117) Li, Y.; Kröger, M.; Liu, W. K. Endocytosis of PEGylated Nanoparticles Accompanied by Structural and Free Energy Changes of the Grafted Polyethylene Glycol. Biomaterials 2014, 35 (30), 8467–8478. https://doi.org/10.1016/j.biomaterials.2014.06.032.

(118) Li, Y.; Monteiro-Riviere, N. A. Mechanisms of Cell Uptake, Inflammatory Potential and Protein Corona Effects with Gold Nanoparticles. Nanomedicine 2016, 11 (24), 3185–3203. https://doi.org/10.2217/nnm-2016-0303.

(119) Ma, X.; Hartmann, R.; Jimenez De Aberasturi, D.; Yang, F.; Soenen, S. J. H.; Manshian, B. B.; Franz, J.; Valdeperez, D.; Pelaz, B.; Feliu, N.; Hampp, N.; Riethmüller, C.; Vieker,

H.; Frese, N.; Gölzhäuser, A.; Simonich, M.; Tanguay, R. L.; Liang, X. J.; Parak, W. J. Colloidal Gold Nanoparticles Induce Changes in Cellular and Subcellular Morphology. ACS Nano 2017, 11 (8), 7807–7820. https://doi.org/10.1021/acsnano.7b01760.

(120) Saftig, P.; Klumperman, J. Lysosome Biogenesis and Lysosomal Membrane Proteins: Trafficking Meets Function. Nat Rev Mol Cell Biol 2009, 10 (9), 623–635. https://doi.org/10.1038/nrm2745.

(121) Chanana, M.; Rivera-gil, P.; Correa-Duarte, M. A.; Liz-Marzán, L. M.; Parak, W. J. Physicochemical Properties of Protein-Coated Gold Nanoparticles in Biological Fluids and Cells before and after Proteolytic Digestion. Angewandte Chemie - International Edition 2013, 52 (15), 4179–4183. https://doi.org/10.1002/anie.201208019.

(122) Chithrani, B. D.; Ghazani, A. A.; Chan, W. C. W. Determining the Size and Shape Dependence of Gold Nanoparticle Uptake into Mammalian Cells. Nano Lett 2006, 6 (4), 662–668. https://doi.org/10.1021/nl052396o.

(123) Yue, J.; Feliciano, T. J.; Li, W.; Lee, A.; Odom, T. W. Gold Nanoparticle Size and Shape Effects on Cellular Uptake and Intracellular Distribution of SiRNA Nanoconstructs. Bioconjug Chem 2017, 28 (6), 1791–1800. https://doi.org/10.1021/acs.bioconjchem.7b00252.

(124) Lu, H.; Su, J.; Mamdooh, R.; Li, Y.; Stenzel, M. H. Cellular Uptake of Gold Nanoparticles and Their Movement in 3D Multicellular Tumor Spheroids: Effect of Molecular Weight and Grafting Density of Poly(2-Hydroxyl Ethyl Acrylate). Macromol Biosci 2020, 20 (1). https://doi.org/10.1002/mabi.201900221.

(125) Sun, X.; Gamal, M.; Nold, P.; Said, A.; Chakraborty, I.; Pelaz, B.; Schmied, F.; von Pückler, K.; Figiel, J.; Zhao, Y.; Brendel, C.; Hassan, M.; Parak, W. J.; Feliu, N. Tracking Stem Cells and Macrophages with Gold and Iron Oxide Nanoparticles – The Choice of the Best Suited Particles. Appl Mater Today 2019, 15, 267–279. https://doi.org/10.1016/j.apmt.2018.12.006.

(126) Behzadi, S.; Serpooshan, V.; Tao, W.; Hamaly, M. A.; Alkawareekd, M. Y.; Dreaden, E. C.; Brown, D.; Alkilany, A. M.; Farokhzad, O. C.; Morteza, M. Cellular Uptake of Nanoparticles: Journey Inside the Cell. Chem. Soc. Rev. 2017, 46 (14), 4218–4244. https://doi.org/10.1039/c6cs00636a.Cellular.

(127) Gunduz, N.; Ceylan, H.; Guler, M. O.; Tekinay, A. B. Intracellular Accumulation of Gold Nanoparticles Leads to Inhibition of Macropinocytosis to Reduce the Endoplasmic Reticulum Stress. Sci Rep 2017, 7 (February), 1–10. https://doi.org/10.1038/srep40493.

(128) Hopkins, C. R.; Trowbridge, I. S. Internalization and Processing of Transferrin and the Transferrin Receptor in Human Carcinoma A431 Cells. Journal of Cell Biology 1983, 97 (2), 508–521. https://doi.org/10.1083/jcb.97.2.508.

(129) Faul, F.; Erdfelder, E.; Lang, A. G.; Buchner, A. G*Power 3: A Flexible Statistical Power Analysis Program for the Social, Behavioral, and Biomedical Sciences. Behav Res Methods 2007, 39 (2), 175–191. https://doi.org/10.3758/BF03193146.

(130) Cohen, J. Statistical Power Analysis for the Behavioral Sciences, Second Edi.; Lawrence Erlbaum Associates: New York, 1988.

(131) Martinez-Criado, G.; Villanova, J.; Tucoulou, R.; Salomon, D.; Suuronen, J. P.; Laboure, S.; Guilloud, C.; Valls, V.; Barrett, R.; Gagliardini, E.; Dabin, Y.; Baker, R.; Bohic, S.; Cohen, C.; Morse, J. ID16B: A Hard X-Ray Nanoprobe Beamline at the ESRF for Nano-Analysis. J Synchrotron Radiat 2016, 23, 344–352. https://doi.org/10.1107/S1600577515019839.

(132) Cesar da Silva, J.; Pacureanu, A.; Yang, Y.; Bohic, S.; Morawe, C.; Barrett, R.; Cloetens, P. Efficient Concentration of High-Energy x-Rays for Diffraction-Limited Imaging Resolution. Optica 2017, 4 (5), 492. https://doi.org/10.1364/optica.4.000492.

(133) Schroer, C. G.; Boye, P.; Feldkamp, J. M.; Patommel, J.; Samberg, D.; Schropp, A.; Schwab, A.; Stephan, S.; Falkenberg, G.; Wellenreuther, G.; Reimers, N. Hard X-Ray Nanoprobe at Beamline P06 at PETRA III. Nucl Instrum Methods Phys Res A 2010, 616 (2–3), 93–97. https://doi.org/10.1016/j.nima.2009.10.094.

(134) Quinn, P. D.; Alianelli, L.; Gomez-Gonzalez, M.; Mahoney, D.; Cacho-Nerin, F.; Peach, A.; Parker, J. E. The Hard X-Ray Nanoprobe Beamline at Diamond Light Source. J Synchrotron Radiat 2021, 28, 1006–1013. https://doi.org/10.1107/S1600577521002502.

(135) Pirollo, K. F.; Chang, E. H. Does a Targeting Ligand Influence Nanoparticle Tumor Localization or Uptake? Trends Biotechnol 2008, 26 (10), 552–558. https://doi.org/10.1016/j.tibtech.2008.06.007.

(136) Chen, Y.-Q.; Xue, M.-D.; Li, J.-L.; Huo, D.; Ding, H.-M.; Ma, Y. Uncovering the Importance of Ligand Mobility on Cellular Uptake of Nanoparticles: Insights from Experimental, Computational, and Theoretical Investigations. ACS Nano 2024, 18 (8), 6463–6476. https://doi.org/10.1021/acsnano.3c11982.

(137) Megahed, S.; Wutke, N.; Liu, Y.; Klapper, M.; Schulz, F.; Feliu, N.; Parak, W. J. Encapsulation of Nanoparticles with Statistical Copolymers with Different Surface

Charges and Analysis of Their Interactions with Proteins and Cells. Int J Mol Sci 2024, 25 (10). https://doi.org/10.3390/ijms25105539.

(138) Shi, P.; Cheng, Z.; Zhao, K.; Chen, Y.; Zhang, A.; Gan, W.; Zhang, Y. Active Targeting Schemes for Nano-Drug Delivery Systems in Osteosarcoma Therapeutics. J Nanobiotechnology 2023, 21 (1), 103. https://doi.org/10.1186/s12951-023-01826-1.

(139) Rampado, R.; Crotti, S.; Caliceti, P.; Pucciarelli, S.; Agostini, M. Recent Advances in Understanding the Protein Corona of Nanoparticles and in the Formulation of "Stealthy" Nanomaterials. Front Bioeng Biotechnol 2020, 8 (April), 1–19. https://doi.org/10.3389/fbioe.2020.00166.

(140) Sanchez-Cano, C.; Carril, M. Recent Developments in the Design of Non-Biofouling Coatings for Nanoparticles and Surfaces. Int J Mol Sci 2020, 21 (3), 1–24. https://doi.org/10.3390/ijms21031007.

(141) Kreyling, W. G.; Abdelmonem, A. M.; Ali, Z.; Alves, F.; Geiser, M.; Haberl, N.; Hartmann, R.; Hirn, S.; De Aberasturi, D. J.; Kantner, K.; Khadem-Saba, G.; Montenegro, J. M.; Rejman, J.; Rojo, T.; De Larramendi, I. R.; Ufartes, R.; Wenk, A.; Parak, W. J. In Vivo Integrity of Polymer-Coated Gold Nanoparticles. Nat Nanotechnol 2015, 10 (7), 619–623. https://doi.org/10.1038/nnano.2015.111.

(142) Llop, J.; Jiang, P.; Marradi, M.; Yu, S.; Puigivila, M.; Baz, Z.; Szczupak, B.; Mao, Z.; Gao, C.; Moya, S. E. Visualisation of Dual Radiolabelled Poly(Lactide-Co-Glycolide) Nanoparticle Degradation in Vivo Using Energy-Discriminant SPECT. Journal of Materials Chemistry B Previous 2015, No. 30, 31–32.

(143) Bargheer, D.; Nielsen, J.; Gébel, G.; Heine, M.; Salmen, S. C.; Stauber, R.; Weller, H.; Heeren, J.; Nielsen, P. The Fate of a Designed Protein Corona on Nanoparticles in Vitro and in Vivo. Beilstein Journal of Nanotechnology 2015, 6 (1), 36–46. https://doi.org/10.3762/bjnano.6.5.

(144) Casanova, E. A.; Rodriguez-Palomo, A.; Stähli, L.; Arnke, K.; Gröninger, O.; Generali, M.; Neldner, Y.; Tiziani, S.; Dominguez, A. P.; Guizar-Sicairos, M.; Gao, Z.; Appel, C.; Nielsen, L. C.; Georgiadis, M.; Weber, F. E.; Stark, W.; Pape, H.-C.; Cinelli, P.; Liebi, M. SAXS Imaging Reveals Optimized Osseointegration Properties of Bioengineered Oriented 3D-PLGA/ACaP Scaffolds in a Critical Size Bone Defect Model. Biomaterials 2023, 294, 121989. https://doi.org/https://doi.org/10.1016/j.biomaterials.2022.121989.

(145) Nicolas, J.-D.; Bernhardt, M.; Markus, A.; Alves, F.; Burghammer, M.; Salditt, T. Scanning X-Ray Diffraction on Cardiac Tissue: Automatized Data Analysis and Processing. J Synchrotron Radiat 2017, 24 (6), 1163–1172.

(146) Cassini, C.; Wittmeier, A.; Brehm, G.; Denz, M.; Burghammer, M.; Köster, S. Large Field-of-View Scanning Small-Angle X-Ray Scattering of Mammalian Cells. J Synchrotron Radiat 2020, 27, 1059–1068. https://doi.org/10.1107/S1600577520006864.

(147) Haase, A.; Umbach, G. L. & E. Röntgen Centennial; WORLD SCIENTIFIC, 1997. https://doi.org/doi:10.1142/3428.

(148) Hamley, I. W. Small-Angle Scattering: Theory, Instrumentation, Data, and Applications; Wiley, 2021.

(149) Ares, A. E. X-Ray Scattering; IntechOpen, 2017.

(150) Schnablegger, H.; Singh, Y. The SAXS Guide: Getting Acquainted with the Principles; Anton Paar GmbH, 2017.

(151) Glatter, O.; Kratky, O. Small Angle X-Ray Scattering; Academic Press, 1982.

(152) Nakamura, K.; Kawabata, T.; Mori, Y. Size Distribution Analysis of Colloidal Gold by Small Angle X-Ray Scattering and Light Absorbance. Powder Technol 2003, 131 (2), 120–128. https://doi.org/https://doi.org/10.1016/S0032-5910(02)00340-6.

(153) Pauw, B. R.; Pedersen, J. S.; Tardif, S.; Takata, M.; Iversen, B. B. Improvements and Considerations for Size Distribution Retrieval from Small-Angle Scattering Data by Monte Carlo Methods. J Appl Crystallogr 2013, 46 (2), 365–371. https://doi.org/https://doi.org/10.1107/S0021889813001295.

(154) Putnam, D. K.; Lowe, E. W.; Meiler, J. RECONSTRUCTION OF SAXS PROFILES FROM PROTEIN STRUCTURES. Comput Struct Biotechnol J 2013, 8 (11), e201308006. https://doi.org/https://doi.org/10.5936/csbj.201308006.

(155) Narayanan, T. Synchrotron Small-Angle X-Ray Scattering. In Soft Matter Characterization; Borsali, R., Pecora, R., Eds.; Springer Netherlands: Dordrecht, 2008; pp 899–952. https://doi.org/10.1007/978-1-4020-4465-6_17.

(156) Ballauff, M.; Jusufi, A. Anomalous Small-Angle X-Ray Scattering: Analyzing Correlations and Fluctuations in Polyelectrolytes. Colloid and Polymer Science. August 2006, pp 1303–1311. https://doi.org/10.1007/s00396-006-1516-5.

(157) Hendrickson, W. A. Anomalous Diffraction in Crystallographic Phase Evaluation. Q Rev Biophys 2014, 47 (1), 49–93. https://doi.org/DOI: 10.1017/S0033583514000018.

(158) Gruzinov, A. Yu.; Schroer, M. A.; Manalastas-Cantos, K.; Kikhney, A. G.; Hajizadeh, N. R.; Schulz, F.; Franke, D.; Svergun, D. I.; Blanchet, C. E. Anomalous SAXS at P12 Beamline EMBL Hamburg: Instrumentation and Applications. J Synchrotron Radiat 2021, 28 (3), 812–823. https://doi.org/10.23689/fidgeo-4434.

(159) Nakanishi, R.; Machida, G.; Kinoshita, M.; Sakurai, K.; Akiba, I. Anomalous Small-Angle X-Ray Scattering Study on the Spatial Distribution of Hydrophobic Molecules in Polymer Micelles. Polym J 2016, 48 (7), 801–806. https://doi.org/10.1038/pj.2016.32.

(160) Sztucki, M.; Di Cola, E.; Narayanan, T. Anomalous Small-Angle X-Ray Scattering from Charged Soft Matter. Eur Phys J Spec Top 2012, 208 (1), 319–331. https://doi.org/10.1140/epjst/e2012-01627-x.

(161) Stuhrmann, H. B. Resonance Scattering in Macromolecular Structure Research. In Characterization of Polymers in the Solid State II: Synchrotron Radiation, X-ray Scattering and Electron Microscopy; Kausch, H. H., Zachmann, H. G., Eds.; Springer Berlin Heidelberg: Berlin, Heidelberg, 1985; pp 123–163.

(162) Goerigk, G.; Mattern, N. Spinodal Decomposition in Ni-Nb-Y Metallic Glasses Analyzed by Quantitative Anomalous Small-Angle X-Ray Scattering. In Journal of Physics: Conference Series; Institute of Physics Publishing, 2010; Vol. 247. https://doi.org/10.1088/1742-6596/247/1/012022.

(163) Goerigk, G.; Huber, K.; Mattern, N.; Williamson, D. L. Quantitative Anomalous Small-Angle X-Ray Scattering - The Determination of Chemical Concentrations in Nano-Scaled Phases. European Physical Journal: Special Topics. June 2012, pp 259–274. https://doi.org/10.1140/epjst/e2012-01623-2.

(164) Goerigk, G. J. The Solution of the Eigenvector Problem in Synchrotron Radiation Based Anomalous Small-Angle X-Ray Scattering. Advances in Linear Algebra & Matrix Theory 2013, 03 (04), 59–68. https://doi.org/10.4236/alamt.2013.34012.

(165) Guinier, A.; Fournet, G. Small-Angle Scattering of X-Rays; Structure of matter series; Wiley, 1955.

(166) Marquardt, D. W. An Algorithm for Least-Squares Estimation of Nonlinear Parameters. Journal of the Society for Industrial and Applied Mathematics 1963, 11 (2), 431–441. https://doi.org/10.1137/0111030.

(167) Vrugt J. A.; ter Braak C.J.F.; Diks C.G.H.; Robinson B. A.; Hyman J. M.; Higdon D. Accelerating Markov Chain Monte Carlo Simulation by Differential Evolution with Self-

Adaptive Randomized Subspace Sampling. 2009, 10 (3), 273–290. https://doi.org/doi:10.1515/IJNSNS.2009.10.3.273.

(168) Clapp, A. R.; Medintz, I. L.; Tetsuo Uyeda, H.; Fisher, B. R.; Goldman, E. R.; Bawendi, M. G.; Mattoussi, H. Quantum Dot-Based Multiplexed Fluorescence Resonance Energy Transfer. J Am Chem Soc 2005, 127 (51), 18212–18221. https://doi.org/10.1021/ja054630i.

(169) Mattoussi, H.; Matthew Mauro, J.; Goldman, E. R.; Anderson, G. P.; Sundar, V. C.; Mikulec, F. V.; Bawendi, M. G. Self-Assembly of CdSe-ZnS Quantum Dot Bioconjugates Using an Engineered Recombinant Protein. J Am Chem Soc 2000, 122 (49), 12142–12150. https://doi.org/10.1021/ja002535y.

(170) Gurunatha, K. L.; Fournier, A. C.; Urvoas, A.; Valerio-Lepiniec, M.; Marchi, V.; Minard, P.; Dujardin, E. Nanoparticles Self-Assembly Driven by High Affinity Repeat Protein Pairing. ACS Nano 2016, 10 (3), 3176–3185. https://doi.org/10.1021/acsnano.5b04531.

(171) Haas, S.; Sun, X.; Conceicao, A. L. C.; Horbach, J.; Pfeffer, S. The New Small-Angle X-Ray Scattering Beamline for Materials Research at PETRA III: SAXSMAT Beamline P62. J Synchrotron Radiat 2023, 30 (6), 1156–1167.

(172) Kieffer, J.; Wright, J. P. PyFAI: A Python Library for High Performance Azimuthal Integration on GPU. Powder Diffr 2013, 28 (S2), S339–S350. https://doi.org/DOI: 10.1017/S0885715613000924.

(173) Doucet, M.; Cho, J. H.; Alina, G.; Attala, Z.; Bakker, J.; Beaucage, P.; Bouwman, W.; Bourne, R.; Butler, P.; Cadwallader-Jones, I.; Campbell, K.; Cooper-Benun, T.; Durniak, C.; Forster, L.; Gilbert, P.; Gonzalez, M.; Heenan, R.; Jackson, A.; King, S.; Kienzle, P.; Krzywon, J.; Maranville, B.; Martinez, N.; Murphy, R.; Nielsen, T.; O'Driscoll, L.; Potrzebowski, W.; Prescott, S.; Ferraz Leal, R.; Rozyczko, P.; Snow, T.; Washington, A.; Wilkins, L.; Wolf, C. SasView Version 5.0.6. Zenodo June 2023. https://doi.org/10.5281/zenodo.7581379.

(174) Perera, Y. R.; Xu, J. X.; Amarasekara, D. L.; Hughes, A. C.; Abbood, I.; Fitzkee, N. C. Understanding the Adsorption of Peptides and Proteins onto Pegylated Gold Nanoparticles. Molecules 2021, 26 (19). https://doi.org/10.3390/molecules26195788.

(175) Manson, J.; Kumar, D.; Meenan, B. J.; Dixon, D. Polyethylene Glycol Functionalized Gold Nanoparticles: The Influence of Capping Density on Stability in Various Media. Gold Bull 2011, 44 (2), 99–105. https://doi.org/10.1007/s13404-011-0015-8.

(176) Li, C.; Zhang, J.-N.; Jin, J.; Jiang, W. The Effect of Topologies and Refilling Short-Chain PEG on Protein Adsorption. Chinese Journal of Polymer Science 2023, 41 (12), 1879–1888. https://doi.org/10.1007/s10118-023-2971-x.

(177) del Mercato, L. L.; Ferraro, M. M.; Baldassarre, F.; Mancarella, S.; Greco, V.; Rinaldi, R.; Leporatti, S. Biological Applications of LbL Multilayer Capsules: From Drug Delivery to Sensing. Adv Colloid Interface Sci 2014, 207, 139–154. https://doi.org/https://doi.org/10.1016/j.cis.2014.02.014.

(178) Ariga, K.; Lvov, Y. M.; Kawakami, K.; Ji, Q.; Hill, J. P. Layer-by-Layer Self-Assembled Shells for Drug Delivery. Adv Drug Deliv Rev 2011, 63 (9), 762–771. https://doi.org/https://doi.org/10.1016/j.addr.2011.03.016.

(179) del Mercato, L. L.; Rivera-Gil, P.; Abbasi, A. Z.; Ochs, M.; Ganas, C.; Zins, I.; Sönnichsen, C.; Parak, W. J. LbL Multilayer Capsules: Recent Progress and Future Outlook for Their Use in Life Sciences. Nanoscale 2010, 2 (4), 458–467. https://doi.org/10.1039/B9NR00341J.

(180) Kolmanovich, D. D.; Chukavin, N. N.; Savintseva, I. V; Mysina, E. A.; Popova, N. R.; Baranchikov, A. E.; Sozarukova, M. M.; Ivanov, V. K.; Popov, A. L. Hybrid Polyelectrolyte Capsules Loaded with Gadolinium-Doped Cerium Oxide Nanoparticles as a Biocompatible MRI Agent for Theranostic Applications. Polymers (Basel) 2023, 15 (18). https://doi.org/10.3390/polym15183840.

(181) Langer, R. Novel Methods of Drug Delivery. Science (1979) 1990, 249 (4976), 1527–1532. https://doi.org/10.1016/0304-3959(90)92625-z.

(182) Decher, G.; Hong, J. D.; Schmitt, J. Buildup of Ultrathin Multiplayer Films by a Self-Assembly Process. II. Consecutive Absorption of Anionie and Cationic Bipolar Amphiphiles and Polyeleetrolytes on Charged Surfaces. Journal of Thin film solids 1992, 210 (1–2), 831–835. https://doi.org/10.1002/bbpc.19910951122.

(183) Zhao, S.; Caruso, F.; Dähne, L.; Decher, G.; De Geest, B. G.; Fan, J.; Feliu, N.; Gogotsi, Y.; Hammond, P. T.; Hersam, M. C.; Khademhosseini, A.; Kotov, N.; Leporatti, S.; Li, Y.; Lisdat, F.; Liz-Marzán, L. M.; Moya, S.; Mulvaney, P.; Rogach, A. L.; Roy, S.; Shchukin, D. G.; Skirtach, A. G.; Stevens, M. M.; Sukhorukov, G. B.; Weiss, P. S.; Yue, Z.; Zhu, D.; Parak, W. J. The Future of Layer-by-Layer Assembly: A Tribute to ACS Nano Associate Editor Helmuth Möhwald. ACS Nano 2019, acsnano.9b03326. https://doi.org/10.1021/acsnano.9b03326.

(184) Caruso, F.; Caruso, R. A.; Mohwald, H. Nanoengineering of Inorganic and Hybrid Hollow Spheres by Colloidal Templating. Science 1998, 282 (5391), 1111–1114. https://doi.org/10.1126/science.282.5391.1111.

(185) Antipov, A. A.; Sukhorukov, G. B.; Leporatti, S.; Radtchenko, I. L.; Donath, E.; Möhwald, H. Polyelectrolyte Multilayer Capsule Permeability Control. Colloids Surf A Physicochem Eng Asp 2002, 198–200 (01), 535–541. https://doi.org/10.1016/S0927-7757(01)00956-6.

(186) Sukhorukov, G. B.; Volodkin, D. V.; Günther, A. M.; Petrov, A. I.; Shenoy, D. B.; Möhwald, H. Porous Calcium Carbonate Microparticles as Templates for Encapsulation of Bioactive Compounds. J Mater Chem 2004, 14 (14), 2073–2081. https://doi.org/10.1039/b402617a.

(187) Trushina, D. B.; Bukreeva, T. V.; Antipina, M. N. Size-Controlled Synthesis of Vaterite Calcium Carbonate by the Mixing Method: Aiming for Nanosized Particles. Cryst Growth Des 2016, 16 (3), 1311–1319. https://doi.org/10.1021/acs.cgd.5b01422.

(188) Stalmann, G. S. D. Optimization of Polyelectrolyte Multilayer Capsules - Optimierung Der Polyelektrolyt Kapseln. Fachbereich Physik Universität Marburg 2010, Bachelorth.

(189) Parakhonskiy, B. V.; Foss, C.; Carletti, E.; Fedel, M.; Haase, A.; Motta, A.; Migliaresi, C.; Antolini, R. Tailored Intracellular Delivery via a Crystal Phase Transition in 400 Nm Vaterite Particles. Biomater Sci 2013, 1 (12), 1273. https://doi.org/10.1039/c3bm60141b.

(190) De Geest, B. G.; De Koker, S.; Sukhorukov, G. B.; Kreft, O.; Parak, W. J.; Skirtach, A. G.; Demeester, J.; De Smedt, S. C.; Hennink, W. E. Polyelectrolyte Microcapsules for Biomedical Applications. Soft Matter 2009, 5 (2), 282–291. https://doi.org/10.1039/B808262F.

(191) Buron, C. C.; Filiâtre, C.; Membrey, F.; Bainier, C.; Charraut, D.; Foissy, A. Early Steps in Layer-by-Layer Construction of Polyelectrolyte Films: The Transition from Surface/Polymer to Polymer/Polymer Determining Interactions. J Colloid Interface Sci 2007, 314 (2), 358–366. https://doi.org/10.1016/j.jcis.2007.05.060.

(192) Buron, C. C.; Filiâtre, C.; Membrey, F.; Bainier, C.; Buisson, L.; Charraut, D.; Foissy, A. Surface Morphology and Thickness of a Multilayer Film Composed of Strong and Weak Polyelectrolytes: Effect of the Number of Adsorbed Layers, Concentration and Type of Salts. Thin Solid Films 2009, 517 (8), 2611–2617. https://doi.org/10.1016/j.tsf.2008.10.036.

(193) Reddy, B. S.; El-bayoumy, K.; Upadhyaya, P.; Rao, C. V. Chemoprevention of Colon Cancer by Organoselenium Compounds and Impact of High- or Low-Fat Diets. J Natl Cancer Inst 1997, 89 (7), 506–512.

(194) Ip, C.; El-bayoumy, K.; Upadhyaya, P.; Ganther, H.; Vadhanavikit, S.; Thompson, H. Comparative Effect of Inorganic and Organic Selenocyanate Derivatives in Mammary Cancer Chemoprevention. Carcinogenesis 1994, 15 (2), 187–192. https://doi.org/10.1093/carcin/15.2.187.

(195) Willett, W. C.; Stampfer, M. J. Selenium and Human Cancer: Epidemiological Aspects and Implications for Clinical Trials. Int J Toxicol 1986, 5 (1), 29–36. https://doi.org/10.3109/10915818609140734.

(196) Avery, J. C.; Hoffmann, P. R. Selenium, Selenoproteins, and Immunity. Nutrients 2018, 10 (9). https://doi.org/10.3390/nu10091203.

(197) Wallenberg, M.; Misra, S.; Björnstedt, M. Selenium Cytotoxicity in Cancer. Basic Clin Pharmacol Toxicol 2014, 114 (5), 377–386. https://doi.org/https://doi.org/10.1111/bcpt.12207.

(198) Zheng, W.; Fadwa Benkessou, B.; Twelkmeyer, S.; Wang, T.; Ginman, H.; Ottosson, M.; Abedi-Valugerdi, M. A.; Subirana, Ying Zhao, M. H. Rapid and Robust Quantification of P-Xyleneselenocyanate in Plasma via Derivatization. Anal. Chem 2017, 89, 7586−7592. https://doi.org/10.1021/acs.analchem.7b01426.

(199) Reddy, B. S.; Kulkarni, N. Chemoprevention of Colon Carcinogenesis by the Synthetic Organoselenium Compound 1,4-Pheny Lenebis(Methy Lene)Selenocyanate. Cancer Res 1992, 52 (20), 5635–5640.

(200) El-bayoiuny, K.; Upadhyaya, P.; Desai, D. H.; Amin, S.; Hecht, S. S. Tumorigenicity in Mouse Lung By the Synthetic Organoselenium Compound , 1 , 4-Pheny Lenebis (Methylene) Selenocyanate. Carcinogenesis 1993, 14 (6), 1111–1114.

(201) Zheng, W.; Boada, R.; He, R.; Xiao, T.; Ye, F.; Simonelli, L.; Valiente, M.; Zhao, Y.; Hassan, M. Extracellular Albumin Covalently Sequesters Selenocompounds and Determines Cytotoxicity. Int J Mol Sci 2019, 20 (19). https://doi.org/10.3390/ijms20194734.

(202) Muñoz Javier, A.; Kreft, O.; Semmling, M.; Kempter, S.; Skirtach, A. G.; Bruns, O. T.; del Pino, P.; Bedard, M. F.; Rädler, J.; Käs, J.; Plank, C.; Sukhorukov, G. B.; Parak, W. J. Uptake of Colloidal Polyelectrolyte-Coated Particles and Polyelectrolyte Multilayer

Capsules by Living Cells. Advanced Materials 2008, 20 (22), 4281–4287. https://doi.org/https://doi.org/10.1002/adma.200703190.

(203) Kastl, L.; Sasse, D.; Wulf, V.; Hartmann, R.; Mircheski, J.; Ranke, C.; Carregal-Romero, S.; Martínez-López, J. A.; Fernández-Chacón, R.; Parak, W. J.; Elsasser, H. P.; Riveragil, P. Multiple Internalization Pathways of Polyelectrolyte Multilayer Capsules into Mammalian Cells. ACS Nano 2013, 7 (8), 6605–6618. https://doi.org/10.1021/nn306032k.

(204) De Koker, S.; De Geest, B. G.; Cuvelier, C.; Ferdinande, L.; Deckers, W.; Hennink, W. E.; De Smedt, S.; Mertens, N. In Vivo Cellular Uptake, Degradation, and Biocompatibility of Polyelectrolyte Microcapsules. Adv Funct Mater 2007, 17 (18), 3754–3763. https://doi.org/10.1002/adfm.200700416.

(205) Javier, A. M.; Kreft, O.; Semmling, M.; Kempter, S.; Skirtach, A. G.; Bruns, O. T.; Del Pino, P.; Bedard, M. F.; Rädler, J.; Käs, J.; Plank, C.; Sukhorukov, G. B.; Parak, W. J. Uptake of Colloidal Polyelectrolyte-Coated Particles and Polyelectrolyte Multilayer Capsules by Living Cells. Advanced Materials 2008, 20 (22), 4281–4287. https://doi.org/10.1002/adma.200703190.

(206) Roy, S.; Zhu, D.; Parak, W. J.; Feliu, N. Lysosomal Proton Buffering of Poly(Ethylenimine) Measured In Situ by Fluorescent PH-Sensor Microcapsules. ACS Nano 2020, 14 (7), 8012–8023. https://doi.org/10.1021/acsnano.9b10219.

(207) Palankar, R.; Pinchasik, B.-E.; Schmidt, S.; De Geest, B. G.; Fery, A.; Möhwald, H.; Skirtach, A. G.; Delcea, M. Mechanical Strength and Intracellular Uptake of CaCO3-Templated LbL Capsules Composed of Biodegradable Polyelectrolytes: The Influence of the Number of Layers. J Mater Chem B 2013, 1 (8), 1175–1181. https://doi.org/10.1039/C2TB00319H.

(208) Köhler, K.; Sukhorukov, G. B. Heat Treatment of Polyelectrolyte Multilayer Capsules: A Versatile Method for Encapsulation. Adv Funct Mater 2007, 17 (13), 2053–2061. https://doi.org/10.1002/adfm.200600593.

(209) O'Brien, J.; Wilson, I.; Orton, T.; Pognan, F. Investigation of the Alamar Blue (Resazurin) Fluorescent Dye for the Assessment of Mammalian Cell Cytotoxicity. Eur J Biochem 2000, 267 (17), 5421–5426. https://doi.org/https://doi.org/10.1046/j.1432-1327.2000.01606.x.

(210) Keshtkar, E.; Kudsk, P.; Mesgaran, M. B. Perspective: Common Errors in Dose–Response Analysis and How to Avoid Them. Pest Manag Sci 2021, 77 (6), 2599–2608. https://doi.org/https://doi.org/10.1002/ps.6268.

(211) Sebaugh, J. L. Guidelines for Accurate EC50/IC50 Estimation. Pharm Stat 2011, 10 (2), 128–134. https://doi.org/https://doi.org/10.1002/pst.426.

(212) Kang, Y.; Nack, L. M.; Liu, Y.; Qi, B.; Huang, Y.; Liu, Z.; Chakraborty, I.; Schulz, F.; Ahmed, A. A. A.; Clavo Poveda, M.; Hafizi, F.; Roy, S.; Mutas, M.; Holzapfel, M.; Sanchez-Cano, C.; Wegner, K. D.; Feliu, N.; Parak, W. J. Quantitative Considerations about the Size Dependence of Cellular Entry and Excretion of Colloidal Nanoparticles for Different Cell Types. ChemTexts 2022, 8 (1), 9. https://doi.org/10.1007/s40828-021-00159-6.

(213) Schoonjans, T.; Brunetti, A.; Golosio, B.; Sanchez del Rio, M.; Solé, V. A.; Ferrero, C.; Vincze, L. The Xraylib Library for X-Ray–Matter Interactions. Recent Developments. Spectrochim Acta Part B At Spectrosc 2011, 66 (11), 776–784. https://doi.org/https://doi.org/10.1016/j.sab.2011.09.011.

(214) Mirabelli, P.; Coppola, L.; Salvatore, M. Cancer Cell Lines Are Useful Model Systems for Medical Research. Cancers. MDPI AG August 1, 2019. https://doi.org/10.3390/cancers11081098.

(215) Kirchner, C.; Javier, A. M.; Susha, A. S.; Rogach, A. L.; Kreft, O.; Sukhorukov, G. B.; Parak, W. J. Cytotoxicity of Nanoparticle-Loaded Polymer Capsules. Talanta 2005, 67 (3), 486–491. https://doi.org/https://doi.org/10.1016/j.talanta.2005.06.042.

(216) Trushina, D. B.; Akasov, R. A.; Khovankina, A. V; Borodina, T. N.; Bukreeva, T. V; Markvicheva, E. A. Doxorubicin-Loaded Biodegradable Capsules: Temperature Induced Shrinking and Study of Cytotoxicity in Vitro. J Mol Liq 2019, 284, 215–224. https://doi.org/https://doi.org/10.1016/j.molliq.2019.03.152.

(217) Rivera-Gil, P.; De Koker, S.; De Geest, B. G.; Parak, W. J. Intracellular Processing of Proteins Mediated by Biodegradable Polyelectrolyte Capsules. Nano Lett 2009, 9 (12), 4398–4402. https://doi.org/10.1021/nl902697j.

(218) Schnitzer, J. E.; Oh, P. Albondin-Mediated Capillary Permeability to Albumin. Differential Role of Receptors in Endothelial Transcytosis and Endocytosis of Native and Modified Albumins. Journal of Biological Chemistry 1994, 269 (8), 6072–6082. https://doi.org/https://doi.org/10.1016/S0021-9258(17)37571-3.

(219) Semmling, M.; Kreft, O.; Muñoz Javier, A.; Sukhorukov, G. B.; Käs, J.; Parak, W. J. A Novel Flow-Cytometry-Based Assay for Cellular Uptake Studies of Polyelectrolyte Microcapsules. Small 2008, 4 (10), 1763–1768. https://doi.org/https://doi.org/10.1002/smll.200800596.

Acknowledgement

As I conclude this thesis, I would like to take the opportunity to express my gratitude to all those who have been at my side, without whom this remarkable journey would not have been possible.

First, I want to thank Prof. Wolfgang, J. Parak. Since now many years ago when I had the privilege of joining your lab as a young unexperienced undergraduate student, I have benefited greatly from your genuine support, trust, and constructive feedback. I am deeply grateful for your invaluable guidance and making all of this even possible.

I could not imagine to undertake this exploration in the world of X-ray analytics without the support of Dr. Carlos Sanchez-Cano. Your enthusiasm in scientific inquiries along with practical teaching and guidance has been essential in leading me to where I am now.

I would like to express my gratitude to Dr. Saša Bajt for our productive collaboration and for agreeing to serve as a second examiner for my thesis. Moreover, I want to thank Prof. B. Rothen-Rutishauser for the additional review of my dissertation, and Prof. Dorota Koziej for joining the board of examiners.

I am also thankful to Prof. Tobias Beck for being my second supervisor as part of the CUI:AIM graduate school. I highly appreciate our discussions and your feedback throughout this time.

Furthermore, many thanks to Dr. Gerald Falkenberg, Dr. Dennis Brückner and Dr. Ruixia Wang for your support in numerous beamtimes, your encouragement was substantial from planning, execution to analysis. Special thanks to Dr. Florian Schulz for the insightful discussions and guidance, also in broader scientific contexts, which were greatly valued and enriched my understanding. I would like to thank Dr. Neus Feliu for her involvement and contributions during these projects, which I appreciate greatly. Moreover, I deeply appreciate the collaboration with Dr. Gabriela Guedes Faria and. Prof. Aitziber Cortajarena, which has been invaluable for the realization of this research. The assistance and technical expertise of Dr. Sylvio Haas, Dr. Xiao Sun, Dr. Dmitry Karpov and Dr. Peter Cloetens in conducting synchrotron experiments at P62-DESY and ID16A-ESRF, respectively, greatly contributed to the success of this investigations. Many thanks to Dr. Maria Riedner for your support during my initial steps into the world of mass spectrometry. For handling all the organizational tasks during this time, I would like to thank Marten Rittner, Helen Oqueka and Yang Ye. Special thanks to Dr. Gerwin Chilla, for managing the organizational aspects and for engaging in valuable scientific discussions. Thank you, Lars, for your friendship and valuable scientific collaboration. I would like to thank Dr. Saša Bajt, Prof. Henry Chapman, Dr. Mauro Prasciolu

as well as the entire team involved, for their support and the valuable knowledge I gained from this collaboration.
Further, I would like to thank Marta Gallego Gonzalez, Juan Barrios and Kai-Wei Lin for electron microscopy examinations. Additionally, I'm thankful to Raquel Pazos, Javier Calvo Martinez, Jili Han, Yuxuan Han, Bo Peng and Jinrui Li for additional ICP-MS measurements. I'm thankful for the colleagues and friends during my research stays abroad, Esteban, Juan, Douglas and Raphael to heartly welcome me, helped me out and let me enjoy this time. In this context I want to thank Prof. Luca Salassa and Prof. Jesus Ruiz-Cabello for providing me with office and lab spaces.
Additionally, this work would not have been possible without the substantial support from the DFG in the form of the Excellence Cluster CUI: Advanced Imaging of Matter. I want to thank all people involved in the cluster for your exceptional organizational effort throughout the workshops and summer schools. Additionally, I would like to acknowledge the invaluable assistance provided in navigating financial and contractual matters. I'd like to express my heartfelt gratitude to my incredible colleagues and friends: Nils, Martin, Ferdinand, Sani, Robbert, Sarodi, Tim, Rukan, Marie, Maya, Malte and Maria. Your steady support, companionship, and shared laughter have not only enriched my professional journey but have also made this experience truly memorable. Working with all of you has truly been both a privilege and a joy.
On a personal note, I extend my deepest thanks to my family, to Rebeka and my dear friends – Tom, Katy, Patrick, Hendrik, your encouragement, understanding, and company have been a source of strength and joy throughout this journey, for which I am truly grateful.

Eidesstattliche Versicherung

Hiermit versichere ich an Eides statt, die vorliegende Dissertationsschrift selbst verfasst und keine anderen als die angegebenen Hilfsmittel und Quellen benutzt zu haben.

Sofern im Zuge der Erstellung der vorliegenden Dissertationsschrift generative Künstliche Intelligenz (gKI) basierte elektronische Hilfsmittel verwendet wurden, versichere ich, dass meine
eigene Leistung im Vordergrund stand und dass eine vollständige Dokumentation aller verwendeten Hilfsmittel gemäß der Guten wissenschaftlichen Praxis vorliegt. Ich trage die Verantwortung für eventuell durch die gKI generierte fehlerhafte oder verzerrte Inhalte, fehlerhafte Referenzen, Verstöße gegen das Datenschutz- und Urheberrecht oder Plagiate.

Datum

Unterschrift der Doktorandin / des Doktoranden